COMPUTATION OF QUASI-PERIODIC TORI AND HETEROCLINIC CONNECTIONS IN ASTRODYNAMICS USING COLLOCATION TECHNIQUES

by

Zubin P. Olikara

B.S., Purdue University, 2007

M.S., Purdue University, 2010

A thesis submitted to the

Faculty of the Graduate School of the

University of Colorado in partial fulfillment

of the requirements for the degree of

Doctor of Philosophy

Department of Aerospace Engineering Sciences

2016

This thesis entitled:
Computation of Quasi-Periodic Tori and Heteroclinic Connections
in Astrodynamics Using Collocation Techniques
written by Zubin P. Olikara
has been approved for the Department of Aerospace Engineering Sciences

Daniel J. Scheeres

Hanspeter Schaub

Date

The final copy of this thesis has been examined by the signatories, and we find that both the content and the form meet acceptable presentation standards of scholarly work in the above mentioned discipline.

Olikara, Zubin P. (Ph.D., Aerospace Engineering Sciences)

Computation of Quasi-Periodic Tori and Heteroclinic Connections in Astrodynamics Using Collocation Techniques

Thesis directed by Prof. Daniel J. Scheeres

Many astrodynamical systems exhibit both ordered and chaotic motion. The invariant manifold structure organizes these behaviors and is a valuable tool for the design of spacecraft trajectories. The study of a system's dynamics often begins with the computation of its invariant tori (equilibrium points, periodic orbits, quasi-periodic orbits) and associated stable and unstable manifolds. Periodic orbits, in particular, have been used effectively for the design of low-energy transfers in the circular restricted 3-body problem (CR3BP). Quasi-periodic orbits offer similar benefits and are often more prevalent in the phase space, but additional complexities are involved in their computation. The foundation of this work is the development of a numerical method for computing two-dimensional quasi-periodic tori. The approach is applicable to a general class of Hamiltonian systems. Using a Fourier discretization and Gauss–Legendre collocation, a continuous representation of the torus is obtained. Included in the scheme is the computation of the torus's stable and unstable manifolds. These manifolds can then be used for the design of natural transfers. Two methods are presented for locating and continuing families of heteroclinic connections between quasi-periodic orbits in the CR3BP. A collocation-based approach for transitioning trajectories to a higher-fidelity ephemeris model is also included.

To my family.

ACKNOWLEDGMENTS

Reaching this point would not be possible without the support of many people. First and foremost, my advisor Prof. Dan Scheeres has helped me in innumerable ways from the moment I arrived in Colorado. His knowledge, guidance, and kindness has been fundamental to this research.

Second, I would like to thank Profs. Gerard Gómez and Josep Masdemont. They too have given me more support along the way than I could possibly repay. I can only hope to pass along some of what they have taught me during three memorable years in Barcelona.

I am also grateful to my committee, Profs. Elizabeth Bradley, James Meiss, Jeffrey Parker, and Hanspeter Schaub, for their time and input through the various stages of my PhD. A special thanks to Prof. George Born as well for his encouragement and humor along the way. In addition, I would like to thank Danny Dixon for showing me the joy of mathematics, and Prof. Kathleen Howell for introducing me to the world of astrodynamics.

To my friends and coworkers everywhere, this would not be possible without you. A special thanks to Dani Pérez-Palau for his kindness, and to Eric Brandner and Tyler Lulich for always being there for me.

Finally, to my family, thank you for everything. I cannot begin to express my appreciation for all that you have done for me.

CONTENTS

1 Introduction 1

1.1 Quasi-Periodic Invariant Tori 4

1.1.1 Representation and invariance 4

1.1.2 Reducibility 6

1.1.3 Hamiltonian setting 8

1.2 Computational Approaches 10

1.2.1 Solving boundary value problems 10

1.2.2 Computing quasi-periodic tori and their stability 12

1.2.3 Connecting orbits between tori 14

1.3 Contributions 15

2 Computing Tori in Hamiltonian Systems 17

2.1 Quasi-Periodic Boundary Value Problem 18

2.1.1 BVP for autonomous case 19

2.1.2 BVP for periodically-forced case 21

2.1.3 BVP for quasi-periodically forced case 22

2.1.4 Solution initialization 22

2.1.5 Lack of parameters 24

2.2 Unfolding Parameters 24

2.2.1 Action–angle coordinates 25

2.2.2 Unfolding for autonomous case 27

2.2.3 Unfolding for periodically-forced case . . . 30
2.3 Computation of Tori . . . 31
2.3.1 Fourier discretization . . . 32
2.3.2 Gauss–Legendre collocation . . . 33
2.3.3 Predictor–corrector implementation . . . 36
2.3.4 Error control . . . 37
2.3.5 Flow on torus . . . 38
2.4 Computation of Stability . . . 39
2.4.1 Extracting state-transition matrix . . . 39
2.4.2 Linear stability of torus . . . 41
2.4.3 Transition to full torus . . . 42

3 Invariant Tori in Astrodynamics 44
3.1 Circular Restricted Three-Body Problem . . . 44
3.1.1 Libration points . . . 46
3.1.2 Periodic orbits . . . 48
3.1.3 Quasi-periodic orbits . . . 50
3.2 Elliptic Restricted Three-Body Problem . . . 55
3.3 Hill Restricted Four-Body Problem . . . 56
3.3.1 HR4BP in Sun–Earth frame . . . 59
3.3.2 Motion near Earth–Moon collinear points . . . 61

4 Connections in the Restricted Three-Body Problem 67
4.1 Indirect Computation . . . 69
4.1.1 Locating and continuing connection . . . 69
4.1.2 Extracting boundary condition torus . . . 74
4.2 Direct Computation . . . 77
4.2.1 BVP for connection family . . . 78

4.2.2 Initializing family from planar connection 79
4.2.3 Geometry of Sun–Earth connection family 80

5 Transitioning to Solar System 86
5.1 Ephemeris Model 87
5.1.1 Prediction transformation 87
5.1.2 Correction minimization 89
5.2 Sample Orbits 90

6 Conclusion and Future Work 94
6.1 Contributions 94
6.2 Next Steps 96

Bibliography 98

LIST OF FIGURES

1.1 Genesis spacecraft trajectory (courtesy NASA/JPL–Caltech) 3

1.2 Dynamics on torus and in phase space 5

1.3 Invariant torus of flow with invariant circle of stroboscopic map 7

1.4 Illustration of a two-parameter torus family (see text) 9

1.5 Shooting (left) and collocation (right) methods before convergence 12

2.1 (a) Jacobian sparsity; ($b_{1,2}$) mesh block sparsity; ($c_{1,2}$) subblock sparsity. Diagonal lines represent diagonal nonzero elements. (See text for more details.) 35

2.2 Illustration of hyperbolic eigenvalue and eigenfunction 42

3.1 Libration points of the CR3BP (not to scale) 46

3.2 L_1 planar periodic orbits 49

3.3 L_2 planar periodic orbits 49

3.4 L_1 vertical periodic orbits 49

3.5 L_2 vertical periodic orbits 49

3.6 L_1 northern halo periodic orbits 50

3.7 L_2 northern halo periodic orbits 50

3.8 Members of quasi-halo torus family emanating from L_2 halo orbit 51

3.9 Tangent directions for stable and unstable manifolds of quasi-halo torus 52

3.10 Snapshots of L_2 quasi-halo unstable manifold departing away from Moon 52

3.11 Snapshots of L_2 quasi-halo stable manifold arriving from Moon's vicinity 53

3.12 Snapshots of L_1 Lissajous unstable manifold departing towards Earth 53

3.13 Crossings of $z = 0$ plane ($\dot{z} > 0$) of Earth–Moon L_1 (left) and L_2 (right) center manifold tori at a fixed energy level 54

3.14 CR3BP L_2 halo orbit family members (left) and corresponding ER3BP ($e = 0.1$) quasi-periodic tori (right). 56

3.15 Snapshots of ER3BP quasi-halo unstable manifold departing away from Moon. . . . 57

3.16 Sun–Earth L_1 and L_2 planar quasi-periodic orbits near 1:7 resonance with Moon . . 61

3.17 Bifurcation diagram of Earth–Moon L_1 dynamical substitute periodic orbits 62

3.18 Stroboscopic map of Earth–Moon L_1 planar quasi-periodic orbits (expanded view of 2:1 resonance region on right) 63

3.19 Bifurcation diagram of Earth–Moon L_2 dynamical substitute periodic orbits 65

3.20 Stroboscopic map of Earth–Moon L_2 planar quasi-periodic orbits (including 2:1 resonance region) 66

4.1 Steps 0, 200, 500, 1000 for locating first heteroclinic connection 70

4.2 Parameters for locating first heteroclinic connection 72

4.3 Earth–Moon L_2 to L_1 heteroclinic connection family from single L_2 quasihalo torus 73

4.4 Crossings of $z = 0$ plane near L_1 for connection family from L_2 torus 74

4.5 Interpolation of $z = 0$ plane crossings 75

4.6 Minimization functions for computing k and T 76

4.7 Invariant circles of section and stroboscopic map 77

4.8 Planar Sun–Earth L_2 to L_1 heteroclinic connections 81

4.9 Spatial connection family initial conditions at L_2 and final conditions at L_1 82

4.10 Sample connection from Sun–Earth L_2 Lissajous to L_1 Lissajous 84

4.11 Initial and final condition 2-sphere topology 85

4.12 Boundary condition amplitudes and transfer time 85

5.1 Sun–Earth L_1 Lissajous ephemeris orbit 90

5.2 Sun–Earth L_2 quasihalo ephemeris orbit 91

5.3 Earth–Moon L_2 quasihalo to L_1 Lissajous connection in ephemeris model 92

5.4 Earth–Moon L_2 quasihalo to L_1 quasihalo connection in ephemeris model 92

CHAPTER 1
INTRODUCTION

Spacecraft trajectory design often leverages simplified models such as the two-body and restricted three-body problems that incorporate relevant dynamics. These idealized models often possess special structure and admit solutions including equilibrium points and periodic orbits. Motion in the two-body problem consists of the well-known conic trajectories. However, the most common regular behavior in many astrodynamical systems including the restricted three-body problem is quasi-periodic motion. This motion takes place on the surface of two- or higher-dimensional invariant tori within the phase space. From a dynamical systems perspective, invariant tori and their associated stable and unstable manifolds provide a framework for the system's dynamics [Simó, 1998]. This is one of the primary motivations for the study of invariant solutions in the design of space missions. A focus of the current work is on numerically computing quasi-periodic orbits and their associated manifolds as well as investigating their astrodynamical applications.

While quasi-periodic solutions are inherently more complex than equilibrium points and periodic orbits (zero- and one-dimensional tori, respectively), their higher dimension along with their family structure can be advantageous. Let us first consider the circular restricted three-body problem (CR3BP). Though there are only five libration points, there is a continuous family of periodic orbits, which can nominally be parameterized by the Jacobi constant, the system's integral of motion. This provides many more trajectory options, and hence, periodic orbits are often of greater interest for mission design. In an analogous manner, while there are isolated periodic orbits at a fixed Jacobi constant value, there are entire families of quasi-periodic orbits. This is one of the principal benefits of studying quasi-periodic solutions: their higher-parameter families along with

their higher dimension means they are much more prevalent within the phase space. Ultimately, considering quasi-periodic orbits allows the available trajectory design space to be expanded.

The benefit of the quasi-periodic orbit family structure is particularly apparent for designing transfers. Families of hyperbolic periodic orbits are two-dimensional and often have three-dimensional stable and unstable manifolds, which asymptotically approach or depart the periodic orbit at no fuel cost. This dynamical property is beneficial for the design of low-energy transfers [Gómez et al., 1993; Howell et al., 1997; Parker & Anderson, 2013]. On the other hand, two-dimensional hyperbolic invariant tori, which contain quasi-periodic motion on their surfaces, lie in four-dimensional families with five-dimensional stable and unstable manifolds. Therefore, including quasi-periodic orbits greatly expands the transfer space; there are many more options for putting a spacecraft on a stable or unstable manifold. Furthermore, intersections between manifolds, corresponding to heteroclinic and homoclinic connections, are more common. These connections are natural in that no maneuver is necessary to transition between two solutions. The connections can subsequently be combined into "chains" to visit various regions of space.

Beyond their use for transfers, invariant tori are beneficial in their own right. Periodic and quasi-periodic orbits may have properties beneficial for meeting a mission's science objectives and technical requirements [Belló et al., 2010]. For example, an Earth–Moon L_2 libration point orbit has been proposed as a communications link between the Earth and the far side of the Moon [Farquhar, 1967]. The Genesis mission orbited the Sun–Earth L_1 libration point orbit to collect solar wind samples [Lo et al., 1998]. The spacecraft's trajectory is shown in Figure 1.1. The upcoming James Webb Space Telescope will orbit the Sun–Earth L_2 libration point [Gardner et al., 2006]. Given the prevalence of quasi-periodic orbits, considering them as candidate trajectories may allow a designer to better balance competing mission requirements. In addition, quasi-periodic orbits have applications to formation flying. They enable a collection of spacecraft to have organized relative behavior using only natural dynamics.

For three-body motion, the natural extension of the CR3BP is to allow the primary bodies to move on elliptical orbits, the so-called elliptic restricted three-body problem (ER3BP). For

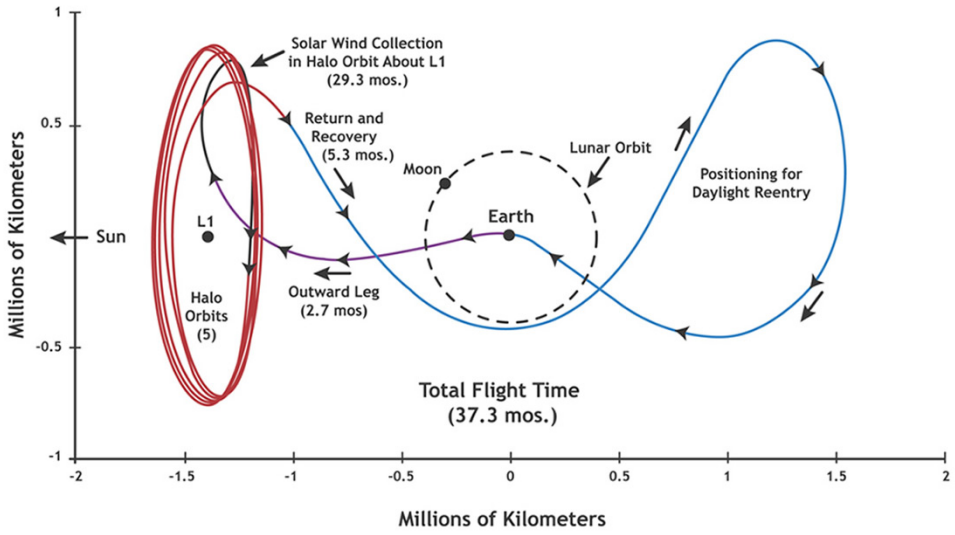

Figure 1.1: Genesis spacecraft trajectory (courtesy NASA/JPL–Caltech)

particularly elliptical systems, it may be beneficial to take the eccentricity into account early in the mission design process. Unlike the one-parameter families of periodic orbits in the CR3BP, periodic orbits of the ER3BP are isolated since they must be resonant with the primary bodies. Generally speaking, periodic orbits in the CR3BP become two-dimensional quasi-periodic orbits in the ER3BP [Jorba & Villanueva, 1997b]. These quasi-periodic orbits fill a similar role to the CR3BP periodic orbits, and they lie in nearly continuous one-parameter families.

The CR3BP and ER3BP are just two examples of astrodynamical systems where quasi-periodic motion appears. Other examples include Hill's three-body problem, various four-body problems, and the small-body orbiter problem. Therefore, the study of general purpose methods for computing these solutions and their associated manifolds could have broad applicability. It is important to note that in higher-fidelity or ephemeris models, invariant solutions no longer exist. However, a "shadow" of them often persists and following a nearby trajectory can be possible [Gómez et al., 2001a]. This behavior validates the use of simplified models in the mission design process.

1.1 QUASI-PERIODIC INVARIANT TORI

To introduce quasi-periodic motion in a general context, consider a vector field $\mathbf{f}_0$ on the space of states $\mathbf{x} \in \mathbb{R}^n$. The vector field may depend on a set of angles $\boldsymbol{\theta} \in \mathbb{T}^d \equiv \mathbb{S}^1 \times \cdots \times \mathbb{S}^1$ (d times) that change at constant rates $\boldsymbol{\omega} \in \mathbb{R}^d$. In this document, for convenience we will use $\mathbb{T}^1 \equiv \mathbb{S}^1 \equiv \mathbb{R}/\mathbb{Z}$ meaning we parameterize angles on the unit interval; therefore, $\boldsymbol{\theta} \equiv \boldsymbol{\theta} + \mathbf{k}$ for any $\mathbf{k} \in \mathbb{Z}^d$. In other words, angles are nominally in the range $[0, 1)$ rather than $[0, 2\pi)$. The system's equations of motion are

$$\dot{\mathbf{x}} = \mathbf{f}_0(\mathbf{x}, \boldsymbol{\theta}) \tag{1.1a}$$

$$\dot{\boldsymbol{\theta}} = \boldsymbol{\omega}. \tag{1.1b}$$

We do not require that each angle θ_i appears explicitly in the vector field $\mathbf{f}_0$. When an angle does appear explicitly, however, it signifies an external forcing applied to the system. Thus, the setting encompasses autonomous, periodically-forced, and quasi-periodically-forced motion. Furthermore, we do not require that each frequency ω_i is fixed a priori. Note we do not lose generality (in terms of the class of system considered) by mandating that each angle changes at a constant rate, but this choice sets a particular parameterization of the motion.

1.1.1 Representation and invariance

To make the computational procedure more concrete, we will focus on two-dimensional invariant tori of (1.1). Let $d = 2$, thus angle vector $\boldsymbol{\theta} \equiv (\theta_1, \theta_2)$ and frequency vector $\boldsymbol{\omega} \equiv (\omega_1, \omega_2)$ are two-dimensional. We represent a torus in our dynamical system using a "torus function" $\mathbf{v}(\cdot) : \mathbb{T}^2 \to \mathbb{R}^n$, which parameterizes the states on the torus using the angles $\boldsymbol{\theta}$. In order for the torus to be invariant, the motion on the torus must be consistent with the vector field $\mathbf{f}_0$. Substituting this torus function into equation (1.1a) by setting $\mathbf{x} = \mathbf{v}(\boldsymbol{\theta})$ and including equation (1.1b) after applying the chain rule give the invariance equation

$$\omega_1 \frac{\partial \mathbf{v}}{\partial \theta_1}(\boldsymbol{\theta}) + \omega_2 \frac{\partial \mathbf{v}}{\partial \theta_2}(\boldsymbol{\theta}) = \mathbf{f}_0(\mathbf{v}(\boldsymbol{\theta}), \boldsymbol{\theta}), \tag{1.2}$$

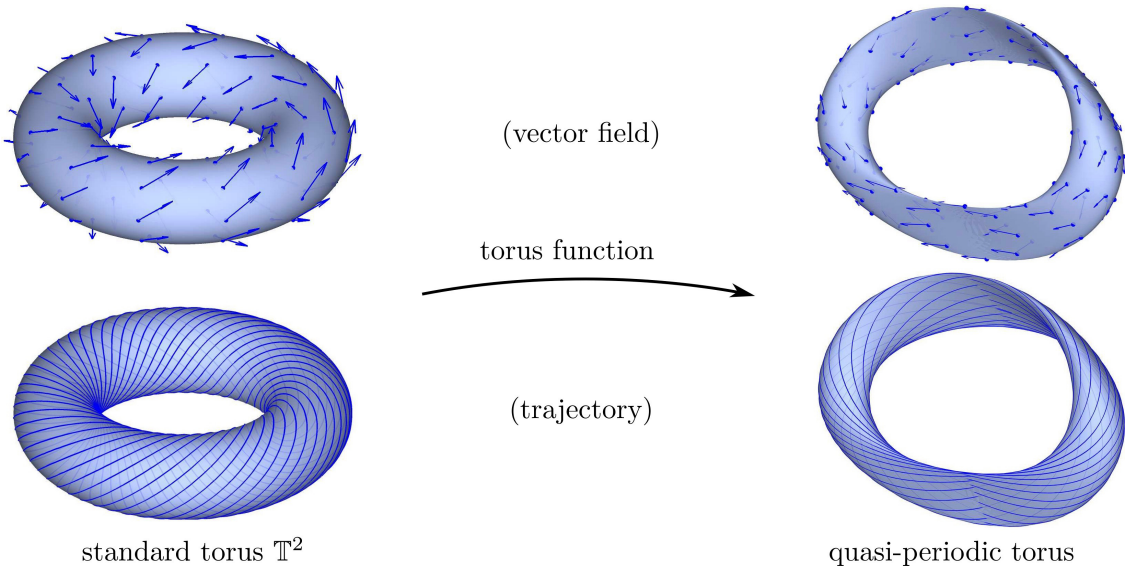

Figure 1.2: Dynamics on torus and in phase space

which must hold for all $\boldsymbol{\theta} \in \mathbb{T}^2$. An implicit assumption is that any angle that explicitly appears in the vector field corresponds to an angle parameterizing the torus. This is done to simplify the presentation. Alternatively, $\mathbf{f}_0(\mathbf{v}(\boldsymbol{\theta}), \mathbf{P}\boldsymbol{\theta})$ could be used in (1.2) where $\mathbf{P} \in \mathbb{Z}^{2\times 2}$ is a nonsingular integer matrix.

We assume that the frequency vector is not resonant, in other words, for $\mathbf{k} \in \mathbb{Z}^2$, $\langle \mathbf{k}, \boldsymbol{\omega} \rangle = 0$ only if $\mathbf{k} = \mathbf{0}$, where the operator $\langle \cdot, \cdot \rangle$ denotes the inner product (dot product). A quasi-periodic orbit $\mathbf{v}(\boldsymbol{\theta}_0 + \boldsymbol{\omega} t)$ must then densely cover the surface of the torus $\mathbf{v}(\mathbb{T}^2)$. Since the closure of the quasi-periodic orbit is an invariant torus, we will occasionally use the terms interchangeably. For certain problems, we will know the frequency vector; for other problems, we will need to determine one or both of the frequencies.

An illustration of the torus function $\mathbf{v}$ is provided in Figure 1.2 (from [Olikara, 2010]). Since the vector field $\mathbf{f}_0$ is a linear combination of $\partial \mathbf{v}/\partial \theta_1$ and $\partial \mathbf{v}/\partial \theta_2$, it is tangent to the torus surface. The parallel flow $\boldsymbol{\theta}_0 + \boldsymbol{\omega} t$ on the standard torus $\mathbb{T}^2$ is mapped to a quasi-periodic orbit. Note that for a phase space of dimension $n > 3$, a projection of the invariant torus onto three-dimensional space can intersect itself, as seen in the figure, but this self-intersection is only of the projection and not the torus itself.

The invariance condition (1.2) must hold over the entire two-dimensional torus surface. We can, however, reduce the dimension of the invariance condition. This reduction is done by converting the flow to a stroboscopic map $\boldsymbol{\varphi}$ with an associated time $T = 1/\omega_1$ (recall angles are parameterized over the unit interval). Fixing an initial value for θ_1 and integrating the flow for time T leaves $\theta_1 \equiv \theta_1 + 1$ unchanged and gives the map $(\mathbf{x}, \theta_2) \mapsto (\bar{\mathbf{x}}, \bar{\theta}_2)$ defined by

$$\bar{\mathbf{x}} = \boldsymbol{\varphi}(\mathbf{x}, \theta_2; T, \rho) \tag{1.3a}$$

$$\bar{\theta}_2 = \theta_2 + \rho. \tag{1.3b}$$

Instead of using the frequency vector (ω_1, ω_2) explicitly in (1.3), the map is given as a function of the rotation number $\rho := T\omega_2 = \omega_2/\omega_1$. From the assumption that ω_1 and ω_2 are not resonant, ρ will be irrational.

Considering the stroboscopic map (1.3), the problem now becomes finding a one-dimensional invariant torus (an invariant circle) described by the "circle function" $\mathbf{w}(\cdot) := \mathbf{v}(\theta_1, \cdot) : \mathbb{T}^1 \to \mathbb{R}^n$. Substituting this function into the map gives the invariance equation

$$\mathbf{w}(\theta_2 + \rho) = \boldsymbol{\varphi}(\mathbf{w}(\theta_2), \theta_2; T, \rho), \tag{1.4}$$

which must hold for all $\theta_2 \in \mathbb{T}^1$. We can write this equation simply as $\mathbf{w}(\theta_2 + \rho) = \boldsymbol{\varphi}(\mathbf{w}(\theta_2))$ when the dependencies on the problem variables are understood. Since the rotation number corresponds to a frequency vector that is not resonant, the trajectory $\mathbf{w}(\theta_{2,0} + k\rho)$, $k \in \mathbb{Z}_+$, will densely cover the invariant circle $\mathbf{w}(\mathbb{T}^1)$. An invariant circle on a two-dimensional torus is shown in red in Figure 1.3.

1.1.2 Reducibility

Similar to equilibrium points and periodic orbits, quasi-periodic orbits can have stable and unstable motion in their vicinity. For example, a two-dimensional hyperbolic torus in the CR3BP has three-dimensional stable and unstable manifolds. Linearizing the map (1.3) about a quasi-periodic solution

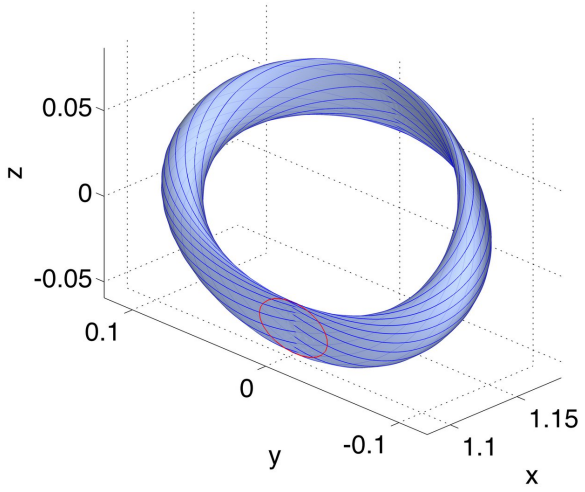

Figure 1.3: Invariant torus of flow with invariant circle of stroboscopic map

$\mathbf{w}$ gives

$$\delta\bar{\mathbf{w}} = \frac{\partial\boldsymbol{\varphi}}{\partial\mathbf{x}}(\mathbf{w}(\theta_2))\,\delta\mathbf{w} \tag{1.5a}$$

$$\bar{\theta}_2 = \theta_2 + \rho. \tag{1.5b}$$

Since the matrix $\partial\boldsymbol{\varphi}/\partial\mathbf{x}$ varies with location $\mathbf{w}(\theta_2)$ on the circle, it does not directly provide stability information. However, assuming a coordinate change $\delta\mathbf{w}(\cdot) \mapsto \delta\mathbf{w}_0(\cdot)$ exists such that this linearized equation can be transformed into

$$\delta\bar{\mathbf{w}}_0 = \mathbf{B}\,\delta\mathbf{w}_0 \tag{1.6a}$$

$$\bar{\theta}_2 = \theta_2 + \rho, \tag{1.6b}$$

where $\mathbf{B} \in \mathbb{R}^{n\times n}$ is a constant matrix, the torus is termed "reducible" [Jorba, 2001]. We will use this property when analyzing stability. The so-called Floquet matrix $\mathbf{B}$ fills a role similar to the monodromy matrix of a periodic orbit. In the computational method that will be presented, we will not directly compute $\mathbf{B}$. We will, however, determine its eigenvalues, which provide linear stability information.

1.1.3 Hamiltonian setting

The astrodynamical systems, such as the CR3BP and the ER3BP, in which we are interested are examples of Hamiltonian systems. These systems share many dynamical properties, which allow us to design computational techniques that are applicable to Hamiltonian systems in general without restricting ourselves to a particular example.

A Hamiltonian system's dynamics are specified by its Hamiltonian function $\bar{H}(\mathbf{q}, \mathbf{p}, \boldsymbol{\theta})$.[1] The function depends on the generalized coordinates $\mathbf{q} \in \mathbb{R}^{\bar{n}}$, the generalized momenta $\mathbf{p} \in \mathbb{R}^{\bar{n}}$, and possibly a set of angles $\boldsymbol{\theta} \in \mathbb{T}^d$. Hamilton's equations provide corresponding equations of motion:

$$\dot{\mathbf{q}} = +\frac{\partial \bar{H}}{\partial \mathbf{p}}^{\intercal} \tag{1.7a}$$

$$\dot{\mathbf{p}} = -\frac{\partial \bar{H}}{\partial \mathbf{q}}^{\intercal} \tag{1.7b}$$

$$\dot{\boldsymbol{\theta}} = \boldsymbol{\omega} \tag{1.7c}$$

where $\boldsymbol{\omega} \in \mathbb{R}^d$ are the constant rates of change of the angles. (Recall that in this document we will focus on the case $d = 2$.) If the angles do not appear explicitly in in the Hamiltonian function, then $\bar{H}$ is an integral of motion. For an introduction to Hamiltonian dynamics, see Lanczos [1986] and Meyer & Hall [1992].

While the form of Hamilton's equations (1.7) is dependent on the canonical coordinate set $(\mathbf{q}, \mathbf{p})$, the solution structure is not. For example, the CR3BP is a Hamiltonian system, but it is often expressed in terms of a non-canonical coordinate set $(\mathbf{q}, \dot{\mathbf{q}})$, the position and velocity in a rotating frame. The existence of invariant tori and their stability properties are independent of the coordinate choice. For generality, we consider a state $\mathbf{x} \in \mathbb{R}^n$, $n := 2\bar{n}$, which is not necessarily canonical, with the Hamiltonian $H(\mathbf{x}, \boldsymbol{\theta})$ expressed in these coordinates.

An extensive theory known as Kolmogorov–Arnold–Moser theory [Broer et al., 1996; Jorba & Villanueva, 1997a; Llave, 2001] deals with properties of quasi-periodic solutions to equations (1.1) and (1.3). While the current work is focused on the computation and application of the solutions, some

[1] In the most general context, the Hamiltonian function can depend on time t in an arbitrary manner, $\tilde{H}(\mathbf{q}, \mathbf{p}, t)$, but we restrict ourselves to a form consistent with the existence of invariant tori.

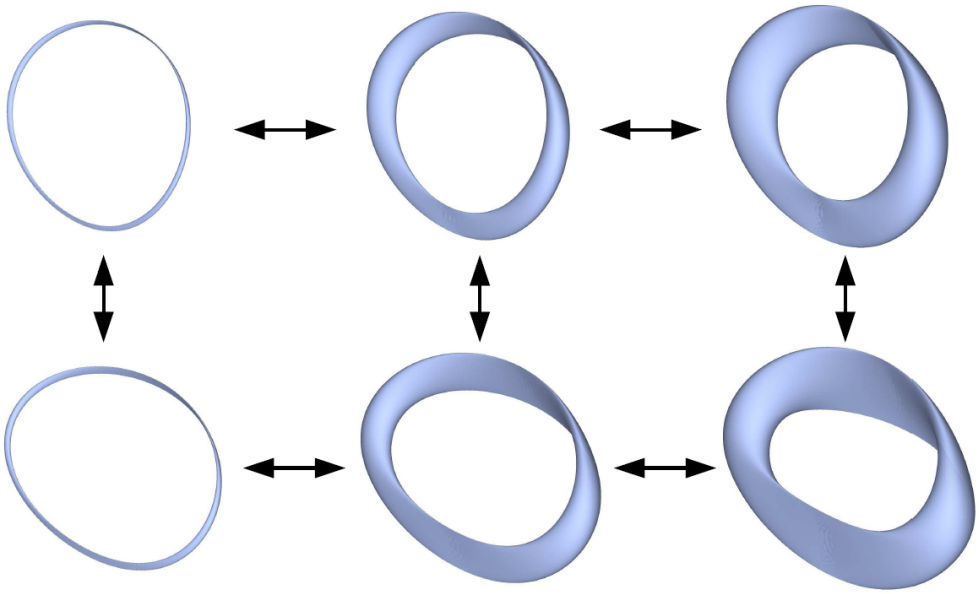

Figure 1.4: Illustration of a two-parameter torus family (see text)

aspects of the theory are relevant to this work. We are particularly interested in the family structure of the tori. Assuming a d-dimensional quasi-periodic torus exists, for an autonomous Hamiltonian dynamical system that depends on r external parameters, the torus (up to a maximum dimension of $\bar{n}$) will lie in a $(d+r)$-parameter family. For example, without any free external parameters, two-dimensional tori in the CR3BP lie in two-parameter families. In general, each torus can be identified by a pair of frequencies. A qualitative illustration of a two-parameter family is shown in Figure 1.4 (from Olikara [2010]); moving in each of the directions (horizontally or vertically), one of the two frequencies is constant. For the ER3BP, one of the torus's frequencies is fixed by the period of the primary bodies. If the eccentricity of the primary bodies is constrained, two-dimensional tori lie in one-parameter families. It should be noted that due to the behavior near resonances, the actual families of tori belong to Cantor sets. However, the gaps in these sets are often "exponentially small," and the family can be extended to a smooth manifold.

1.2 COMPUTATIONAL APPROACHES

Given their important role in dynamical systems in general (and astrodynamics in particular), various computational techniques have been developed for computing invariant tori and connecting orbits. Many of these techniques are based around the formulation of an appropriate boundary value problem that is then solved numerically. In this section, we provide an overview of the main approaches with a particular focus on those relevant to problems in astrodynamics.

1.2.1 Solving boundary value problems

Given an ordinary differential equation, such as the CR3BP equations of motion, we often seek trajectory segments that satisfy certain boundary conditions. In the simplest case, a so-called initial value problem, there is a prescribed initial state. Since there is in general no closed form solution, we must produce an approximation. For example, a Runge–Kutta integrator will evaluate the vector field (which provides the first-order derivative of the state) multiple times for each time step to produce a higher-order approximation. The procedure is then repeated to produce additional time steps along the trajectory.

A boundary value problem (BVP) has constraints on both the initial and final states of a trajectory. For instance, when computing a periodic orbit, the initial state is not explicitly specified but rather constrained to match the final state. Typically, however, we assume that an approximate initial state and time period is available. Using a single shooting method, the initial state is integrated along with the first-order variational equations, and an error in the boundary conditions is computed. Using a Newton method, a linear system is solved to update the initial conditions and time period, and the procedure repeats iteratively. One of the primary drawbacks is that the initial guess needs to be sufficiently accurate, or the procedure will not converge. Furthermore, since the integrator is only accurate to a certain order and the computations are done in finite precision, some trajectories are too unstable to ever converge with single shooting.

Multiple shooting improves on single shooting by distributing the instabilities along the

trajectory. The trajectory is split into multiple segments starting from a sequence of points, and each of these initial conditions is integrated separately (which can be done in parallel on a computer). Then the Newton method computes linear updates to all the points and repeats until the trajectory is continuous and the boundary conditions are satisfied. Multiple shooting can partially mitigate the the instabilities as a function of the number of segments into which the trajectory is split. Note that there is a corresponding increase in the size of the linear system that must be solved at each iteration.

With a shooting method, we essentially follow the flow of the vector field and then iterate to satisfy continuity and boundary constraints. On the other hand, with a collocation method we start with a continuous trajectory, and then iterate such that it matches the vector field and boundary constraints. This has implications on the numerical stability of the method. The trajectory is discretized as a continuous, piecewise polynomial as a function of time. Constraints are incorporated such that the derivative at a set of collocation points matches the vector field. Common choices of the collocation points are the Gauss–Lobatto points and Gauss–Legendre points (such as used in the AUTO software [Doedel et al., 1991]). As before, a Newton method is used to converge to a solution. Collocation methods will be presented in more detail in Chapter 2.

From one perspective, a collocation method may be viewed as a limiting case of multiple shooting where each trajectory segment is a single step of an (implicit) integrator. It is, however, more insightful to view collocation as a method in its own right considering the greater control of the error and the trajectory (we can, for example, include constraints that depend on an integral along the trajectory) that is available. Furthermore, with a collocation method the entire continuous, piecewise polynomial is updated at each iteration. An illustration of shooting and collocation methods for computing a periodic orbit is shown in Figure 1.5. Before convergence, a shooting method exactly follows the vector field (up to the order of the numerical integrator) but is not periodic. A collocation trajectory, on the other hand, is exactly periodic but does not match the vector field at the collocation points until convergence. Note that a numerical integrator is not used for any part of the collocation scheme. An overview of the theory and methods for numerically

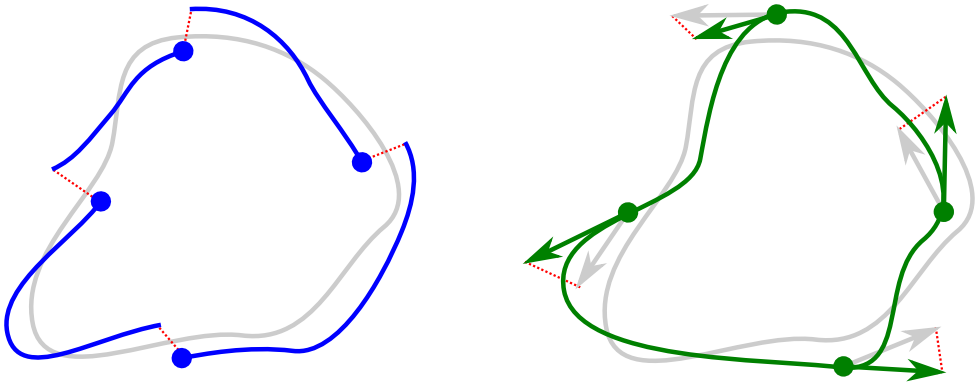

Figure 1.5: Shooting (left) and collocation (right) methods before convergence

solving boundary value problems can be found in Ascher et al. [1995].

1.2.2 Computing quasi-periodic tori and their stability

A variety of methods are available for computing quasi-periodic tori in general dynamical systems (see [Haro & de la Llave, 2006; Jorba & Olmedo, 2009] for methods including stability information and references therein). Many of these approaches have been developed for fully-forced systems, i.e., systems where the vector field depends explicitly on the angles that parameterize the torus. However, many astrodynamical systems including the CR3BP and ER3BP do not belong to this class of systems.

Motivated by trajectory design applications, analytical work from the 1970s includes Farquhar & Kamel's [1973] third-order expansion of orbits in the vicinity of the Earth–Moon L_2 libration point using a Poincaré–Lindstedt method. During the same time period, Richardson & Cary [1975] developed a third-order approximation of quasi-periodic motion near the Sun–Earth L_1 and L_2 libration points via the method of multiple time scales. More recent semi-analytical work leverages computer algebra tools. Gómez et al. [1998] use a Poincaré–Lindstedt method to generate high-order quasi-halo orbit expansions. Jorba & Masdemont [1999] investigate the dynamics around the libration points using center manifold reduction. These local methods offer a thorough view of the dynamics in the libration point vicinity, but they are limited by their regions of convergence. Specialized algebraic manipulators are often required as well, which can be an implementation obstacle.

In the 1980s Howell & Pernicka [1988] presented a numerical shooting approach for correcting approximate quasi-periodic orbits in the CR3BP, though without explicit control of orbit parameters. Gómez & Mondelo [2001b] later developed a multiple shooting scheme for computing two-dimensional quasi-periodic tori by using an invariant circle parameterized by Fourier coefficients of the stroboscopic map (1.4). Kolemen et al. [2011] use a similar approach except with multiple Poincaré sections selected based on a knowledge of the torus shape and directly parameterizing the invariant circles using states, though it lacks explicit control of the torus frequencies. A general purpose shooting-based scheme for computing tori parameterized by states is presented in Olikara & Scheeres [2012]. Alternatively, for general dynamical systems a method presented by Schilder et al. [2005] is available to compute a torus of a flow directly by solving invariance equation (1.2). This flow method has been applied to the CR3BP [Olikara, 2010]; however, this requires dealing with a torus of dimension one larger than the torus of an associated map. Some comparisons of the methods are available in Baresi et al. [2016].

For computing the stability of tori, Jorba [2001] introduces a numerical approach based on the eigenvalues of a large, dense matrix. Mondelo et al. [2009] and Olikara & Scheeres [2012] use this scheme for generating stable and unstable manifolds in the CR3BP. Jorba & Olmedo [2009] also have an efficient method that combines the torus and stability computations, but it is specific to nonautonomous systems with known forcing frequencies.

While a large part of the applications within astrodynamics focus on the CR3BP, special solutions in the ER3BP have also been considered. Early analytic expansions [Farquhar & Kamel, 1973; Richardson & Cary, 1975] included the eccentricity of the primary bodies, and more recently periodic orbits have been numerically investigated [Campagnola et al., 2008]. Unlike the CR3BP, these orbits are isolated since most periodic orbits that persist become quasi-periodic orbits with the influence of eccentricity. Additional examples of quasi-periodic orbits appearing in periodically forced systems can be found in the four-body problems [Andreu, 1999; Castella & Jorba, 2000].

1.2.3 Connecting orbits between tori

An important class of solution associated with invariant tori (equilibrium points, periodic orbits, and quasi-periodic orbits) are connecting orbits. Heteroclinic connections are possible between hyperbolic tori of the same or different dimension and occur when the unstable manifold of one torus intersects the stable manifold of another in the phase space. The special case where the tori are the same is a homoclinic connection. These solutions have been investigated in the planar CR3BP between periodic orbits, and they are often found using a surface of section. For use in the design of low-energy trajectories, these connections can be joined to form chains traversing a periodic orbit sequence [Koon et al., 2000; Canalias et al., 2006; Parker et al., 2010].

Due to the increased dimension, the situation becomes significantly more complex when the spatial CR3BP is considered. With a four-dimensional surface of section, visual tools are more difficult to use. It becomes challenging to detect whether an intersection occurs, especially since connections involving quasi-periodic orbits are possible. However, Gómez et al. [2004] studied the center manifold semi-analytically and were able to locate sample heteroclinic connections between quasi-periodic orbits by propagating a large set of trajectories and taking advantage of the center manifold's geometry. A family of connections in the spatial Hill's restricted three-body problem was studied by Arona & Masdemont [2007], and a theoretical foundation was presented in Delshams et al. [2008].

An alternative approach presented by Calleja et al. [2012] computes a hyperbolic periodic orbit and indirectly finds a connection to a quasi-periodic orbit. The main idea is that an approximate connection departing the periodic orbit will wind around a quasi-periodic orbit many times before leaving and intersecting an appropriate surface of section; hence, the time to reach the section will be long. By computing a trajectory in the periodic orbit's unstable manifold using a collocation method and using continuation to increase the time to reach the section, a connection is located indirectly. The formulation of Calleja et al. is specific to periodic-to-quasi-periodic orbit connections, which are demonstrated to exist in families parameterized by Jacobi constant.

1.3 CONTRIBUTIONS

In this section we highlight the primary contributions to the existing body of research. While relevant theoretical aspects of quasi-periodic solutions are considered, the goal of the work is primarily pragmatic in nature. We seek to present tools that could be useful to practitioners in various fields as well as representative results in astrodynamical systems.

Flexible torus computation scheme: The foundation of this work is a fully numerical method for computing families of quasi-periodic tori and their associated stable and unstable manifolds in Hamiltonian systems. The scheme is presented in Chapter 2 and applicable both to autonomous systems and systems with forcing. Many concepts follow the approach of Olikara & Scheeres [2012] but rather than using a shooting method, a Gauss–Legendre collocation method is used. This allows a complete representation of the entire torus to be obtained. In addition, we incorporate a set of solution and continuation constraints that are broadly applicable. This allows the method to be used basically unchanged between families of solutions and in a variety of systems. Included in the approach is the computation of the torus's stability. For hyperbolic tori, their stable and unstable directions are obtained over the entire torus surface.

Tori in astrodynamics: To demonstrate the computational procedure, in Chapter 3 we include examples in astrodynamical systems. Due to their significance for mission design applications, we first produce two-dimensional tori in the CR3BP along with their stability. Given the general purpose nature of the method, results in less studied systems are also included. We show how periodic orbits in the CR3BP become two-dimensional tori in the ER3BP. As an extended analysis following Olikara et al. [2016], we consider planar motion in the Hill restricted four-body problem (HR4BP), where the influence of the Sun, Earth, and Moon are included.

Connecting orbits between tori: We investigate the computation of heteroclinic connections between tori in the spatial CR3BP in Chapter 4. We present both indirect and direct computational approaches. The approach for finding initial connecting orbits originating from a periodic orbit described in

Calleja et al. [2012] can be extended to finding orbits originating from a quasi-periodic orbit. This connection can then be continued to generate a family of quasi-periodic-to-quasi-periodic connections, which will offer natural transfer options for a spacecraft. Since the method is indirect, we will also investigate whether a representation of the destination torus can be extracted. We then formulate a boundary value problem for the direct computation of connections. A complete two-parameter family of connecting orbits at a fixed energy level in the Sun–Earth system is presented.

High-fidelity modeling: An important question that arises in the computation of invariant solutions and the use of idealized models is whether the solutions are in fact "real." The existence of a quasi-periodic orbit in the CR3BP can be studied rigorously using KAM theory, but the precise family structure is of less importance from a mission design perspective. The pragmatic approach is to see whether a nearby solution exists in a high-fidelity model. Specifically, we will illustrate in Chapter 5 that quasi-periodic orbits and associated connecting orbits in the CR3BP can often be transitioned to an ephemeris model. This will help to validate the study of these solutions for spacecraft trajectory design. This is formulated as an optimization problem to find the closest similar trajectory.

CHAPTER 2

COMPUTING TORI IN HAMILTONIAN SYSTEMS

In this chapter we present a general-purpose scheme for computing families of quasi-periodic invariant tori in Hamiltonian systems. To make the exposition concrete, we focus on two-dimensional tori. Most aspects, however, should generalize in a natural manner for the computation of higher-dimensional tori. The approach is applicable to systems with at least two degrees of freedom ($n \geq 4$). For systems with more than two degrees of freedom, two-dimensional tori are not maximal and can have elliptic or hyperbolic motion (or a combination of these) normal to their families. We do not assume a certain stability type.

We will formulate boundary value problems for computing tori in autonomous, periodically-forced, and quasi-periodically forced Hamiltonian systems. For the first two cases, the torus families have a non-generic structure. Entire families of solutions exist without any external parameters. We introduce additional unfolding parameters so that the Hamiltonian system appears generic. This allow us to have the same number of parameters as constraints in the boundary value problems.

The computation provides a complete parameterization of the two-dimensional torus. This is done using a combination of Fourier discretization and Gauss–Legendre collocation. Since the discretized equations are solved using a Newton method, the problem is constructed so as to maximize the sparsity of the associated Jacobian matrix, which allows for an efficient solution.

The tools in this chapter are numerical in nature. We do not attempt to rigorously prove the existence of the quasi-periodic tori, which would require KAM techniques and consideration of the fine Cantor-like structure of the families. We do, however, provide an error estimate in the torus computation and additional Fourier modes can be added to reduce the error. For practical purposes,

such as spacecraft trajectory design, this should be sufficient considering the tori themselves exist in simplified models such as the circular restricted three-body problem.

As a by-product of the quasi-periodic torus computation scheme, we are able to determine the linear stability of the torus. In particular, we can extract this information from the Jacobian matrix used for the Newton method. For hyperbolic tori, this allows us determine the stable and unstable directions at each point on the torus's surface, which can then be used to generate the associated stable and unstable manifolds.

In many ways the special structure of Hamiltonian systems makes the computation of invariant tori more challenging than in a generic dynamical system. In this chapter, these difficulties are resolved via the unfolding parameters such that the original Hamiltonian system is embedded in a family of generic dynamical systems. Therefore, while we focus on quasi-periodic orbits in Hamiltonian systems, the methods presented here should be directly applicable to systems lacking this structure.

2.1 QUASI-PERIODIC BOUNDARY VALUE PROBLEM

We now construct a boundary value problem such that the solution is a two-dimensional quasi-periodic torus. Following the introduction to quasi-periodic solutions in Section 1.1, we match the flow on the torus to the vector field making the torus invariant. We incorporate constraints to provide a unique representation of the torus. These constraints serve two purposes. In many situations the tori are not isolated but lie in a family. One purpose is to select a particular quasi-periodic torus from within a one- or more-parameter family of tori. The second purpose is to provide a unique parameterization of a particular torus. For example, the phases of a torus's angles in an autonomous system are free and need to be constrained.

We consider three settings: autonomous, periodically-forced, and quasi-periodically-forced Hamiltonian systems. Depending on the situation, we will include arbitrary internal parameters to have a system that is well-posed. In Section 2.2, we will formalize the choice of these parameters.

2.1.1 BVP for autonomous case

We begin by considering the autonomous Hamiltonian setting. For this case, we expect two-dimensional tori to lie in two-parameter families [Jorba & Villanueva, 1997a]. We will thus need two scalar constraints to identify a particular two-dimensional torus. Since neither angle parameterizing the torus appears explicitly in the autonomous Hamiltonian, we will need two phase constraints to fix the representation.

Starting from invariance equation (1.4), we construct the boundary value problem. In this form, we are looking for a circle that is invariant under a stroboscopic map. The stroboscopic map is defined by the vector field's flow over a time interval T, which will be rescaled to 1. This leads us to look for a "cylinder function" of the form $\mathbf{u} : [0,1] \times \mathbb{T}^1 \to \mathbb{R}^n$ along with applicable parameters. For each $\theta_2 \in \mathbb{T}^1$, $\mathbf{u}(\,\cdot\,;\theta_2)$ represents an individual trajectory from initial condition $\mathbf{u}(0;\theta_2)$; i.e., function $\mathbf{u}$ is defined such that θ_2 corresponds to the angle on the initial invariant circle, and θ_2 is constant along a given trajectory. By identifying the ends of the cylinder, it becomes topologically a torus. The vector field and quasi-periodicity condition are

$$\frac{d\mathbf{u}}{d\tau}(\tau;\theta_2) = T\mathbf{f}(\mathbf{u}(\tau;\theta_2),(\tau,\theta_2+\rho\tau);\lambda_1,\lambda_2), \tag{2.1a}$$

$$\mathbf{u}(0;\theta_2) = \mathbf{u}(1;\theta_2-\rho) \tag{2.1b}$$

for all $\tau \in [0,1]$, $\theta_2 \in \mathbb{T}^1$. Rescaled time τ is on the unit interval since the vector field $\mathbf{f}$ is scaled by T, which also allows stroboscopic time T to appear explicitly as a parameter. Note that in the autonomous case, the angles $(\tau, \theta_2 + \rho\tau)$ will not appear explicitly in $\mathbf{f}$, but are included in (2.1a) since we will use the same formulation when forcing is present. The first angle of these angles matches the rescaled time τ. The term $\rho\tau$ is included in the the second angle to incorporate its change from its initial value θ_2. The condition (2.1b) guarantees quasi-periodicity when rotation number ρ is irrational. We then add the following four scalar constraints:

$$\int_0^1 \left\langle \mathbf{u}(0;\theta_2) - \tilde{\mathbf{u}}(0;\theta_2),\, \frac{d\tilde{\mathbf{u}}}{d\tau}(0;\theta_2) \right\rangle d\theta_2 = 0, \tag{2.1c$_1$}$$

$$\int_0^1 \left\langle \mathbf{u}(0;\theta_2) - \tilde{\mathbf{u}}(0;\theta_2),\, \frac{\partial\tilde{\mathbf{u}}}{\partial\theta_2}(0;\theta_2) \right\rangle d\theta_2 = 0 \tag{2.1c$_2$}$$

$$\int_0^1 H(\mathbf{u}(0;\theta_2))\,d\theta_2 = \tilde{H} \tag{2.1d$_1$}$$

$$\int_0^1 \big\langle \mathbf{u}(0;\theta_2) - \tilde{\mathbf{u}}(0;\theta_2),\, \tilde{\mathbf{u}}'(0;\theta_2)\big\rangle\,d\theta_2 = \Delta s. \tag{2.1d$_2$}$$

All of these constraints are functions of the initial invariant circle $\mathbf{u}(0;\,\cdot\,)$ and are integrated around it. (Recall that the angles are nominally parameterized on the unit interval.) They are defined with respect to a nearby, previously computed torus in the family represented by function $\tilde{\mathbf{u}}$. The first two constraints, (2.1c$_1$) and (2.1c$_2$), fix the two free phases of the torus. They come from the necessary conditions to minimize the change between $\mathbf{u}(0;\,\cdot\,)$ and $\tilde{\mathbf{u}}(0;\,\cdot\,)$ under an appropriate norm. The second two constraints select the particular torus from within the family. Energy constraint (2.1d$_1$) fixes the Hamiltonian value at $\tilde{H}$. Pseudo-arclength constraint (2.1d$_2$) sets the distance between the current and previous torus at Δs. The distance is defined as their difference projected onto an approximate tangent $\tilde{\mathbf{u}}'$ to the fixed-energy torus family. Finally, we include two additional scalar constraints,

$$T\omega_1 = 1 \tag{2.1e$_1$}$$

$$T\omega_2 = \rho, \tag{2.1e$_2$}$$

which allows us to use both (T,ρ) and (ω_1,ω_2) as consistent parameters. This completes the system of equations for the autonomous case boundary value problem.

To determine the complete representation of torus, we need to determine function $\mathbf{u}$ along with the associated parameters. The boundary value problem (2.1) includes 6 scalar equations and depends on 6 free parameters $(T,\rho,\omega_1,\omega_2,\lambda_1,\lambda_2)$. The last two "internal" parameters, which appear in the vector field $\mathbf{f}(\ldots;\lambda_1,\lambda_2)$, are included so that there are an equal number of parameters as constraints, which is convenient for the numerical computation of a solution. Since these parameters are not in the original vector field $\mathbf{f}_0$ (1.1), they will be introduced in Section (2.2).

While the domain of $\mathbf{u} : [0,1]\times\mathbb{T}^1 \to \mathbb{R}^n$ has the structure of a cylinder, condition (2.1b) identifies its ends, $\mathbf{u}(0;\mathbb{T}^1) \equiv \mathbf{u}(1;\mathbb{T}^1)$, making it a torus. On the other hand, the torus function $\mathbf{v} : \mathbb{T}^2 \to \mathbb{R}^n$ directly parameterizes the states in terms of a pair of angles. The functions are related

by

$$\mathbf{v}(\theta_1, \theta_2) \equiv \mathbf{u}(\tau; \theta_2 - \rho\tau) \text{ where } \tau = \theta_1 \pmod 1. \tag{2.2}$$

From inspection, we can see that $\mathbf{v}$ is periodic in each of its arguments.

2.1.2 BVP for periodically-forced case

Now let us consider the case where one of the two angles, θ_1 or θ_2, appears explicitly in the equations of motion. While in the autonomous case the tori have two free frequencies (ω_1, ω_2), in the periodically-forced case one of the frequencies (or an integer multiple of it) is equal to the fixed forcing frequency. We thus have a one-parameter family of two-dimensional tori. From an alternate perspective, in an autonomous Hamiltonian system (with no additional integrals of motion) we have a one-parameter family of one-dimensional tori (periodic orbits). When a periodic perturbation is added, these periodic orbits generally become quasi-periodic orbits on two-dimensional tori [Jorba & Villanueva, 1997b].

Since the Hamiltonian is no longer a conserved quantity and the tori belong to a one-parameter (rather than two-parameter) family, we remove the constraint $(2.1\mathrm{d}_1)$ from the boundary value problem. Furthermore, if θ_1 appears explicitly in the equations of motion, we remove the corresponding phase constraint $(2.1\mathrm{c}_1)$; if θ_2 appears explicitly, we remove $(2.1\mathrm{c}_2)$. Thus, we are left with 4 scalar-valued constraints: $(2.1\mathrm{c}_1)$ or $(2.1\mathrm{c}_2)$, $(2.1\mathrm{d}_2)$, $(2.1\mathrm{e}_1)$, $(2.1\mathrm{e}_2)$.

We now consider the set of free parameters. The frequency associated with the angle that appears explicitly is fixed by the forcing. Therefore, we can remove it from the set of free parameters used in the autonomous case. Since we desire 4 parameters to match the 4 scalar constraints, we only require a single internal parameter λ_1 or λ_2 (the subscript will be selected to correspond to the index of the free angle). The resulting vector field is $\mathbf{f}(\ldots; \lambda_1)$ or $\mathbf{f}(\ldots; \lambda_2)$ with corresponding free parameters $(T, \rho, \omega_1, \lambda_1)$ or $(T, \rho, \omega_2, \lambda_2)$, respectively.

2.1.3 BVP for quasi-periodically forced case

Let us consider the case where both angles θ_1 and θ_2 appear explicitly in the equations of motion. In this situation, a two-dimensional torus is generically isolated assuming both frequencies are fixed by the quasi-periodic forcing and there are no free external parameters. From an alternate perspective, equilibrium points in autonomous Hamiltonian systems are generically isolated. When we add quasi-periodic forcing with two frequencies, this isolated point generally becomes an isolated two-dimensional torus [Jorba & Villanueva, 1997b].

Starting from the boundary value problem formulation (2.1) for the autonomous case, we can remove both continuation constraints, ($2.1\mathrm{d}_1$) and ($2.1\mathrm{d}_2$), since the tori are now isolated (we are no longer computing a family). In addition, we no longer need either phase constraint, ($2.1\mathrm{c}_1$) and ($2.1\mathrm{c}_2$). This leaves us with 2 scalar equations, ($2.1\mathrm{e}_1$) and ($2.1\mathrm{e}_2$), that simply relate (ω_1, ω_2) with (T, ρ).

Since both frequencies are fixed by the forcing, we can remove (ω_1, ω_2) from the parameter list. We also remove both internal parameters (λ_1, λ_2) leaving 2 free parameters (T, ρ) to match the 2 scalar constraints. In fact, we can directly solve for (T, ρ) from (ω_1, ω_2), so the situation is simple enough to remove both the scalar equations and the parameters. Thus, the boundary value problem reduces to only the vector field equation (2.1a) and the quasi-periodicity condition (2.1b) that can be solved for the isolated torus. Alternatively, if there is some external parameter, we can include it as a free parameter along with a stepping constraint. Since this situation is the simplest and behaves identically to the dissipative case, we do not currently consider it further.

2.1.4 Solution initialization

Quasi-periodic solution families can arise in Hamiltonian systems in many different settings. We can consider tori emanating from equilibrium points or periodic orbits, or start from an approximate torus obtained from an analytic or semi-analytic method. For a periodically-forced system (e.g., the ER3BP) that is a perturbation for an autonomous one, it is often sufficient to directly use a periodic orbit of the autonomous system (e.g., the CR3BP) as an initial guess. One frequency will

correspond to the orbit's period, and the other frequency will correspond to the forcing.

Initializing a two-dimensional torus family in an autonomous system can be more challenging. An equilibrium point or periodic orbit is a degenerate solution to the boundary value problem (2.1). The linearization about an equilibrium point with two non-resonant center components provides an initial guess for a two-dimensional torus of the nonlinear system. The same is true for a periodic orbit with a center component. Since this is a common starting point, we consider it now in more detail.

For a complex eigenvalue $e^{i(2\pi\rho)}$ of the monodromy matrix $\mathbf{\Phi}(1)$ (the state transition matrix after one period T) on the unit circle, let $\mathbf{y} \in \mathbb{C}^n$ be the corresponding eigenvector. Then the standard approach is to obtain a linear approximation of an initial invariant circle relative to the initial point on the periodic orbit:

$$\hat{\mathbf{u}}_2(0;\theta_2) = \mathrm{Re}\left[e^{i(2\pi\theta_2)}\mathbf{y}\right] = \cos(2\pi\theta_2)\,\mathrm{Re}\,[\mathbf{y}] - \sin(2\pi\theta_2)\,\mathrm{Im}\,[\mathbf{y}]\,, \tag{2.3}$$

which can be scaled by a small value for initializing the first torus. The corresponding rotation number is ρ. Note that we have freedom in selecting ρ by an integer shift. This approach can be generalized to yield initial approximations of higher-dimensional tori from periodic orbits whose monodromy matrix has more than one pair of complex conjugate eigenvalues. The state transition matrix can be used to map the initial invariant circle around the periodic orbit:

$$\hat{\mathbf{u}}_2(\tau;\theta_2) = \mathbf{\Phi}(\tau)\hat{\mathbf{u}}_2(0;\theta_2). \tag{2.4}$$

Now recall that there is a two-parameter family of invariant tori in an autonomous system, so we expect an additional tangent direction. The other tangent comes from the family tangent to the periodic orbits themselves. A simple approximation, for example, is

$$\hat{\mathbf{u}}_1(\tau) = \mathbf{u}_{\mathrm{po}}(\tau) - \tilde{\mathbf{u}}_{\mathrm{po}}(\tau) \tag{2.5}$$

where $\mathbf{u}_{\mathrm{po}}, \tilde{\mathbf{u}}_{\mathrm{po}} : \mathbb{T}^1 \to \mathbb{R}^n$ are parameterizations of two nearby periodic orbits. Combining the tangents gives us a linear approximation of the two-parameter family of tori in the vicinity of the periodic orbit,

$$\mathbf{u}(\tau;\theta_2) = \mathbf{u}_{\mathrm{po}}(\tau) + \epsilon_1\hat{\mathbf{u}}_1(\tau) + \epsilon_2\hat{\mathbf{u}}_2(\tau;\theta_2) \tag{2.6}$$

where $(\epsilon_1, \epsilon_2) \in \mathbb{R}^n$ are small parameters. Since we reduce the family to a single parameter using a constraint such as $(2.1\mathrm{d}_1)$ that fixes the Hamiltonian value, the parameters (ϵ_1, ϵ_2) are not independent. In practice, however, it suffices to have a nonzero component in the direction of the true family tangent. When tori at a fixed Hamiltonian level are computed, only including the $\hat{\mathbf{u}}_2$ component (i.e., $\epsilon_1 = 0$) is typically a good choice.

2.1.5 Lack of parameters

The family structure we have discussed pertains to having all external parameters fixed. Therefore, we do not have explicit parameters λ_1 or λ_2 in our original vector field $\mathbf{f}_0$, and we have a seemingly overconstrained system of equations. This is a characteristic of Hamiltonian systems that is not present in a generic (dissipative) dynamical system. In that case, these parameters are external and can be varied to compute families of solutions.

There are not obvious redundant equations to remove. Removing any of the scalar constraint equations will result in a system that does not have a unique solution. One approach is to, after discretization, use a pseudo-inverse as in a Gauss–Newton method. We would, however, like to use the framework of a typical collocation-based boundary-value solver and continuation method. Rather than attempt to remove two equations, what we do is introduce two additional parameters. Ultimately, we seek a well-posed system with an equal number of equations and unknowns. This allows us to use a standard Newton method for solving the discretized equations.

2.2 UNFOLDING PARAMETERS

We now introduce unfolding parameters that embed the Hamiltonian system in a family of generic dynamical systems. These additional parameters allow us to construct a well-posed quasi-periodic boundary value problem of the form described in Section 2.1.1 for autonomous systems and in Section 2.1.2 for periodically-forced systems. While the quasi-periodic solutions of the original Hamiltonian system remain, we will demonstrate that any additional solutions that emerge correspond to systems that are exponentially close to the original.

A similar situation is encountered when computing periodic orbits (one-dimensional invariant tori) in autonomous Hamiltonian systems. Without any free external parameters, these solutions lie in k-parameter families (where $k \geq 1$ is the number of independent integrals of motion), which is a non-generic behavior. For the case of a single integral of motion, Sepulchre & MacKay [1997] add an unfolding parameter λ by augmenting the vector field with the gradient of the Hamiltonian,

$$\mathbf{f}(\mathbf{x}) := \mathbf{f}_0(\mathbf{x}) + \lambda \frac{\partial H}{\partial \mathbf{x}}^{\mathsf{T}}(\mathbf{x}). \tag{2.7}$$

It is demonstrated that periodic solutions only exist when $\lambda = 0$. Additional parameters can be added if the system admits additional integrals of motion [Muñoz-Almaraz et al., 2003]. Doedel et al. [2003] use augmented systems of this form for computing families of periodic orbits in conservative systems. Each orbit family is a "vertical branch" along which the parameter is always zero.

The challenge is that we need two unfolding parameters (λ_1, λ_2) for computing two-dimensional quasi-periodic tori in autonomous systems with only a single integral of motion, the Hamiltonian. We need one unfolding parameter in periodically-forced systems when there are no integrals of motion; the Hamiltonian is no longer conserved. Instead of (global) integrals of motion, we will use the torus actions, which behave like local integrals of motion. We will demonstrate that the gradient of each action can easily be obtained from the torus representation $(\mathbf{u}, T, \rho)$ via the canonical coordinates $(\mathbf{q}, \mathbf{p})$.

2.2.1 Action–angle coordinates

To make the procedure more flexible, we do not assume that the coordinate set $\mathbf{x} \in \mathbb{R}^n$, where n is even, is canonical. Let us assume, however, that a transformation $\mathbf{y}(\mathbf{x}) := (\mathbf{q}, \mathbf{p})(\mathbf{x}) \in \mathbb{R}^{\bar{n}} \times \mathbb{R}^{\bar{n}}$, where $\bar{n} := n/2$, is known such that the new coordinates are canonical. For example, if the original coordinate set comes from the Lagrangian formulation of the equations of motion, the generalized momenta are $\mathbf{p} := \partial L / \partial \dot{\mathbf{q}}^{\mathsf{T}}$ where $L(\mathbf{q}, \dot{\mathbf{q}}, \boldsymbol{\theta})$ is the Lagrangian.

We now restrict ourselves to the autonomous setting. In the new coordinates the Hamiltonian is $\bar{H}(\mathbf{q}, \mathbf{p})$. The system has $\bar{n} \geq 2$ degrees of freedom. A two-dimensional torus is maximal if $\bar{n} = 2$. If $\bar{n} \geq 3$, there is behavior normal to the family of two-dimensional tori that can (nondegenerately)

be fully elliptic, fully hyperbolic, or some combination of the two. If there is elliptic normal behavior, the two-dimensional torus family can be embedded in a family of higher-dimensional tori.

We begin by assuming that the system admits a quasi-periodic torus with frequencies $\boldsymbol{\omega}^0 \equiv (\omega_1^0, \omega_2^0)$ such that there exists a local canonical change of coordinates $(\mathbf{q}, \mathbf{p}) \mapsto (\boldsymbol{\theta}, \mathbf{I}, \mathbf{Q}, \mathbf{P})$ putting the Hamiltonian in the normal form (plus remainder)

$$K(\boldsymbol{\theta}, \mathbf{I}, \mathbf{Q}, \mathbf{P}) = \left\langle \boldsymbol{\omega}^0, \mathbf{I} \right\rangle + K_2(\mathbf{I}, \mathbf{Q}, \mathbf{P}) + R(\boldsymbol{\theta}, \mathbf{I}, \mathbf{Q}, \mathbf{P}). \tag{2.8}$$

Here $\boldsymbol{\theta} \equiv (\theta_1, \theta_2) \in \mathbb{T}^2$ and $\mathbf{Q} \in \mathbb{R}^{\bar{n}-2}$ are the generalized positions, and $\mathbf{I} \equiv (I_2, I_2) \in \mathbb{R}^2$ and $\mathbf{P} \in \mathbb{R}^{\bar{n}-2}$ are the generalized momenta. The variables $\mathbf{Q}$ and $\mathbf{P}$ are coordinates normal to the two-dimensional torus family (for maximal tori, these coordinates can be removed). Let the initial torus correspond to coordinates $\mathbf{I} = \mathbf{0}$ and $(\mathbf{Q}, \mathbf{P}) = \mathbf{0}$, and let K_2 only contain terms of degree at least two in these variables. Additional terms are included in the remainder R, which also depends on the angles.

The form (2.8) is motivated by the KAM results of Jorba & Villanueva [1997a], which are applicable to both lower-dimensional and maximal tori. Subject to reducibility, nonresonance, and nondegeneracy conditions, an infinite sequence of canonical transforms can (formally) remove all terms from the remainder. In a finite number of steps, a canonical transform from $(\mathbf{q}, \mathbf{p})$ can be constructed such that in a neighborhood of the initial torus, the remainder R is exponentially small relative to the neighborhood's size.

Applying Hamilton's equations to (2.8), we can deduce the following behavior of the torus actions:

$$\dot{\mathbf{I}} = -\frac{\partial K}{\partial \boldsymbol{\theta}}^{\intercal} = -\frac{\partial R}{\partial \boldsymbol{\theta}}^{\intercal}, \tag{2.9}$$

which is also exponentially small. In fact, the remainder does not prevent the existence of most tori [Jorba & Villanueva, 1997a]. For a Cantor set (whose complement has exponentially-small measure), there is a family of tori in the neighborhood of the initial torus that are parameterized by their constant actions $\mathbf{I}$. The variation of the corresponding angles is

$$\dot{\boldsymbol{\theta}} = +\frac{\partial K}{\partial \mathbf{I}}^{\intercal} = \boldsymbol{\omega}^0 + \frac{\partial K_2}{\partial \mathbf{I}}^{\intercal} + \frac{\partial R}{\partial \mathbf{I}}^{\intercal}. \tag{2.10}$$

On the nearby tori, the angles will change at constant rates, $\dot{\boldsymbol{\theta}} = \boldsymbol{\omega}$, and excluding degenerate situations, the frequency vector $\boldsymbol{\omega}$ can also be used to parameterize the family.

Action–angle coordinates provide a geometric perspective on the dynamics in the vicinity of a torus. While they always exist, the transformation from the original system is, in general, not easily obtainable. In the approach we present, we will avoid explicitly computing the transformation itself but rather take advantage of its canonical nature.

2.2.2 Unfolding for autonomous case

Inspired by the choice for computing periodic orbits in systems with multiple integrals of motion [Muñoz-Almaraz et al., 2003], we propose the following augmented vector field for computing two-dimensional quasi-periodic tori in autonomous Hamiltonian systems:

$$\mathbf{f}(\mathbf{x}; \lambda_1, \lambda_2) := \mathbf{f}_0(\mathbf{x}) + \lambda_1 \frac{\partial I_1{}^{\intercal}}{\partial \mathbf{x}}(\mathbf{x}) + \lambda_2 \frac{\partial I_2{}^{\intercal}}{\partial \mathbf{x}}(\mathbf{x}). \tag{2.11}$$

We intend to demonstrate that the addition of the parameters does not affect the quasi-periodic solution structure. In particular, for nonzero (or not exponentially small) parameter values, the tori are destroyed. We will also address how the terms $\partial I_i/\partial \mathbf{x}$ are computed. We start from the following proposition:

Proposition 1. *Consider a quasi-periodic solution of an autonomous Hamiltonian system with vector field* $\dot{\mathbf{x}} = \mathbf{f}(\mathbf{x}; 0, 0)$. *When this solution is expressed in a canonical coordinate set* $\mathbf{y}(\mathbf{x})$*, assume that a canonical transformation* $\mathbf{z}(\mathbf{y})$ *exists putting a neighborhood of the solution into normal form (2.8) with an exponentially small remainder. Then any nearby quasi-periodic solution of the augmented vector field,* $\dot{\mathbf{x}} = \mathbf{f}(\mathbf{x}; \lambda_1, \lambda_2)$*, will have exponentially small unfolding parameters.*

Proof. We begin by generalizing the approach of Lemma 6 of Muñoz-Almaraz et al. [2003] to quasi-periodic solutions. Let $(\mathbf{u}, T, \rho; \lambda_1, \lambda_2)$ be a quasi-periodic solution in the neighborhood of the original solution, and let $I := \lambda_1 I_1 + \lambda_2 I_2$, a linear combination of the actions. Note this allows us to write the augmented vector field as $\mathbf{f} = \mathbf{f}_0 + \partial I/\partial \mathbf{x}^{\intercal}$. Recalling $\mathbf{u}(0; \theta_2) = \mathbf{u}(1; \theta_2 - \rho)$ for all

$\theta_2 \in \mathbb{T}^1$, we can take the following steps:

$$\begin{aligned} 0 &= \int_0^1 I(\mathbf{u}(1;\theta_2))\, d\theta_2 - \int_0^1 I(\mathbf{u}(0;\theta_2))\, d\theta_2 \\ &= \int_0^1 \int_0^1 \frac{dI}{d\tau}(\mathbf{u}(\tau;\theta_2))\, d\tau\, d\theta_2 \\ &= \int_0^1 \int_0^1 \left(\frac{\partial I}{\partial \mathbf{x}} \cdot T \left(\mathbf{f}_0 + \frac{\partial I}{\partial \mathbf{x}}^{\intercal} \right) \right) \circ \mathbf{u}(\tau;\theta_2)\, d\tau\, d\theta_2, \end{aligned} \tag{2.12}$$

where '$\circ$' denotes the composition of functions. Since we evaluate over all the states on the torus, we can switch from $\mathbf{u} : [0,1] \times \mathbb{T}^1 \to \mathbb{R}^n$ to the corresponding torus function $\mathbf{v} : \mathbb{T}^2 \to \mathbb{R}^n$,

$$\int_{\mathbb{T}^2} \left\| \frac{\partial I}{\partial \mathbf{x}}^{\intercal} \right\|^2 \circ \mathbf{v}(\boldsymbol{\theta})\, d\boldsymbol{\theta} = - \int_{\mathbb{T}^2} \left(\frac{\partial I}{\partial \mathbf{z}} \cdot \mathbf{g}_0 \right) \circ \mathbf{z}(\mathbf{y}(\mathbf{v}(\boldsymbol{\theta})))\, d\boldsymbol{\theta} \tag{2.13}$$

where the nominal vector field $\mathbf{f}_0(\mathbf{x}) = \partial \mathbf{x}/\partial \mathbf{z} \cdot \mathbf{g}_0(\mathbf{z}(\mathbf{y}(\mathbf{x}))$ is expressed in action–angle coordinates, $\mathbf{g}_0(\mathbf{z})$. Inserting the behavior of the actions from (2.9), we have

$$\int_{\mathbb{T}^2} \left\| \lambda_1 \frac{\partial I_1}{\partial \mathbf{x}}^{\intercal} + \lambda_2 \frac{\partial I_2}{\partial \mathbf{x}}^{\intercal} \right\|^2 \circ \mathbf{v}(\boldsymbol{\theta})\, d\boldsymbol{\theta} = \int_{\mathbb{T}^2} \left(\lambda_1 \frac{\partial R}{\partial \theta_1} + \lambda_2 \frac{\partial R}{\partial \theta_2} \right) \circ \mathbf{z}(\mathbf{y}(\mathbf{v}(\boldsymbol{\theta})))\, d\boldsymbol{\theta}. \tag{2.14}$$

Given that $\partial I_1/\partial \mathbf{x}$ and $\partial I_2/\partial \mathbf{x}$ are linearly independent over the surface of the torus, we can conclude $\|\boldsymbol{\lambda}\|$ is exponentially small like the remainder. □

Let us remark that the local nature of the actions and Cantor-like nature of the quasi-periodic solutions make it difficult to make a statement as strong as for periodic orbits. It may be possible to strengthen this statement using KAM techniques, but that is beyond the scope of this document. However, we will see that augmenting the vector field in this manner for a periodic orbit allows us to recover the standard form from (2.7) (we will see this in (2.21)).

For the computational purposes of this document, this result is sufficient. Note that if we assume that the manifold is completely filled with tori, then the remainder is identically zero and we find that the parameters are identically zero from (2.14). Since the solution can be checked a posteriori and since we have error control algorithms, we take the approach that the assumptions do not need to be verified ahead of time but rather we can assess the accuracy of a solution when it is found. In practice, it appears to work well.

Since the transformation to action–angle coordinates is canonical, we use the direct conditions (necessary and sufficient) for a canonical transformation [Goldstein et al., 2002]:

$$\frac{\partial I_i}{\partial \mathbf{y}}^{\mathsf{T}} = -\mathbf{J}\frac{\partial \mathbf{y}}{\partial \theta_i} \tag{2.15}$$

where $\mathbf{y} := (\mathbf{q}, \mathbf{p})$ is written in canonical coordinates and where $\mathbf{J}$ is the $n \times n$ canonical structure matrix,

$$\mathbf{J} := \begin{bmatrix} 0 & +\mathrm{Id} \\ -\mathrm{Id} & 0 \end{bmatrix}. \tag{2.16}$$

In fact, this is quite practical since the torus can be parameterized in terms of angles: $\mathbf{v} : \mathbb{T}^2 \to \mathbb{R}^n$. Since our original coordinates are not necessarily canonical, we compute the gradient of the actions on the torus as:

$$\frac{\partial I_i}{\partial \mathbf{x}}^{\mathsf{T}} = -\frac{\partial \mathbf{y}}{\partial \mathbf{x}}^{\mathsf{T}} \mathbf{J} \frac{\partial \mathbf{y}}{\partial \mathbf{x}} \frac{\partial \mathbf{v}}{\partial \theta_i} \tag{2.17}$$

Recall that the boundary value problem (2.1) is setup in terms of a "cylinder function" $\mathbf{u}$ consisting of a collection of trajectories parameterized by angle θ_2. Since $\partial \mathbf{u}/\partial\theta_2 = \partial \mathbf{v}/\partial\theta_2$, the gradient of I_2 over the torus is

$$\frac{\partial I_2}{\partial \mathbf{x}}^{\mathsf{T}}(\mathbf{u})\bigg|_{(\tau,\theta_2)} = -\left(\frac{\partial \mathbf{y}}{\partial \mathbf{x}}^{\mathsf{T}} \mathbf{J} \frac{\partial \mathbf{y}}{\partial \mathbf{x}}\right) \frac{\partial \mathbf{u}}{\partial \theta_2}\bigg|_{(\tau,\theta_2)}. \tag{2.18}$$

The other variable parameterizing the solution is "time" τ rather than angle θ_1. We can, however, compute the derivative with respect to θ_1 from the derivative with respect to angle θ_2 and the vector field using the invariance relation (1.2), which gives us

$$\frac{\partial I_1}{\partial \mathbf{x}}^{\mathsf{T}}(\mathbf{u}; T, \rho)\bigg|_{(\tau,\theta_2)} = -\left(\frac{\partial \mathbf{y}}{\partial \mathbf{x}}^{\mathsf{T}} \mathbf{J} \frac{\partial \mathbf{y}}{\partial \mathbf{x}}\right) \left(T\mathbf{f}_0(\mathbf{u}, \boldsymbol{\theta}) - \rho \frac{\partial \mathbf{u}}{\partial \theta_2}\right)\bigg|_{(\tau,\theta_2)}. \tag{2.19}$$

Note that $d\mathbf{u}/d\tau$ could be used in place of $T\mathbf{f}_0(\mathbf{u})$.

An alternative to using action I_1 is to use the Hamiltonian. Locally we have two independent (approximate) integrals of motion, the actions. Since the Hamiltonian is an integral of motion, it can be used to replace either action in (2.11) and the result would still be valid. Therefore, an alternative choice of the augmented vector field is

$$\mathbf{f}(\mathbf{x}; \lambda_1, \lambda_2) := \mathbf{f}_0(\mathbf{x}) + \lambda_1 \frac{\partial H}{\partial \mathbf{x}}^{\mathsf{T}}(\mathbf{x}) + \lambda_2 \frac{\partial I_2}{\partial \mathbf{x}}^{\mathsf{T}}(\mathbf{x}) \tag{2.20}$$

This can be shown in same way as Proposition 1, except because it is an exact integral of motion, we no longer have the $\partial R/\partial\theta_1$ term that appears in the proof.

As a brief aside, let us now consider the case of a periodic orbit. If we use the gradient of the action I_{po} of the one-dimensional torus, we find

$$\begin{aligned}\frac{\partial I_{\text{po}}}{\partial \mathbf{x}}^{\intercal} &= -\frac{1}{T}\frac{\partial \mathbf{y}}{\partial \mathbf{x}}^{\intercal}\mathbf{J}\frac{\partial \mathbf{y}}{\partial \mathbf{x}}\frac{d\mathbf{x}}{dt} \\ &= -\frac{1}{T}\frac{\partial \mathbf{y}}{\partial \mathbf{x}}^{\intercal}\mathbf{J}\mathbf{J}\frac{\partial \mathbf{x}}{\partial \mathbf{y}}^{\intercal}\frac{\partial H}{\partial \mathbf{x}}^{\intercal} \\ &= \frac{1}{T}\frac{\partial H}{\partial \mathbf{x}}^{\intercal}\end{aligned} \tag{2.21}$$

We recover the form of the augmented term in (2.7) up to a scaling by the period T.

2.2.3 Unfolding for periodically-forced case

A Hamiltonian system with forcing can be recast as an autonomous Hamiltonian system by adding a pair of variables for each (nonresonant) angle that appears explicitly in the original Hamiltonian. This allows us to apply the autonomous results from Section 2.2.2 to the periodically-forced case. In this section, we explain how the results can be moved back to the original coordinate set.

For convenience, let us consider the Hamiltonian in terms of canonical coordinates. We can define an extended Hamiltonian of the form

$$\tilde{H}(\mathbf{q},\mathbf{p},\phi,p_\phi) := \bar{H}(\mathbf{q},\mathbf{p};\phi) + \bar{\omega}p_\phi \tag{2.22}$$

where ϕ and $p_\phi$are the extended generalized position and momentum, respectively. In this form we can apply Proposition 1, and deduce that the unfolding parameters will be exponentially small. While we can simply leave the system in this form, and proceed as in the autonomous case, we prefer to use a smaller coordinate set for computations and remove "equivalent" solutions.

From Hamilton's equations, we have the following behaviors of the extended coordinates:

$$\dot{\phi} = +\bar{\omega} \tag{2.23a}$$

$$\dot{p}_\phi = -\frac{\partial \bar{H}}{\partial \phi}. \tag{2.23b}$$

The extended momentum p_ϕ does not appear in anywhere else in the vector field. For any quasi-periodic solution, a constant value can be added to the p_ϕ coordinate and an equivalent solution is obtained. For simplicity let us assume that the solution is parameterized such that $\theta_2 = \phi$. Then the shift in p_ϕ corresponds to the action I_2, so we remove the coordinate p_ϕ and remove the corresponding unfolding term in (2.11) with associated parameter λ_2. This effectively fixes I_2 and reduces the two-parameter family of tori to a single parameter. The only remaining extended coordinate is ϕ. In the augmented vector field, this coordinate has equation of motion $\dot{\phi} = \bar{\omega} + \lambda_1 \frac{\partial I_1}{\partial \phi}$. However, since $\frac{\partial I_1}{\partial \phi} = \frac{\partial I_1}{\partial \theta_2} = 0$, we can also remove the coordinate ϕ and replace it with θ_2 in the equations of motion, while fixing $\omega_2 = \bar{\omega}$.

Since we can apply the same reasoning for either angle appearing explicitly in the equations of motion, what we are left with is an augmented vector field

$$\mathbf{f}(\mathbf{x}, \boldsymbol{\theta}; \lambda_i) := \mathbf{f}_0(\mathbf{x}, \boldsymbol{\theta}) + \lambda_i \frac{\partial I_i}{\partial \mathbf{x}}^\intercal \tag{2.24}$$

where $\mathbf{x}$ is the non-extended coordinate set and subscript i corresponds to the angle θ_i that does not appear explicitly. The computation of the gradient is identical to the autonomous case using (2.18) or (2.19). We now have a vector field that can be put into the boundary value problem of Section 2.1.2 that depends on the expected number of parameters for a generic dynamical system.

2.3 COMPUTATION OF TORI

In order to compute the cylinder function $\mathbf{u} : [0, 1] \times \mathbb{T}^1 \to \mathbb{R}^n$ corresponding to a two-dimensional quasi-periodic torus, we discretize it in two steps. First, we discretize the second argument by restricting the angle to a set of evenly-spaced values. This is functionally equivalent to using a truncated Fourier series. Then, we have a set of trajectories on the torus surface that are discretized via continuous piecewise polynomials with the vector field enforced at the Gauss–Legendre collocation points. Using a Newton method, the discretized boundary value problem is solved. The Jacobian's sparsity is an important consideration for the implementation. An error estimate of the torus invariance is also provided. In addition, a trajectory on the torus can be efficiently generated using trigonometric interpolation.

Note that while the discretized torus depends on a finite number of variables, we have a continuous parameterization of its entire surface. Therefore, we can view the Newton method as reshaping the torus to match the vector field. If a shooting method was used instead of a collocation method, each iteration would exactly match the vector field, but the solution would not be a torus until convergence.

2.3.1 Fourier discretization

We discretize the cylinder function $\mathbf{u}(\tau;\theta_2)$ beginning with its second argument θ_2. From one perspective, the cylinder function corresponds to a set of trajectories $\mathbf{u}(\,\cdot\,;\theta_2) : [0,1] \to \mathbb{R}^n$ parameterized by the angle $\theta_2 \in \mathbb{T}^1$. From an alternative perspective, the cylinder function represents a set of circle functions $\mathbf{u}(\tau;\,\cdot\,) : \mathbb{T}^1 \to \mathbb{R}^n$ at different normalized times $\tau \in [0,1]$ along the flow. Since we perform operations on angle θ_2 within the augmented vector field, we start from this latter perspective.

The natural choice for representing each circle function $\mathbf{u}(\tau;\,\cdot\,)$ is via a Fourier series truncated at a certain order M_2,

$$\mathbf{u}(\tau;\theta_2) = \sum_{|k|\le M_2} \mathbf{c}_k(\tau) e^{ik(2\pi\theta_2)} \tag{2.25}$$

where index $k \in \mathbb{Z}$ and coefficients $\mathbf{c}_k(\tau) \in \mathbb{C}^n$. For computation, however, it is easier to work with states rather than Fourier coefficients. There is a direct relationship between the set of $N_2 := 2M_2+1$ coefficients $\{\mathbf{c}_k(\tau)\}$ and the set of N_2 states $\{\mathbf{u}(\tau;k/N_2)\}$. This is possible via the discrete Fourier transform (DFT), which is a linear and invertible operation.

The discretized circle function at time τ can thus be completely represented by the set of states at N_2 evenly-spaced angle values,

$$\mathbf{X}(\tau) := \left\{ \mathbf{X}^k(\tau) := \mathbf{u}(\tau;\tfrac{k}{N_2}) \;\middle|\; k = 0,\ldots,N_2-1 \right\} \tag{2.26}$$

recalling that we nominally parameterize angle θ_2 over the unit interval $[0,1)$. The collected state $\mathbf{X}(\tau)$ belongs to $\mathbb{R}^{n^*}$ where $n^* := nN_2$. We also define the collected vector field acting on the collected state:

$$\mathbf{F}(\mathbf{X}(\tau),\tau;\rho,\lambda_1,\lambda_2) := \left\{ \mathbf{f}(\mathbf{X}^k(\tau),(\tau,\tfrac{k}{N_2}+\rho\tau);\lambda_1,\lambda_2) \;\middle|\; k = 0,\ldots,N_2-1 \right\}. \tag{2.27}$$

This allows us to write the equation of motion (2.1a) for the boundary value problem as simply

$$\frac{d\mathbf{X}}{d\tau}(\tau) = T\mathbf{F}(\mathbf{X}(\tau), \tau; \rho, \lambda_1, \lambda_2) \tag{2.28}$$

for all $\tau \in [0, 1]$. The quasi-periodic boundary condition (2.1b) can also be expressed in terms of the collected state:

$$\mathbf{X}(0) = \mathbf{R}(-\rho)\mathbf{X}(1). \tag{2.29}$$

Here the real $n^* \times n^*$ rotation matrix $\mathbf{R}(-\rho)$ can be constructed by the composition of the DFT matrix, the phase shift $-\rho$, and the inverse DFT matrix. The derivative with respect to angle θ_2 is also a linear operation. Finally, the boundary value problem (2.1) also contains integrals over the angle θ_2. After the Fourier discretization, this is just the average over the collected states. For example, the constraint ($2.1\mathrm{d}_1$) on the Hamiltonian becomes

$$\frac{1}{N_2} \sum_{i=0}^{N_2-1} H(\mathbf{X}^i(0)) = \tilde{H}. \tag{2.30}$$

The torus computation is now posed in a form typical for boundary value problem solution techniques. The form is similar to that of periodic orbits except we are now dealing with collected states $\mathbf{X}(\tau) \in \mathbb{R}^{nN_2}$ rather than the individual states $\mathbf{x}(\tau) \in \mathbb{R}^n$. Let us emphasize that the computation variables are the state variables rather than Fourier coefficients.

2.3.2 Gauss–Legendre collocation

We now present a collocation-based approach for finding a trajectory $\mathbf{X}(\cdot) : [0, 1] \to \mathbb{R}^{n^*}$ that matches the flow generated by vector field $\mathbf{F}$. In the current setting, $\mathbf{X}(\cdot)$ represents the cylinder function after the Fourier discretization. In later chapters, $\mathbf{X}(\cdot)$ will represent a single trajectory (in which case, we use the original vector field, $\mathbf{F} = \mathbf{f}_0$ and $n^* = n$), for example, a heteroclinic connection between two tori. We can proceed in the same manner for either situation.

To numerically compute the trajectory $\mathbf{X}(\cdot)$, we represent it as a continuous piecewise polynomial of degree-m with $(N + 1)$ break points $0 = \tau_{0,0} < \tau_{1,0} < \ldots < \tau_{N,0} = 1$. Within each of the N intervals, we take the m roots of of the degree-m Legendre polynomial, $\hat{\tau}_1, \ldots, \hat{\tau}_m \in (-1, +1)$, and rescale them to the interval $(\tau_{i,0}, \tau_{i+1,0}) \ni \tau_{i,1}, \ldots, \tau_{i,m}$. Note that all the roots are in the

interior of the interval. Then we can uniquely represent $\mathbf{X}(\cdot)$ on each interval by the set of states $\{\mathbf{X}_{i,0}, \mathbf{X}_{i,1}, \ldots, \mathbf{X}_{i,m}\}$ at the times $\{\tau_{i,0}, \tau_{i,1}, \ldots, \tau_{i,m}\}$. For $\tau \in [\tau_{i,0}, \tau_{i+1,0})$, this is the degree-$m$ polynomial

$$\mathbf{X}(\tau) = \sum_{k=0}^{m} \mathbf{X}_{i,k} \ell_k(\hat{\tau}) \quad \text{where} \quad \hat{\tau} = \frac{\tau - \tau_{i,0}}{\tau_{i+1,0} - \tau_{i,0}} \tag{2.31}$$

and $\ell_k(\hat{\tau})$ are the Lagrange basis polynomials,

$$\ell_k(\hat{\tau}) = \prod_{\substack{j=0 \\ j \neq k}}^{m} \frac{\hat{\tau} - \hat{\tau}_j}{\hat{\tau}_k - \hat{\tau}_j}, \tag{2.32}$$

which have the property $\ell_k(\hat{\tau}_k) = 1$, and $\ell_k(\hat{\tau}_l) = 0$ when $l \neq k$.

For a collocation method, we require the derivative of $\mathbf{X}(\cdot)$ to match the vector field $\mathbf{F}$ at a set of times. For Gauss–Legendre collocation, these times are precisely the rescaled roots of the degree-m Legendre polynomial. This corresponds to the collocation conditions

$$(\tau_{i+1,0} - \tau_{i,0}) \sum_{k=0}^{m} \mathbf{X}_{i,k} \frac{d\ell_k}{d\hat{\tau}}(\hat{\tau}_j) = \mathbf{F}(\mathbf{X}_{i,j}, \tau_{i,j}) \tag{2.33}$$

that are enforced on all the intervals ($i = 0, \ldots, N-1$) and for all the collocation times ($j = 1, \ldots, m$). Since we require that $\mathbf{X}(\cdot)$ is continuous over the entire interval $[0, 1]$, we mandate continuity between the piecewise polynomials,

$$\sum_{j=0}^{m} \mathbf{X}_{i,j} \ell_j(1) = \mathbf{X}_{i+1,0} \tag{2.34}$$

for $i = 0, \ldots, N-1$. Note that this also constrains the final state $\mathbf{X}_{N,0}$ to match the last polynomial.

Together between the collocation conditions (2.33) and continuity constraints (2.34), we have $N(m+1)$ vector equations. There are $N(m+1)+1$ vector states $\mathbf{X}_{i,j}$. Therefore, we need (at least) n^* additional scalar equations to define a trajectory. For an initial value problem, this corresponds to fixing $\mathbf{X}_{0,0}$. For a periodic orbit, this is periodicity $\mathbf{X}_{0,0} = \mathbf{X}_{N,0}$. For a quasi-periodic torus, this is the boundary condition (2.29), $\mathbf{X}_{0,0} = \mathbf{R}(-\rho)\mathbf{X}_{N,0}$.

A functionally equivalent (but computationally different) approach is to use the states corresponding to the $(m+1)$ evenly-spaced times $\{\tau_{i,0} + (\tau_{i+1,0} - \tau_{i,0})\, j/m \mid j = 0, \ldots m\}$ on each interval to define the degree-m polynomial. Since this includes both boundaries $\tau_{i,0}$ and $\tau_{i+1,0}$ of

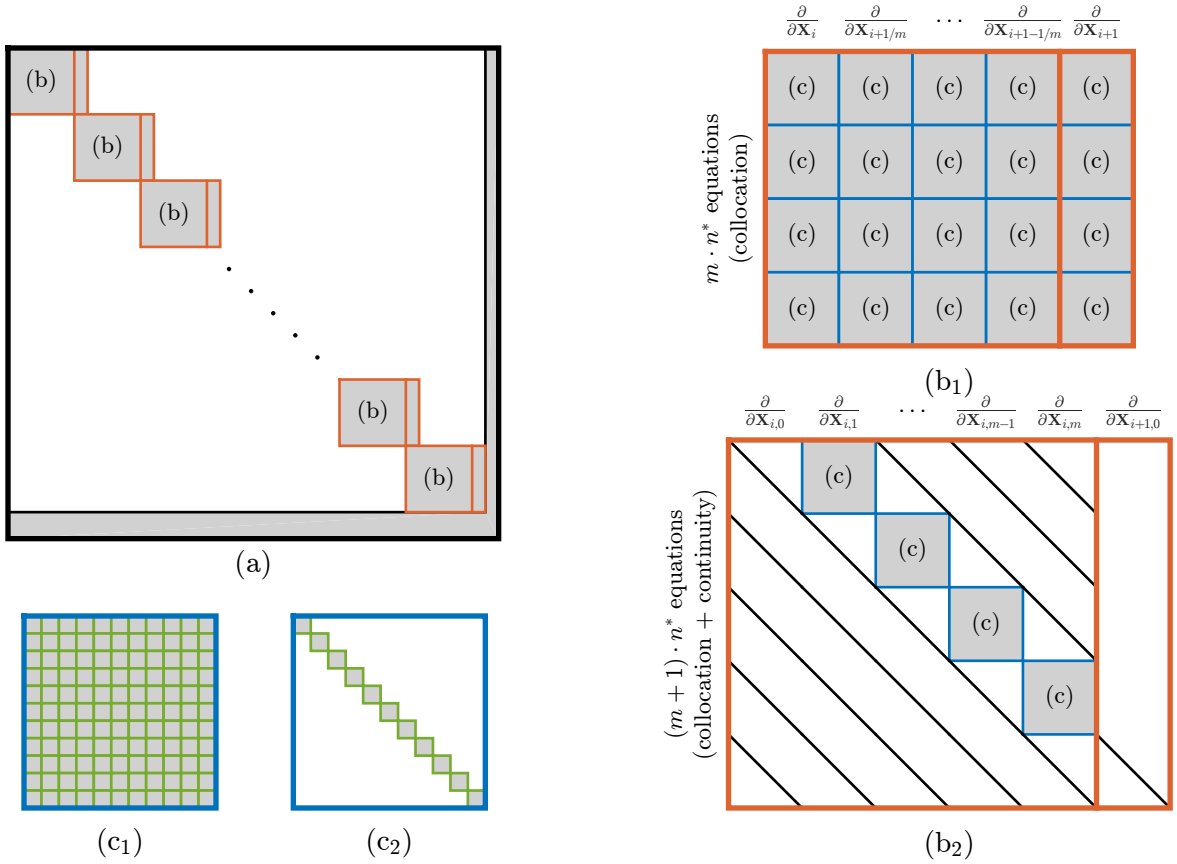

Figure 2.1: (a) Jacobian sparsity; ($b_{1,2}$) mesh block sparsity; ($c_{1,2}$) subblock sparsity. Diagonal lines represent diagonal nonzero elements. (See text for more details.)

the interval, it directly incorporates the continuity constraint into the polynomial representation. Thus, we only need Nm vector equations and $Nm + 1$ vector states (we still require n^* additional scalar equations). This is the approach used in the boundary value problem solver AUTO [Doedel et al., 1991]. The disadvantage is that the Gauss–Legendre collocation times do not match the the times used to construct the polynomial. When the boundary value problem is solved with a Newton method, this approach leads to a much denser Jacobian matrix (though with fewer rows and columns). When dealing with high-dimensional problems ($n^* \gg 1$), such as the computation of quasi-periodic tori, it is preferable to use the form (2.31), which leads to a notably sparser Jacobian matrix (though with more rows and columns).

This is illustrated in Figure 2.1 where each gray block denoted (b) corresponds to a single mesh interval. Using an AUTO-style discretization, each of these blocks are nominally full as in (b_1).

The discretization presented here leads to a sparser block as shown in (b_2). Within these blocks there are subblocks (c) corresponding to the sparsity of $\partial\mathbf{F}/\partial\mathbf{X}$. Later in Section 2.4.1, we will address how linear stability information can be extracted from the Jacobian matrix.

Gauss–Legendre collocation methods are appealing due to their error characteristics [Boor & Swartz, 1973]. For a given number m of collocation points (and for a sufficiently smooth vector field), they possess a global error $\mathcal{O}(h^{m-1})$ where h is the size of the largest mesh interval $|\tau_{i+1,0} - \tau_{i,0}|$. Furthermore, they exhibit "superconvergence" at the mesh boundaries where the states are $\mathcal{O}(h^{2(m-1)})$ accurate. By adaptively adjusting the mesh spacing and controlling the global error [Russell & Christiansen, 1978], we obtain a robust numerical method for solving the boundary value problem.

2.3.3 Predictor–corrector implementation

With an appropriate set of constraints, a dynamical system's quasi-periodic tori can be reduced to a single parameter family, each member having a unique cylinder function representation. Incorporating pseudo-arclength continuation allows us to select a single member from the family at each step. Computing each member requires solving the boundary value problem (2.1), which we approach using a predictor–corrector method. The family can be initialized using the techniques described in Section 2.1.4. Assuming a previous member $(\tilde{\mathbf{u}}, \tilde{T}, \tilde{\boldsymbol{\rho}}, \tilde{\boldsymbol{\lambda}})$ of the family is known along with an approximation of the family tangent $(\tilde{\mathbf{u}}', \tilde{T}', \tilde{\boldsymbol{\rho}}', \tilde{\boldsymbol{\lambda}}')$, we typically use a simple linear prediction of the next member.

After the prediction step, a Newton method is used to iteratively converge to the quasi-periodic torus. An essential aspect of the Fourier discretization and the piecewise polynomial representation is that each constraint only depends on a limited number of the the problem variables (the states and the parameters). This leads to a Jacobian matrix that is very sparse as shown in Figure 2.1. Each subblock (c) in block (b_1) represents the partial derivative of a collocation constraint (2.33) with respect to a collected state $\mathbf{X}_{i,j} \in \mathbb{R}^{nN_2}$. Nominally this is a full matrix as shown in (c_1) since the augmented vector field depends on $\partial\mathbf{u}/\partial\theta_2$, which is a function of the entire collected state. Recall, however, that Proposition 1 states that the parameters scaling these augmented terms are

exponentially small. We, therefore, remove terms of $\mathcal{O}(\lambda_1, \lambda_2)$ from the Jacobian, which makes each subblock of the form (c_2) which consists of N_2 full matrices of size $n \times n$ along the diagonal. This reduction allows us to further increase the sparsity significantly. Note that the partial derivatives with respect to λ_1 and λ_2 (which are in the final columns) are $\mathcal{O}(1)$ and still included in the Jacobian. Let us emphasize that the terms of $\mathcal{O}(\lambda_1, \lambda_2)$ are only removed from the Jacobian and not the discretized equations themselves. In practice, it appears that removing these small perturbations on the Jacobian does not affect the convergence at all while notably increasing the sparsity.

By adding the unfolding parameters, we are able to obtain a square Jacobian matrix. This is constructed as part of a general-purpose, collocation-based BVP solver we have implemented in MATLAB. To solve the linear system for the Newton method, we use an efficient sparse LU factorization [Davis et al., 2016]. This factorization takes the vast majority of the computation time compared to the evaluation of the vector field and other operations. Once the quasi-periodic solution is converged, the next member of the family can be predicted, and the process repeats. If we are unable to converge within tolerance in at most five iterations, a smaller step is taken. Note that all aspects of the computation are parallelizable (including the sparse matrix factorization), though this is not currently used. Alternatively, since the tori often lie in multi-parameter families, the continuation process can be parallelized. For example, we can compute families at different energy levels $\tilde{H}$ separately.

2.3.4 Error control

Recall that the cylinder function $\mathbf{u}$ is discretized in two steps. First, the Fourier discretization reduces it to a set of N_2 trajectories on the torus surface. Then the collected trajectories are discretized via Gauss–Legendre collocation. Using the global error estimate and mesh refinement approach of Russell & Christiansen [1978], we control the error along each of these trajectories (in fact, for the CR3BP, we can often preserve the Hamiltonian value at each of the mesh states $\mathbf{X}_{i,0}$ within 10^{-15} of the nominal value). We do not, however, know what is happening between the N_2 trajectories on the torus surface.

What we seek is an error control method that fits well with our torus discretization. One approach is to look at the magnitude of the Fourier coefficients, and verify that beyond a certain order they are below a tolerance. An alternative approach that we use is to increase the number of trajectories on the torus surface by an integer factor c. Using the discrete Fourier transform, we can very efficiently generate a cylinder function $\mathbf{u}_{(c)}$ consisting of cN_2 trajectories (we often use $c = 2$). Rather than numerically correct this cylinder function, we average the vector field error over the corresponding torus,

$$\epsilon := \frac{1}{cN_2} \int_0^1 \sum_{k=1}^{cN_2} \left\| T\mathbf{f}_0(\mathbf{X}^k_{(c)}(\tau)) - \frac{d\mathbf{X}^k_{(c)}}{d\tau}(\tau) \right\|^2 d\tau \tag{2.35}$$

where $\mathbf{X}^k_{(c)}(\cdot)$ is each of the trajectories from (2.26) and $\mathbf{f}_0$ is the nominal vector field. (An alternate choice would be to use a supremum rather than an average.) This error estimate measures how well the torus matches the vector field between the discrete set of N_2 computed trajectories on its surface. If the error ϵ is above a set tolerance, we can increase the number of trajectories N_2 (i.e., increase the Fourier order M_2). This error control can all be done efficiently using the discrete Fourier transform at a computational cost much less than an iteration of the Newton method.

2.3.5 Flow on torus

An advantage of a collocation-based approach over a shooting-based method is that we directly have a continuous representation of the entire torus. Furthermore, the computed trajectories are parallel to the flow, so any trajectory is just a fixed shift from the computed set. This shift can be performed using the discrete Fourier transform. For many applications, it is desirable to be able to generate a quasi-periodic trajectory on the torus surface from an arbitrary starting point. Let $(\theta_{1,0}, \theta_{2,0})$ be the starting angles at time $t = 0$. Recall that each angle is parameterized over the unit interval. We can then use the formula

$$\mathbf{x}(t) = \mathbf{u}(\tau; \theta_{2,0} + \rho(k - \theta_{1,0})) \text{ where } k = \lfloor \theta_{1,0} + \omega_1 t \rfloor,\ \tau = (\theta_{1,0} + \omega_1 t) \pmod 1 \tag{2.36}$$

Given an initial angle pair, a trajectory can be very efficiently generated.

2.4 COMPUTATION OF STABILITY

We now investigate the linearized dynamics in the vicinity of a computed quasi-periodic invariant torus. We are particularly interested in hyperbolic tori and determining their associated stable and unstable directions. The method assumes the tori are reducible as described in Section 1.1.2. Stability information (the eigenvalues of the Floquet matrix) is extracted from the Jacobian matrix used for the collocation method. The corresponding eigenvectors are first determined for a circle on the invariant torus. For hyperbolic tori, we will show how to map the stable and unstable directions relative to the circle to the full invariant torus of the flow. By perturbing the torus in these directions and integrating forward or backward in time, we can numerically generate the global manifolds.

2.4.1 Extracting state-transition matrix

The state-transition matrix provides linear information about the dynamics in the vicinity of a reference solution. In particular, it allows us to map the evolution of a perturbation to the initial state (or changes to the parameters) along the trajectory. We present a simple algorithm to extract this information from the Jacobian matrix used for the collocation method described in Section 2.3.2. This approach is broadly applicable to boundary value problems solved via a collocation method. The result will then be applied to the computation of quasi-periodic torus stability.

Let us begin by assuming that we have converged to the solution of a boundary value problem such as (2.1). When a Newton method is used, the Jacobian is constructed. The first $N(m+1)n^*$ rows correspond to the collocation conditions matching the trajectory to the vector field and continuity constraints matching the polynomials to their neighbors. Recall that N is the number of mesh intervals, m is the number of collocation points in each interval, and n^* is the dimension of each state $\mathbf{X}_{i,j}$. Removing the remaining rows associated with other constraints, we have a linear system that variations in the states and parameters must satisfy in order to still have a continuous solution

that matches the vector field. This linear system is:

$$\left[\begin{array}{c|c|c} \mathbf{A} & \mathbf{B} & \mathbf{C} \end{array}\right] \left[\begin{array}{c} \delta\mathbf{X}_{0,0} \\ \hline \delta\mathbf{X}_{0,1} \\ \vdots \\ \delta\mathbf{X}_{N,0} \\ \hline \delta\boldsymbol{\Lambda} \end{array}\right] = \mathbf{0} \tag{2.37}$$

where the Jacobian (after removing the final rows) is partitioned such that $\mathbf{A}$ has dimension $N(m+1)n^* \times n^*$, $\mathbf{B}$ has dimension $N(m+1)n^* \times N(m+1)n^*$, and $\mathbf{C}$ has dimension $N(m+1)n^* \times n_p$ (where n_p is the number of free parameters). We can rearrange this system to relate changes in the initial state, $\delta\mathbf{X}_{0,0}$, and changes in the free parameters, $\delta\boldsymbol{\Lambda}$, to changes in the state along the trajectory,

$$\begin{aligned} \delta\mathbf{X} &= \boldsymbol{\Phi}\,\delta\mathbf{X}_{0,0} + \boldsymbol{\Psi}\,\delta\boldsymbol{\Lambda} \\ &= \left[\begin{array}{c} \mathrm{Id} \\ -\mathbf{B}^{-1}\mathbf{A} \end{array}\right] \delta\mathbf{X}_{0,0} + \left[\begin{array}{c} \mathbf{0} \\ -\mathbf{B}^{-1}\mathbf{C} \end{array}\right] \delta\boldsymbol{\Lambda} \end{aligned} \tag{2.38}$$

where Id is the $n^* \times n^*$ identity matrix, and where we make the following definitions:

$$\delta\mathbf{X} := \left[\begin{array}{c} \delta\mathbf{X}_{0,0} \\ \delta\mathbf{X}_{0,1} \\ \vdots \\ \delta\mathbf{X}_{N,0} \end{array}\right], \; \boldsymbol{\Phi} := \left[\begin{array}{c} \boldsymbol{\Phi}_{0,0} \\ \boldsymbol{\Phi}_{0,1} \\ \vdots \\ \boldsymbol{\Phi}_{N,0} \end{array}\right], \; \boldsymbol{\Psi} := \left[\begin{array}{c} \boldsymbol{\Psi}_{0,0} \\ \boldsymbol{\Psi}_{0,1} \\ \vdots \\ \boldsymbol{\Psi}_{N,0} \end{array}\right]. \tag{2.39}$$

Here each matrix $\boldsymbol{\Phi}_{i,j}$ has dimension $n^* \times n^*$, and each matrix $\boldsymbol{\Psi}_{i,j}$ has dimension $n^* \times n_p$. The computational cost for computing $\boldsymbol{\Phi}$ and $\boldsymbol{\Psi}$ is approximately the same as a single iteration of the Newton method since a majority of the time is spent factoring sparse matrix $\mathbf{B}$.

The power of this approach is that we not only have the state transition matrix at the final time, we have its value at all the mesh and collocation times. This allows us to map an initial perturbation $\delta\mathbf{X}_{0,0}$ to all these times giving a continuous piecewise polynomial representation of the time evolution of the perturbation, $\delta\mathbf{X}(\tau)$.

When computing a periodic orbit, the matrix $\boldsymbol{\Phi}_{N,0}$ is referred to as the monodromy matrix and provides stability information about the periodic orbit. We will see that this matrix can also be used to determine stability information about a quasi-periodic torus.

2.4.2 Linear stability of torus

Consider the circle function $\mathbf{w}(\cdot) := \mathbf{u}(0; \cdot) : \mathbb{T}^1 \to \mathbb{R}^n$ that parameterizes an invariant circle of the time-T stroboscopic map $\boldsymbol{\varphi}_T$. From the quasi-periodic invariance condition (1.4), this function is a fixed point of the map $\mathbf{G} : U \to U$ on the space of circle functions,

$$\mathbf{G}(\mathbf{w}(\cdot)) := \mathrm{Rot}(-\rho) \circ \boldsymbol{\varphi}_T(\mathbf{w}(\cdot)) \tag{2.40}$$

where $\mathrm{Rot}(-\rho) : U \to U$ shifts rotates the parameterization by $-\rho$. We can proceed to find the stability of the invariant circle (and subsequently the invariant torus) by studying the eigenvalues μ and eigenfunctions $\delta\mathbf{w}(\cdot)$ of the map's linearization,

$$\begin{aligned} \frac{\partial \mathbf{G}}{\partial \mathbf{w}}(\mathbf{w}(\cdot))\, \delta\mathbf{w}(\cdot) &= \mathbf{R}(-\rho) \circ (\boldsymbol{\Phi}(\mathbf{w}(\cdot); T)\, \delta\mathbf{w}(\cdot)) \\ &= \mu\, \delta\mathbf{w}(\cdot). \end{aligned} \tag{2.41}$$

The operator $\partial\mathbf{G}/\partial\mathbf{w}$ incorporates the linearization of the stroboscopic map, $\boldsymbol{\Phi}(\mathbf{w}(\cdot); T)$, which is the state transition matrix after time T, but it also removes the rotation about the invariant circle by including the composition with $\mathrm{Rot}(-\rho)$. This way a perturbation $\delta\mathbf{w}(\theta_2)$ and mapped perturbation $\delta\bar{\mathbf{w}}(\theta_2)$ have the same base point $\mathbf{w}(\theta_2) = \mathbf{u}(0; \theta_2)$.

Jorba [2001] shows that the eigenvalues μ of equation (2.41) correspond to the eigenvalues of the Floquet matrix $\mathbf{B}$ defined in equation (1.6) up to a rotation of the form $e^{ik(2\pi\rho)}$, $k \in \mathbb{Z}$. Therefore, the full spectrum lies densely on circles in the complex plane. For a real, non-unity eigenvalue of equation (2.41), if the entire circle $\mathbf{w}(\cdot)$ is perturbed in the direction of the corresponding eigenfunction $\delta\mathbf{w}(\cdot)$, an iteration of the map simply expands or contracts in this direction. This is a linear approximation of stable and unstable manifold directions, which is illustrated in Figure 2.2.

When the cylinder function space is discretized, the operator from (2.41) can be represented by the matrix $[\mathbf{G}_\mathbf{w}] = \mathbf{R}(-\rho)\boldsymbol{\Phi}_{N,0}$. The state transition matrix is extracted from the Jacobian matrix for the collocation method. It is evaluated using the converged, discretized torus $\mathbf{u}$ (such as from the last Newton iteration). It is important to note that this matrix acts directly on variations of the evenly-spaced circle states. Jorba uses a similar operator except in terms of Fourier coefficients. If

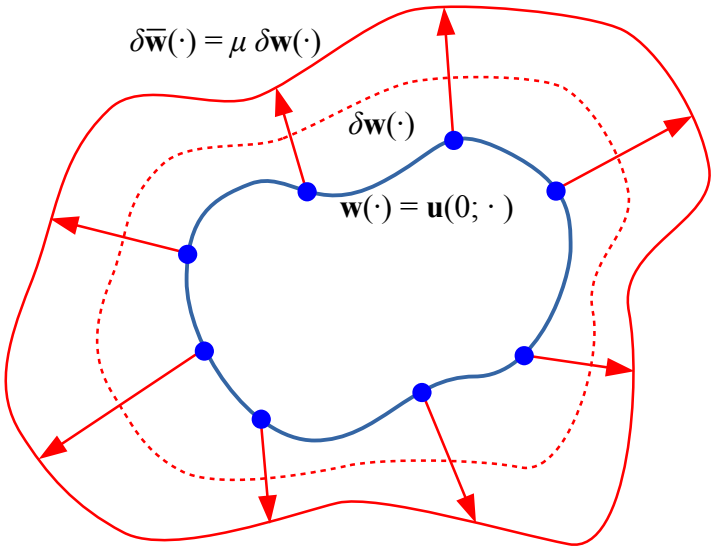

Figure 2.2: Illustration of hyperbolic eigenvalue and eigenfunction

we represent the N_2 array of state variations as vectors $\{\delta\mathbf{w}\}$ and $\{\delta\bar{\mathbf{w}}\}$, they are related by

$$\{\delta\bar{\mathbf{w}}\} = [\mathbf{G}_{\mathbf{w}}]\,\{\delta\mathbf{w}\}\,. \tag{2.42}$$

This matrix is of dimension $(nN_2)\times(nN_2)$ and has nN_2 eigenvalues since it is finite dimensional. This matrix is also dense and potentially quite large, but schemes exists for determining its eigenstructure. The eigenvalues of $[\mathbf{G}_{\mathbf{w}}]$ correspond to the eigenvalues of the Floquet matrix $\mathbf{B}$ up to a rotation about the origin in the complex plane. The magnitude of the eigenvalues, however, is maintained providing stability information. If sets of eigenvalues off the unit circle exist, it corresponds to stable and unstable motion in the vicinity. The eigenvectors corresponding to real eigenvalues in the sets give the stable and unstable manifold tangent directions at each of the evenly-spaced points on the invariant circle. A depiction of these points and vectors is included in Figure 1.3.

2.4.3 Transition to full torus

Thus far we have only considered the manifold tangent directions $\delta\mathbf{w}(\cdot)$ relative to the initial (i.e., $\tau = 0$) circle function $\mathbf{w}(\cdot) := \mathbf{u}(0;\cdot) : \mathbb{T}^1 \to \mathbb{R}^n$ of the stroboscopic map. However, we would like to generate the tangent directions $\delta\mathbf{u}$ relative to the full torus parameterized by $\mathbf{u} : [0,1]\times\mathbb{T}^1 \to \mathbb{R}^n$.

This can easily be performed using the state transition matrix $\mathbf{\Phi}$. Since this matrix maps the variations of the collected state $\mathbf{X}(\tau) \in \mathbb{R}^{nN_2}$, we can compute the manifold tangent direction as

$$\delta\mathbf{u}(\tau;\theta_2) = \mu^{-\tau}\mathbf{\Phi}(\tau)\,\delta\mathbf{w}(\theta_2). \tag{2.43}$$

Since the state transition matrix also scales the tangent direction, we include factor $\mu^{-\tau}$ to "undo" this scaling. Finally, to initialize the stable or unstable manifold, we can choose a small factor $\epsilon > 0$, and linearly approximate points on the manifold using $\mathbf{u}(\tau;\theta_2) \pm \epsilon\,\delta\mathbf{u}(\tau;\theta_2)$. The simplest approach is to numerically propagate forward or backward in time to generate the full manifold. These stable and unstable manifolds will each be three-dimensional for a two-dimensional invariant torus in the phase space.

CHAPTER 3

INVARIANT TORI IN ASTRODYNAMICS

In this chapter we illustrate the numerical method for computing quasi-periodic orbits and their stability by considering astrodynamical examples. We consider both the CR3BP (an autonomous system) and the ER3BP (a periodically-forced system) with a mass ratio corresponding to the Earth–Moon system. For the ER3BP, however, we continue solutions beyond the system's true eccentricity. For both problems, families of tori are generated along with associated stable and unstable manifolds.

As an extended example, we also consider the planar dynamics in the Hill restricted four-body problem (HR4BP). In particular, we model the motion of a spacecraft subject to the influence of the Sun, Earth, and Moon. This allows us to numerically investigate the role of strong resonances by studying both periodic and quasi-periodic orbits. This discussion will appear in Olikara et al. [2016].

3.1 CIRCULAR RESTRICTED THREE-BODY PROBLEM

In the CR3BP, the gravitational interaction of three bodies, one with infinitesimal mass, is modeled. We assume that the two massive, primary bodies travel in circular orbits. The third body is located at $\mathbf{q} = (x, y, z)$ in a barycentric rotating frame, which is defined such that the primary bodies are fixed along the x-axis. Its state $\mathbf{x} = (\mathbf{q}, \dot{\mathbf{q}}) \in \mathbb{R}^6$ is governed by the nondimensional equation of motion

$$\begin{bmatrix} \dot{\mathbf{q}} \\ \ddot{\mathbf{q}} \end{bmatrix} = \dot{\mathbf{x}} = \mathbf{f}_0(\mathbf{x}) = \begin{bmatrix} \dot{\mathbf{q}} \\ \partial U / \partial \mathbf{q}^\intercal + 2\dot{\mathbf{q}} \times \hat{\mathbf{z}} \end{bmatrix}, \tag{3.1}$$

which depends on a force potential-like function

$$U(\mathbf{q}) = \frac{1-\mu}{r_1} + \frac{\mu}{r_2} + \frac{1}{2}\left(x^2 + y^2\right). \tag{3.2}$$

The parameter $\mu \in [0, 0.5]$ relates the primaries' masses, r_1 and r_2 are the distances of the third body to each primary (the larger and smaller primaries are located at $x = -\mu$ and $x = 1 - \mu$, respectively), and $\hat{\mathbf{z}}$ is a unit vector along the z-axis, the direction of the system angular momentum. For the Earth–Moon system, we use mass parameter $\mu = 0.01215$, which is fixed for all solutions and, thus, not included as a free parameter.

The CR3BP is an autonomous Hamiltonian system, which provides insight into its dynamical structure. Its Hamiltonian function expressed in the non-canonical coordinate set $\mathbf{x} = (\mathbf{q}, \dot{\mathbf{q}})$ is

$$H(\mathbf{x}) = \frac{1}{2} \|\dot{\mathbf{q}}\|^2 - U(\mathbf{q}). \tag{3.3}$$

Since the Hamiltonian function does not depend on time, it is an integral of motion. It is often referred to as the "energy" even though it does not precisely correspond to the third body's energy (note that the Hamiltonian function is constructed in a rotating frame). For historical reasons, a related integral of motion, the Jacobi constant $C := -2H$, is commonly presented in the literature. Some authors use an alternate definition $\bar{C} := -2H + \mu(1 - \mu)$ such that two of the equilibrium points (L_4 and L_5) have value $\bar{C} = 3$. There are no additional integrals of motion.

While the phase space is six-dimensional, an energy surface is five-dimensional. This surface is the set of all states having the same Hamiltonian value H_0. Since any CR3BP trajectory preserves its Hamiltonian value, the energy surface is invariant. A consequence is that on a given energy surface, not all positions are accessible. From an inspection of (3.3), it follows that $U(\mathbf{q}) \geq -H_0$ since the square of the velocity magnitude is nonnegative. We refer to the set of positions where this inequality is violated as the forbidden region. The boundary of this region is the so-called zero-velocity surface since it corresponds to states with $\|\dot{\mathbf{q}}\| = 0$. The geometry of these surfaces is discussed in detail in Szebehely [1967].

The set of states such that $z = \dot{z} = 0$ is also invariant. This corresponds to a third body whose position and velocity are in the plane of the primary bodies, in which case there are no forces normal to the plane. This restriction is known as the planar CR3BP. In the following analysis, however, we will focus on the spatial CR3BP, which includes out-of-plane motion. We first summarize the equilibrium points and periodic orbits; since these results are independent from the quasi-periodic

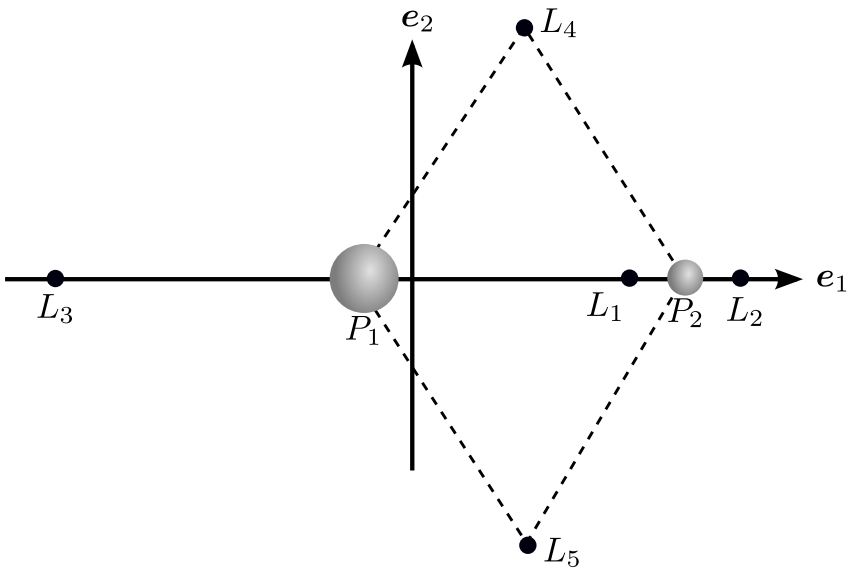

Figure 3.1: Libration points of the CR3BP (not to scale)

computation scheme, we include their descriptions from Olikara [2010] in Sections 3.1.1 and 3.1.2. We then compute quasi-periodic tori in their vicinity using the method of Chapter 2.

3.1.1 Libration points

The zero-dimensional tori in the CR3BP consist of the five libration points shown in Figure 3.1. All the equilibrium points lie in the plane of the primaries' motion. The "collinear" L_1, L_2, and L_3 libration points are along the axis connecting the primaries. Each corresponds to a root of a quintic polynomial Szebehely [1967] and can be found iteratively using a Newton method. The "triangular" L_4 and L_5 libration points are at the corners of equilateral triangles.

We are interested in studying the phase space structure near the libration points, particularly the higher-dimensional invariant tori. The dynamics in the vicinity of the libration points can be qualitatively understood using the stable, unstable, and center manifold theorems for continuous flows [Guckenheimer & Holmes, 2002; Perko, 1991]. To apply these theorems, we consider the eigenvalues of the 6×6 matrix $\mathbf{Df}_0(\bar{\mathbf{x}})$ corresponding to the linearization of the CR3BP vector field $\mathbf{f}_0$ relative to the libration point $\bar{\mathbf{x}}$. Since the eigenvalues of the matrix $\mathbf{Df}_0(\bar{\mathbf{x}})$ are symmetric

Table 3.1: Linear stability of libration points

	$0 \leq \mu < \mu_{\text{crit}}$	$\mu_{\text{crit}} < \mu \leq 0.5$
L_1	center × center × saddle	
L_2	center × center × saddle	
L_3	center × center × saddle	
L_4	center × center × center	center × complex saddle
L_5	center × center × center	center × complex saddle

across the real and imaginary axes for a Hamiltonian system Meyer & Hall [1992], we categorize the stability type for each libration point in a system with mass parameter μ using the components listed in Table 3.1. The label "center" implies a pair of eigenvalues with zero real part. The label "saddle" denotes a pair of eigenvalues with nonzero real part, one eigenvalue possessing a negative real part and the other a positive real part. The label "complex saddle" corresponds to four eigenvalues with nonzero real and imaginary parts that are symmetric across both axes.

For any CR3BP system, a linearization relative to the collinear libration points L_1, L_2, and L_3 yields two pairs of eigenvalues corresponding to center motion and one pair of eigenvalues that represent a hyperbolic saddle. Applying the stable, unstable, and center manifold theorem, we conclude that there exists a four-dimensional center manifold, a one-dimensional stable manifold, and a one-dimensional unstable manifold for each of these libration points. The four-dimensional center manifold contains a two-parameter family of two-dimensional tori. Since there is at least one unstable direction, the collinear libration points are termed to be unstable. Locally, we expect an arbitrary perturbation to the libration point state to grow exponentially in time.

Unlike the collinear libration points, the stability of the triangular libration points, L_4 and L_5, is system dependent. As demonstrated in Szebehely [1967], for systems with a mass parameter less than a critical value, $\mu < \mu_{\text{crit}} = 0.038521$, all the pairs of eigenvalues correspond to center motion and, thus, there is a six-dimensional center manifold consisting of a three-parameter family of three-dimensional tori. This includes the Earth-Moon CR3BP system. On the other hand, a mass parameter $\mu > \mu_{\text{crit}}$ results in two pairs of eigenvalues associated with complex saddle behavior. In

this case, L_4 and L_5 are unstable.

3.1.2 Periodic orbits

Since the dynamics associated with all of the libration points contain a center component, periodic orbits, or one-dimensional invariant tori, exist in the vicinity of each point. The periodic behavior is confirmed by applying the Lyapunov center theorem [Meyer & Hall, 1992]. A detailed study of periodic libration point orbits in the CR3BP is available in Doedel et al. [2007]. In this section we present a brief overview of some periodic orbit families in the Earth-Moon system that are of interest when computing quasi-periodic tori. Specifically, we are interested in periodic orbits with a center component corresponding to quasi-periodic motion, i.e., orbits with a monodromy matrix possessing at least one pair of nontrivial eigenvalues on the unit circle.

Two one-parameter families of periodic orbits emanate from each of the collinear libration points. These are the Lyapunov orbits, plotted near L_1 in Figure 3.2 and near L_2 in Figure 3.3, as well as the vertical orbits in the vicinity of L_1 in Figure 3.4 and in the vicinity of L_2 in Figure 3.5. Recall that all of the plotted families correspond to the Earth-Moon system. Similar families exist about the L_3 libration point. Note that we plot only a finite number of the members, and the families continue beyond the orbits that appear in Figures 3.2–3.5. In addition, orbits in blue denote periodic orbits possessing at least one quasi-periodic center component that can be used to initialize a first member of a family of quasi-periodic tori. The orbits in red do not have quasi-periodic tori that emanate from them.

Close to the L_1 and L_2 libration points, we observe the Lyapunov orbits, all of which lie in the plane of the primary motion, contain a quasi-periodic center component. There is a transition in the family to orbits without this center component. At this first change in stability, a bifurcation occurs and the Lyapunov family intersects another family, known as the halo orbits. The out-of-plane halo family in the vicinity of each of the collinear libration points is symmetric across the xy-plane of the primaries and can be divided into two branches, which we term the northern and southern halo families. The Earth-Moon northern L_1 halo family appears in Figure 3.6, and the northern L_2 family

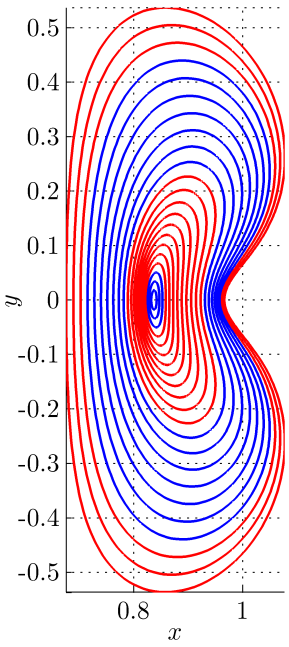

Figure 3.2: L_1 planar periodic orbits

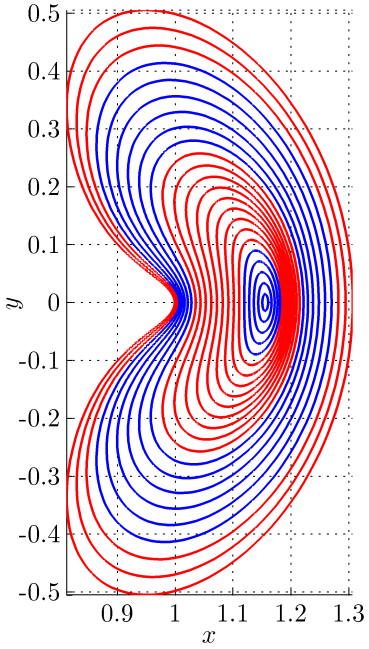

Figure 3.3: L_2 planar periodic orbits

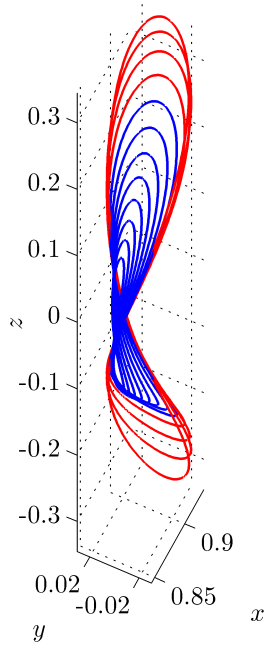

Figure 3.4: L_1 vertical periodic orbits

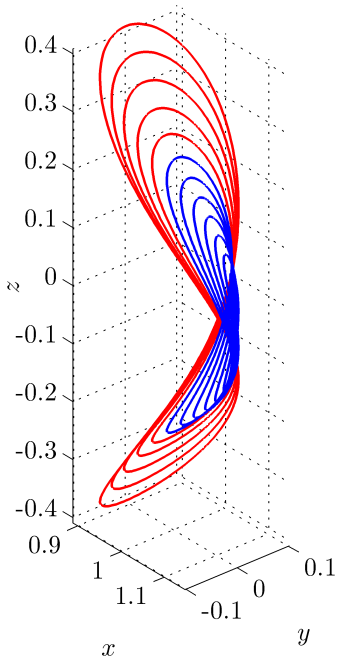

Figure 3.5: L_2 vertical periodic orbits

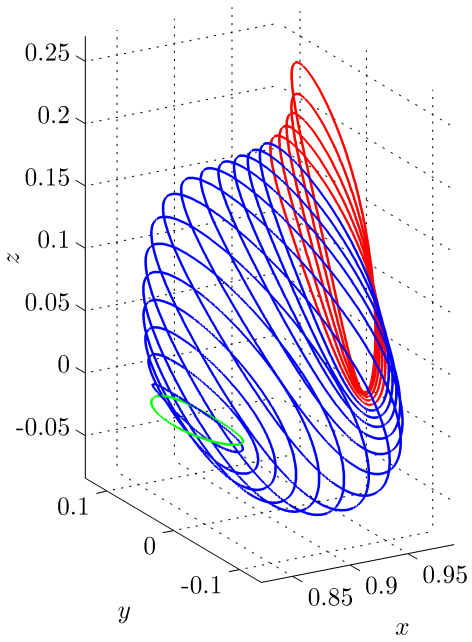

Figure 3.6: L_1 northern halo periodic orbits

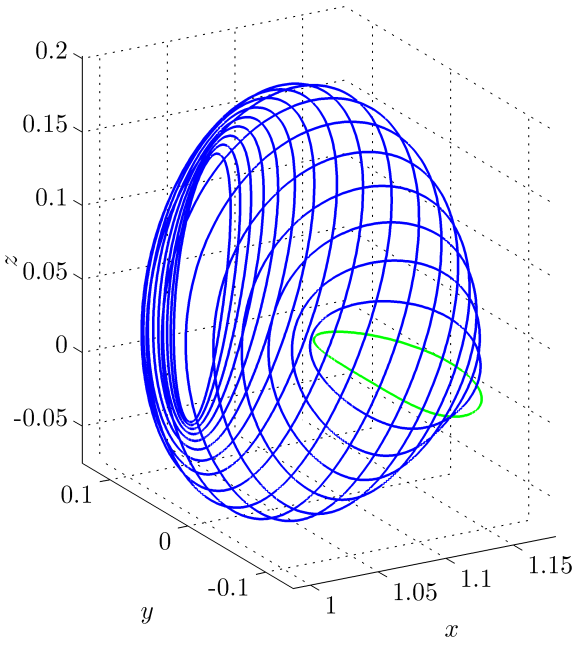

Figure 3.7: L_2 northern halo periodic orbits

is plotted in Figure 3.7. Note that these families extend beyond the orbits that are illustrated. The green orbit in each figure denotes the bifurcating orbit and belongs to both the Lyapunov and halo families. Consistent with the previous plots, we use the color blue to identify periodic orbits from which quasi-periodic tori emanate. Another family of periodic orbits, identified as the axial family, bifurcates from the Lyapunov family at its second change in stability, and ends at a bifurcation with the vertical family at its first change in stability. However, none of the axial orbits contain a quasi-periodic center component.

3.1.3 Quasi-periodic orbits

The quasi-periodic boundary value problem for an autonomous Hamiltonian system such as the CR3BP is given by 2.1. Recall that two additional parameters λ_1 and λ_2 are added to the nominal vector field $\mathbf{f}_0$ in order to have a matching number of parameters as constraints. The parameters depend on the gradients of the actions $(\partial I_1/\partial \mathbf{x})^\intercal$ and $(\partial I_2/\partial \mathbf{x})^\intercal$, which are computed using (2.18) and (2.19) and do not require the computation of the actions themselves. These terms depend on the transformation from our computational coordinate set $\mathbf{x} = (\mathbf{q}, \dot{\mathbf{q}})$ to the canonical coordinate set

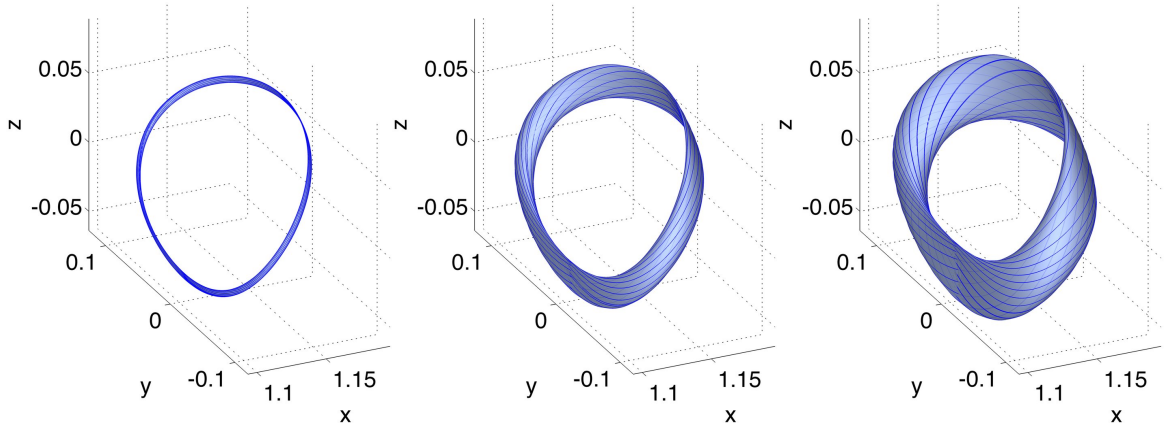

Figure 3.8: Members of quasi-halo torus family emanating from L_2 halo orbit

$\mathbf{y} = (\mathbf{q}, \mathbf{p})$, specifically the matrix

$$-\frac{\partial \mathbf{y}^{\mathsf{T}}}{\partial \mathbf{x}} \mathbf{J} \frac{\partial \mathbf{y}}{\partial \mathbf{x}} = \left[\begin{array}{cccc|cccc} & +2 & & & -1 & & & \\ -2 & & & & & -1 & & \\ & & & & & & & -1 \\ & & & & & & & \\ \hline +1 & & & & & & & \\ & +1 & & & & & & \\ & & +1 & & & & & \end{array}\right], \tag{3.4}$$

which is constant for the CR3BP formulation. This allows us to easily compute the gradients of the actions from the function $\mathbf{u} : [0, 1] \times \mathbb{T}^1 \to \mathbb{R}^n$.

Recall that the boundary value problem fixes the Hamiltonian value within the torus family. This constraint reduces the two-parameter family of two-dimensional quasi-periodic tori to a single parameter, which can be stepped along with pseudo-arclength continuation. Starting from an L_2 halo periodic orbit in the Earth–Moon system, we generate representative members of the quasi-halo family, all members having Jacobi constant $C = 3.132$ ($H = -1.566$), shown in Figure 3.8. A segment of the quasi-periodic trajectory on the torus surface is also plotted.

Like the associated halo orbit, these quasi-periodic orbits are hyperbolic. In Figure 3.9 we show the stable and unstable directions relative to one member of the quasi-halo family. Perturbing the torus along the tangent directions and propagating backward or forward in time allows us to generate the three-dimensional stable or unstable manifold. If we propagate the perturbed torus for discrete amounts of time, its image is also a torus. The continuous sequence of these tori sweep out

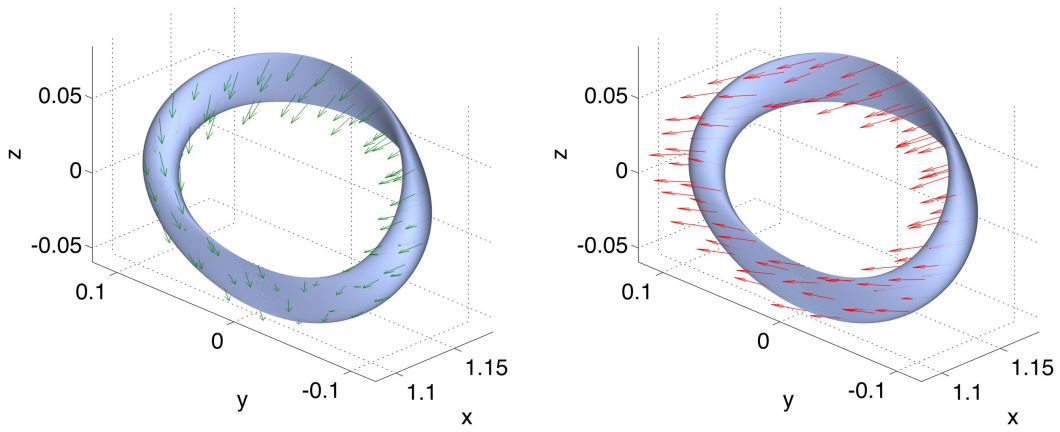

Figure 3.9: Tangent directions for stable and unstable manifolds of quasi-halo torus

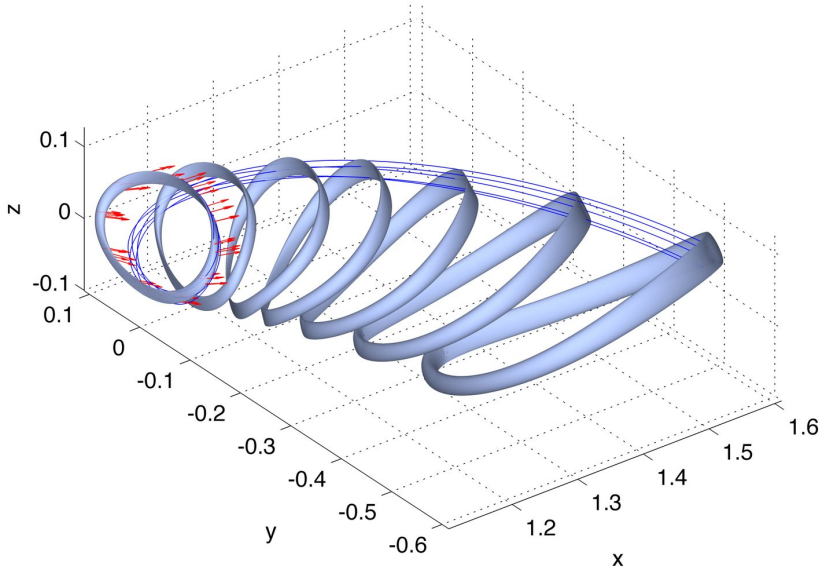

Figure 3.10: Snapshots of L_2 quasi-halo unstable manifold departing away from Moon

the manifold. Note that the tangent directions can be flipped, i.e., multiplied by -1, to generate the other "half" of the stable or unstable manifold. Part of a quasi-halo's unstable manifold departing away from the smaller primary, the Moon, is shown in Figure 3.10. Manifold trajectories associated with one invariant circle on the torus are included. In Figure 3.11 we present the torus's stable manifold arriving from the direction of the Moon. Note that the manifold becomes twisted in the Moon's vicinity.

The method can be directly applied to other families with only a change in the initial orbit.

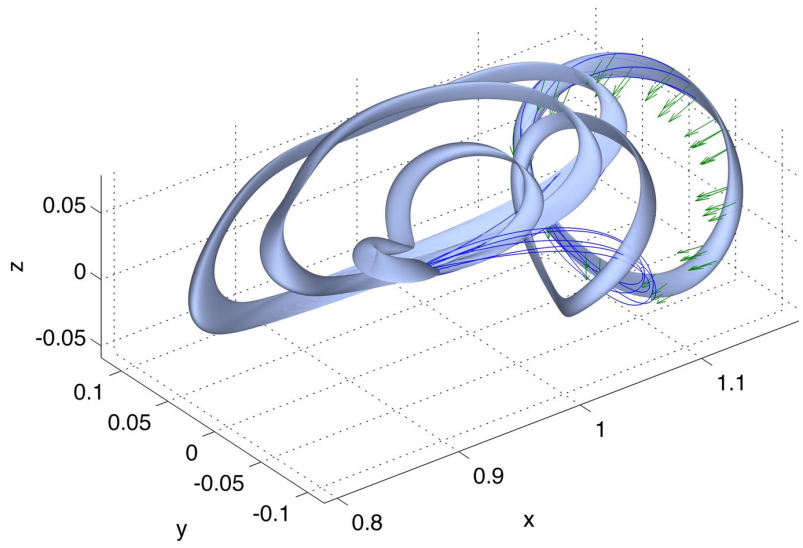

Figure 3.11: Snapshots of L_2 quasi-halo stable manifold arriving from Moon's vicinity

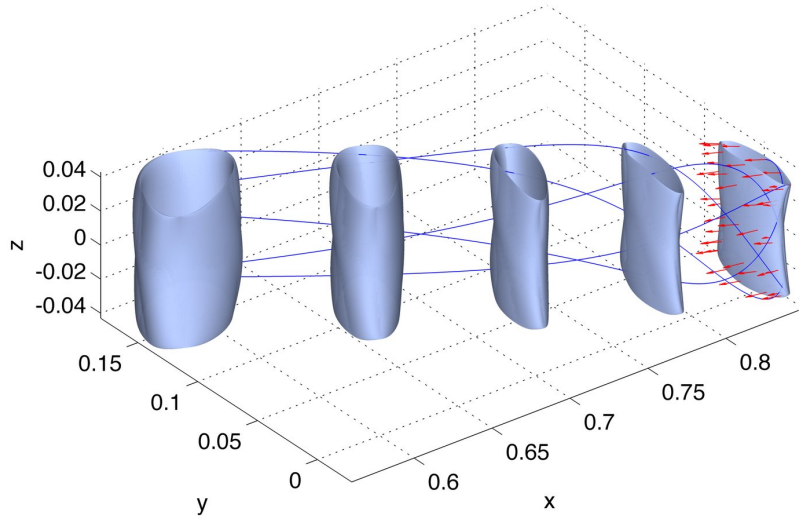

Figure 3.12: Snapshots of L_1 Lissajous unstable manifold departing towards Earth

Initializing the family from a planar L_1 Lyapunov orbit, we show a two-dimensional member from the Lissajous family in Figure 3.12 along with its three-dimensional unstable manifold departing in the direction of the Earth.

In order to get a graphical depiction of the Earth–Moon L_1 and L_2 center manifold structure, we restrict ourselves to the fixed energy level $C = 3.132$. We consider intersections of the torus families with the plane $z = 0$ with crossings in the direction $\dot{z} > 0$. The families are shown in

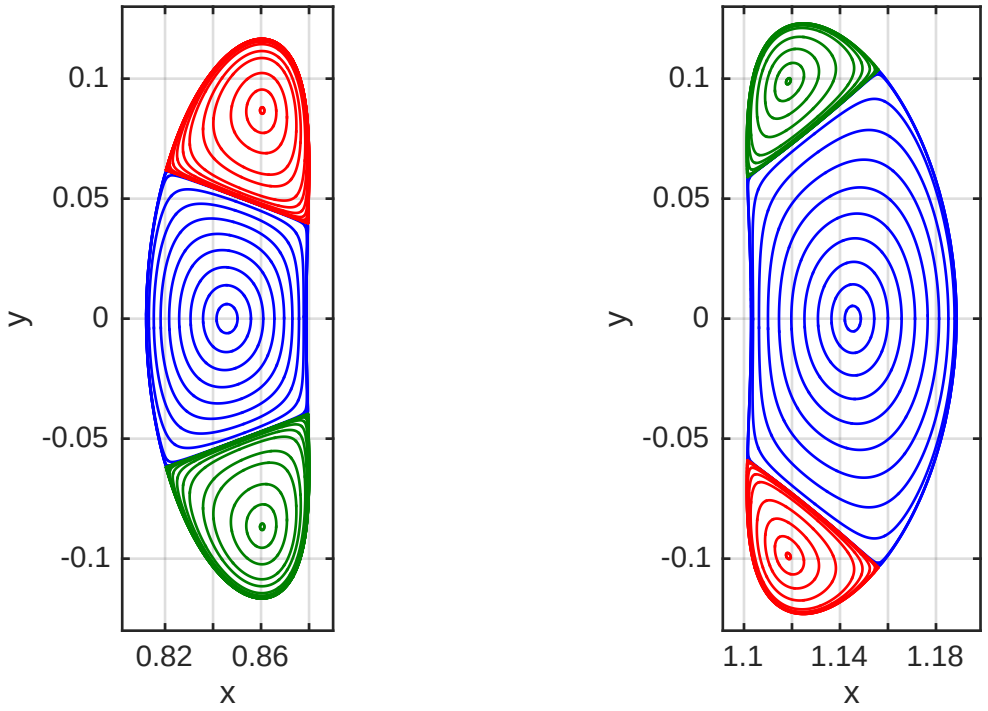

Figure 3.13: Crossings of $z = 0$ plane ($\dot{z} > 0$) of Earth–Moon L_1 (left) and L_2 (right) center manifold tori at a fixed energy level

Figure 3.13. Each torus is computed without parallelization in about 2 seconds using a Fourier order $M_2 = 25$ ($N_2 = 51$), $m = 6$ collocation points per interval, and a global error tolerance along each trajectory of 10^{-10} (the Jacobi constant along each trajectory is preserved within 10^{-15}). Each plot is computed in about a minute. In blue are the Lissajous quasi-periodic orbits. Each circle corresponds to the intersection of a two-dimensional invariant torus with the plane. At the center of each plot is a single point corresponding to the vertical periodic orbit (see Figures 3.4 and 3.5) at this energy level. In green are the northern quasi-halo orbits, and in red are the southern quasi-halo orbits. At the center of each of these families are points corresponding to the northern and southern halo periodic orbits (see Figures 3.6 and 3.7 for the northern periodic orbit families) at this energy level. Bounding each center manifold at this energy level are the planar Lyapunov periodic orbits. These periodic orbits are in the red regions of Figures 3.2 and 3.3, and they do not have quasi-periodic orbits emanating from them. In fact, restricted to this energy level, the planar

Lyapunov periodic orbits have stability of type saddle × saddle, and it is their stable and unstable manifolds that form a boundary to the center manifold.

All of the torus families in Figure 3.13 are normally hyperbolic. Since they all belong to the same energy level, there is a possibility that the unstable manifold of one torus intersects with the stable manifold of another. In Chapter 4, we will compute a family of these heteroclinic connections. They enable a spacecraft to naturally pass between the libration points.

3.2 ELLIPTIC RESTRICTED THREE-BODY PROBLEM

The two primary bodies in the ER3BP move on elliptic orbits with eccentricity e about their barycenter. We consider the motion of a third body with infinitesimal mass. As with the CR3BP, the primaries are fixed along the x-axis, and lengths are normalized by the distance between them. However, this distance is now time-varying, which allows the the five libration points to remain equilibrium solutions in the nondimensional rotating reference frame. The ER3BP equation of motion is given by

$$\begin{bmatrix} \dot{\mathbf{q}} \\ \ddot{\mathbf{q}} \end{bmatrix} = \dot{\mathbf{x}} = \mathbf{f}_0(\mathbf{x}, \theta_2; e) = \begin{bmatrix} \dot{\mathbf{q}} \\ (1 + e\cos\theta_2)^{-1}(\partial U/\partial \mathbf{q}^\intercal - ze\cos\theta_2\,\hat{\mathbf{z}}) + 2\dot{\mathbf{q}} \times \hat{\mathbf{z}} \end{bmatrix} \tag{3.5a}$$

where U is defined by (3.2), and we can append an equation for the dynamics on a quasi-periodic solution:

$$\begin{bmatrix} \dot{\theta}_1 \\ \dot{\theta}_2 \end{bmatrix} = \dot{\boldsymbol{\theta}} = \boldsymbol{\omega} = \begin{bmatrix} \omega_1 \\ 1 \end{bmatrix}. \tag{3.5b}$$

Note that the true anomaly θ_2 of the primaries, rather than time, is used as the independent variable in these equations. However, it is simple to switch between these two. We can also note that when parameter $e = 0$ in equation (3.5a), we recover the CR3BP equation of motion (3.1).

Since two-dimensional quasi-periodic tori in the ER3BP fill a role similar to periodic orbits in the CR3BP, we can initialize the ER3BP quasi-periodic orbits from the CR3BP periodic orbits. For obtaining families, we fix the stroboscopic time T to match the periodic orbit's period and the frequency $\omega_2 = 1$ to match the primaries' frequency. The eccentricity e is allowed to vary. We include a phase constraint for angle θ_1. A constraint for angle θ_2 is not necessary since it appears

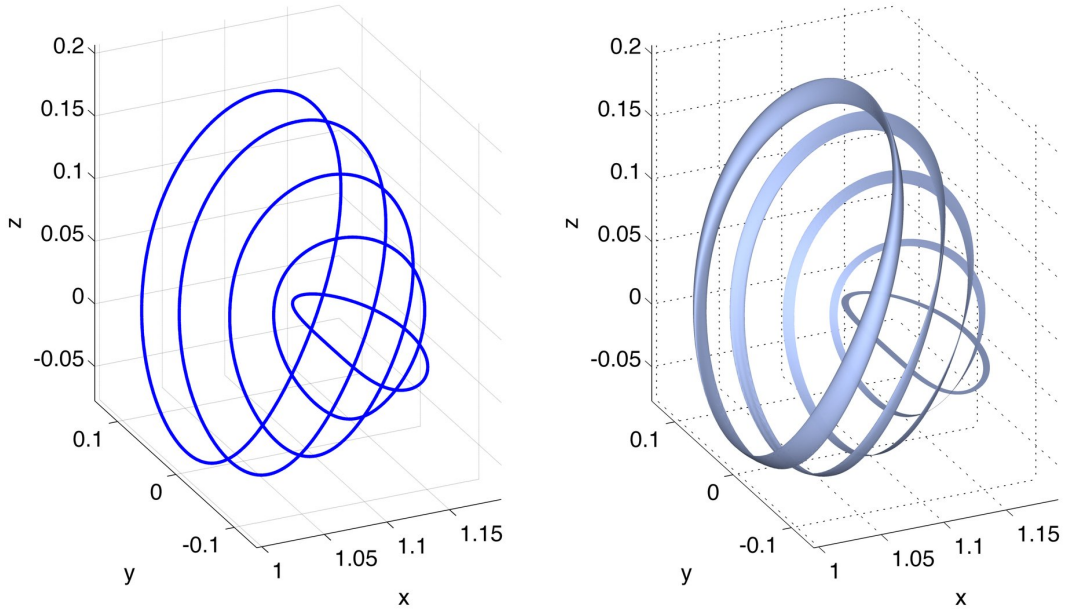

Figure 3.14: CR3BP L_2 halo orbit family members (left) and corresponding ER3BP ($e = 0.1$) quasi-periodic tori (right).

explicitly in the equation of motion (3.5a). Finally, we use pseudo-arclength continuation to generate a family of quasi-periodic orbits emanating from a periodic orbit in the CR3BP.

For this example we consider a fictitious system with an Earth–Moon mass parameter $\mu = 0.01215$ but an arbitrary eccentricity e. In Figure 3.14 we show periodic orbit members of the CR3BP halo family about libration point L_2. Applying the method presented, we can continue each of these solutions as quasi-periodic orbits. In the figure we include the corresponding members at eccentricity $e = 0.1$. We see that the members of the original family persists except with higher dimension. Each orbit has the same stroboscopic time T as the period of its associated CR3BP periodic orbit. For one of the ER3BP members we show its associated unstable manifold in Figure 3.15.

3.3 HILL RESTRICTED FOUR-BODY PROBLEM

We now consider an extended application [Olikara et al., 2016]. The idea is to study an intermediate model between the CR3BP and reality so as to consider the most significant perturbations while neglecting lesser ones. The primary perturbation on a spacecraft near an Earth–Moon libration point is from the Sun. Similarly, Sun–Earth libration point orbits can be significantly perturbed

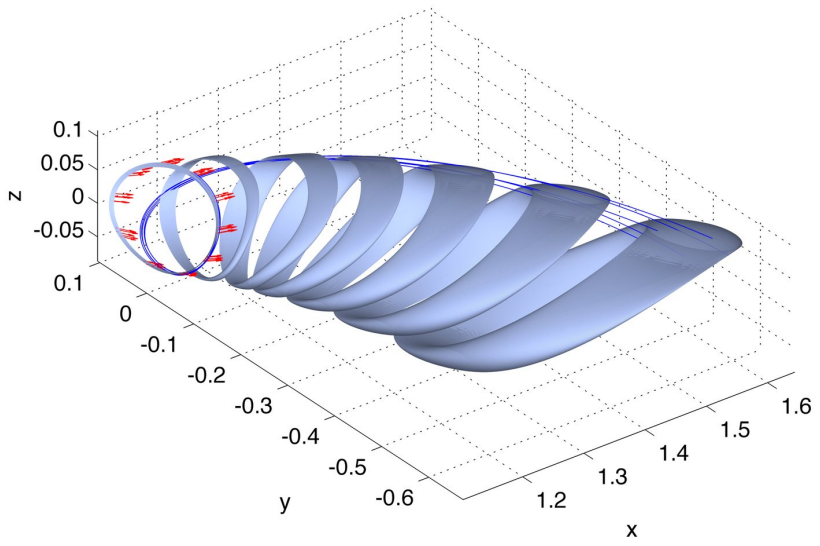

Figure 3.15: Snapshots of ER3BP quasi-halo unstable manifold departing away from Moon.

by the Moon. Both of these situations are addressed by considering a restricted four-body model consisting of the Sun, Earth, Moon, and spacecraft. Notably, in such a model invariant solutions can still exist. The difference between modeling the Sun–Earth and Earth–Moon libration points in a restricted four-body problem is simply the choice of coordinates; the dynamics are unchanged between the reference frames.

The simplest restricted four-body problem is the bicircular model [Simó et al., 1995]. In this model, we assume that the Earth–Moon barycenter travels in a circular orbit about the Sun, and the Earth and Moon travel in circular orbits about their barycenter. This assumption is not consistent, however, with Newtonian motion since the three primary bodies do not follow a solution to the general three-body problem.

Another option is to use a coherent restricted four-body model. It is possible to find a periodic solution to the general three-body problem such that the bodies' masses match the Sun, Earth, and Moon, and their relative configuration repeats each synodic month (about 29.53 days). The motion of the fourth body with infinitesimal mass has been studied in earlier works [Andreu, 1999; Gúzman, 2001] and is sometimes referred to as the quasi-bicircular model. An alternative coherent approach is to construct the relative motion of the Earth and Moon as a periodic solution to Hill's problem with

the Sun as the much more massive primary. Then when we consider the motion of the fourth body, we have the Hill restricted four-body problem (HR4BP) [Mohn & Kevorkian, 1967; Scheeres, 1998]. In either situation we assume that the Earth and Moon lie in the ecliptic plane, while in reality their relative orbit has an average inclination of 5.14°. Also note that while these models are coherent, we do not match the eccentricities of Earth's orbit about the Sun (0.0167) or the Moon's orbit about the Earth (0.0549).

In this section we consider motion near the L_1 and L_2 collinear libration points of the HR4BP in the Sun–Earth and Earth–Moon reference frames. Note that since the Sun is about 1 AU from the Earth and Moon, the magnitude of the Sun's perturbation is approximately constant in the vicinity of the Earth–Moon libration points. Within families of orbits about the Sun–Earth L_1 and L_2 libration points, however, the minimum distance to the Moon varies significantly, and the Moon's influence is much greater for larger amplitude orbits.

Unlike Hill's problem or the CR3BP, which are autonomous systems, time appears periodically in the HR4BP equations of motion and repeats each synodic month. As a consequence, invariant objects from the autonomous system generally turn into objects one dimension higher [Jorba & Villanueva, 1997b]. The equilibrium points become periodic orbits, and most periodic orbits become quasi-periodic orbits lying on two-dimensional invariant tori. Two-dimensional invariant tori (such as Lissajous and quasi-halo orbits) generally become three-dimensional invariant tori in the HR4BP, but these orbits are not currently considered.

The results presented in this section are obtained using the collocation-based torus computation scheme from Chapter 2. The advantage of a numerical approach over a semi-analytic one is that we are not limited by the convergence radius of an expansion about a reference solution. We do, however, need to compute objects one at a time, and separate computation of resonances is required. Numerical and semi-analytic results complement each other well. For instance, we can numerically verify some of the Earth–Moon results obtained semi-analytically by Andreu [1999] in a similar model and expand them to a larger region.

3.3.1 HR4BP in Sun–Earth frame

The Hill restricted four-body problem is developed by Scheeres [1998] and constructed in a rotating reference frame of the smaller two primaries, in our case the Earth and the Moon. The motion of these primaries is the classical Hill variation orbit that can be computed to any desired accuracy in powers of a period parameter m. We use the parameter value $m = 0.0808$ that relates the period of the Earth–Moon barycenter about the Sun to the period of the Earth and Moon about their barycenter. The model depends on a second parameter μ corresponding to the mass ratio of the smaller primaries, $\mu = 0.01215$ for the Earth and the Moon.

The system is constructed to be 2π periodic, which corresponds to the time period after which the primaries' configuration repeats (a synodic month for the Sun–Earth–Moon system). The origin is located at the Earth–Moon barycenter. A reference frame that rotates at a constant rate is selected along with a length normalization by $a_0(m) = m^{2/3}(1 - \frac{2}{3}m + O(m^2))$, the average distance between the smaller primaries along Hill's variation orbit. Consequently, the Earth and Moon move slightly in their reference frame. Note that this is simply a coordinate choice and does not effect the dynamics; equivalently, the Earth and Moon positions could be fixed as in Mohn & Kevorkian [1967].

A convenient aspect of the HR4BP is that it reduces to the Earth–Moon CR3BP when $m = 0$, and to the Sun–Earth Hill's problem when $\mu = 0$. Notably, there is a natural route to perform continuation from the autonomous limiting cases to the Sun–Earth–Moon HR4BP such that the model is coherent at every step. The connection between the CR3BP and HR4BP is clear when the equations of motion are formulated in an Earth–Moon frame. The connection between Hill's problem and the HR4BP is most apparent if we formulate the equations in a Sun–Earth frame. We will use the same origin, length, and time scaling as the Earth–Moon frame, and refer the reader to Scheeres [1998] for Hill's expansion of the Earth and Moon motion.

To define the Sun–Earth reference frame, let the x-axis point from the Sun to the Earth–Moon barycenter, and the z-axis point in the direction of the primaries' angular momentum. The y-axis

completes the right-handed frame. The Sun–Earth HR4BP equations of motion are

$$\begin{aligned} \ddot{x} - 2m\dot{y} &= U_x \\ \ddot{y} + 2m\dot{x} &= U_y \\ \ddot{z} &= U_z, \end{aligned}$$

which depend on the partial derivatives of the force potential-like function

$$U(\mathbf{r}, t; m, \mu) = \frac{1}{2}m^2(3x^2 - z^2) + \frac{m^2}{a_0(m)^3}\left(\frac{1-\mu}{r_1(\mathbf{r}, t; m, \mu)} + \frac{\mu}{r_2(\mathbf{r}, t; m, \mu)}\right). \tag{3.6}$$

The lengths r_1 and r_2 are the distances of the fourth body located at $\mathbf{r} := (x, y, z)$ to the Earth and Moon. When we set $\mu = 0$, the Earth is located at the origin, length $r_1 = \|\mathbf{r}\|$, and we recover Hill's problem up to a constant length and time scaling.

The HR4BP in a Sun–Earth frame has several symmetries. These are similar to Hill's problem except time plays an important role since it orients the primaries. If we define $t = 0$ to be the time when the Sun, Earth, and Moon are in a line, the symmetries can be represented as follows:

$$\begin{aligned} (x,\, y,\, z,\, v_x,\, v_y,\, v_z,\, t) &\mapsto (-x,\ \ y,\ \ z,\ \ v_x, -v_y, -v_z,\, \pi - t) \\ (x,\, y,\, z,\, v_x,\, v_y,\, v_z,\, t) &\mapsto (\ \ x, -y,\ \ z, -v_x,\ \ v_y, -v_z,\ \ -t) \\ (x,\, y,\, z,\, v_x,\, v_y,\, v_z,\, t) &\mapsto (\ \ x,\ \ y, -z,\ \ v_x,\ \ v_y, -v_z,\ \ +t) \end{aligned}$$

where (v_x, v_y, v_z) are the velocities associated with the coordinates (x, y, z). Additional solutions can be generated by composing the symmetries.

The Sun–Earth–Moon HR4BP is intended for studying the motion in the vicinity of the Sun–Earth L_1 and L_2 libration points and the region between them (including motion near the Earth and Moon and their libration points). When μ is nonzero, the influence of the Moon is included and the Sun–Earth equilibrium points located on the x-axis at $x = \pm 3^{-1/3}/a_0(m) = \pm 3.91$ become small 2π-periodic orbits serving as dynamical substitutes.

In general, the planar Lyapunov orbits become two-dimensional quasi-periodic tori with an internal frequency associated with their period in Hill's problem, and an external frequency associated

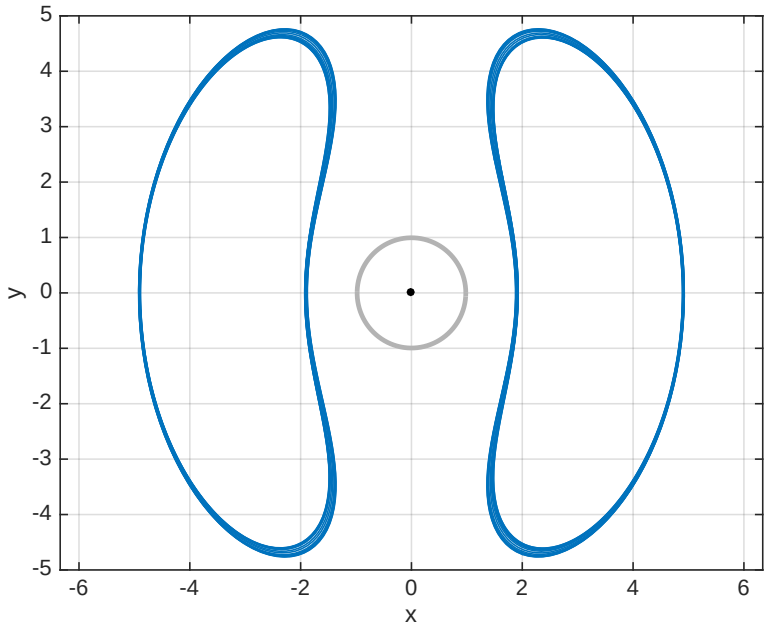

Figure 3.16: Sun–Earth L_1 and L_2 planar quasi-periodic orbits near 1:7 resonance with Moon

with the Moon's synodic period. Close to the Sun–Earth L_1 and L_2 libration points, the internal period is slightly less than 6 synodic months. As we continue along the planar orbit family, the period increases, and we cross a 1:6 resonance followed by 3:19, 2:13, and 3:20 resonances. Since the orbits near the libration point do not pass close to the Moon, the early resonances do not perturb the dynamics significantly. However, larger orbits pass nearer the Moon, and the family of quasi-periodic orbits appears to break down approaching the 1:7 resonance. One of the last computed orbits before the 1:7 resonance is shown in Figure 3.16. Due to symmetry, the L_1 and L_2 orbits are identical up to a rotation about the origin.

3.3.2 Motion near Earth–Moon collinear points

We now consider the HR4BP dynamics about the L_1 and L_2 libration points in an Earth–Moon frame (see [Scheeres, 1998] for the equations of motion). Unlike the Sun–Earth case where the Moon's influence increases as we move along the planar family of libration point orbits, the magnitude of the Sun's perturbation near the Earth–Moon libration points is approximately constant.

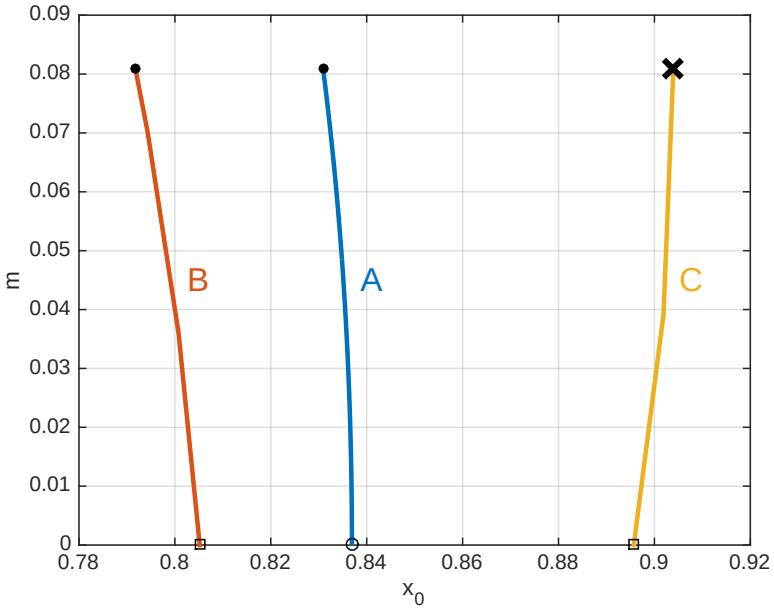

Figure 3.17: Bifurcation diagram of Earth–Moon L_1 dynamical substitute periodic orbits

3.3.2.1 Earth–Moon L_1 planar orbits

The first step in analyzing the planar vicinity of the Earth–Moon L_1 point in the HR4BP is to find a substitute for the libration point itself. We initialize the computation from the Earth–Moon L_1 point in the CR3BP ($m = 0$). For nonzero m, the equations of motion are 2π-periodic,[1] and the equilibrium point becomes a periodic orbit of the same period. If the orbit is continued until $m = 0.0808$, the dynamical equivalent including the Sun's perturbation is obtained. This continuation process is illustrated by branch A in Figure 3.17, where the orbit's x-component when $t \pmod{2\pi} = 0$, i.e., the Sun, Earth, and Moon are aligned, is shown as m is varied. The substitute has stability center $\times$ saddle.

The planar L_1 Lyapunov orbits in the Earth–Moon CR3BP begin with a period of about $T = 2.69$ and increase along the family. Within this family there is a periodic orbit of period π. If we continue this orbit to nonzero m, it splits into two orbits of period 2π, one with stability center $\times$ saddle and the other with stability saddle $\times$ saddle. The continuation of these orbits is shown by branches B and C, respectively, in Figure 3.17. While initial orbit is identical when $m = 0$,

[1] The Earth–Moon HR4BP equations of motion in fact have a minimal period π due to symmetry, but this is not essential for the discussion.

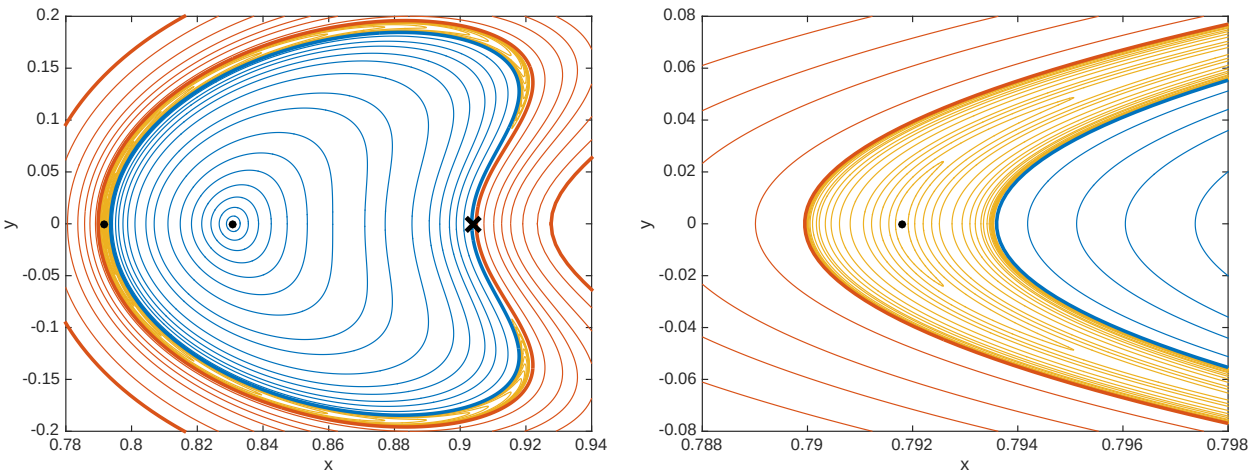

Figure 3.18: Stroboscopic map of Earth–Moon L_1 planar quasi-periodic orbits (expanded view of 2:1 resonance region on right)

their phasing differs by half a revolution, so the initial x-component in the figure is on either side of the CR3BP L_1 libration point.

We expect most of the planar periodic orbits in the Earth–Moon CR3BP to become two-dimensional tori in the HR4BP. One frequency $\omega_1 = 2\pi/T$ is associated with the period T that varies along the family of CR3BP planar Lyapunov orbits. The other frequency $\omega_2 = 1$ matches the periodic influence of the Sun. Starting from the L_1 dynamical substitute (branch A periodic orbit at $m = 0.0808$), we initialize a family of Sun–Earth–Moon two-dimensional tori along which the frequency ω_1 varies. The family is continued (with fixed m) until a dynamical boundary is reached. The family of tori is illustrated in Figure 3.18 using a stroboscopic map $t \,(\mathrm{mod}\, 2\pi) = 0$ and corresponds to the inner curves. Note that the axes are scaled independently to emphasize the detail.

The boundary is associated with the 2:1 resonance when $2\pi/\omega_0$ is half a synodic month. We can understand the structure in this resonance region by returning to the two additional periodic orbits we have computed. The orbit on branch B, which has an elliptic (center) component, has a small region of approximately resonant tori around it shown in Figure 3.18. This family is bounded on the planar center manifold by the stable and unstable manifolds of the hyperbolic (saddle) periodic orbit on branch C. These manifolds will not exactly coincide, so there will be a small region of chaos on the center manifold in its vicinity.

Finally, beyond the resonance we have more quasi-periodic orbits replacing the planar Lyapunov orbits with larger amplitude. These are the outer curves in Figure 3.18. The family is continued until a 5:3 resonance is reached at which there are more resonant "islands" that we do not currently compute. Note that by using a numerical approach we are able to extend the family beyond what can be conveniently obtained using center manifold reduction about the Earth–Moon L_1 point. This allows us to compute the 2:1 resonance, which may otherwise be outside the region of convergence of a semi-analytic method [Andreu, 1999].

3.3.2.2 Earth–Moon L_2 planar orbits

The situation for the Earth–Moon L_2 point differs in some significant ways from the L_1 case. Here the CR3BP planar Lyapunov orbits emanating from the libration point have a period T of about 3.37, which corresponds to a frequency ω_0 of about 1.86. However, this frequency crosses 2 as we perform continuation in m of the dynamical substitute.[2] The crossing leads to interesting bifurcation behavior of the L_2 dynamical substitute itself.

The bifurcation diagram of the 2π periodic orbit replacing the Earth–Moon L_2 point is shown in Figure 3.19. At first, it appears that there is a pitchfork-like bifurcation that occurs along branch A, which originates from the CR3BP equilibrium point. A close inspection, however, shows that the bifurcation is perturbed (at least when Hill's variational orbit is expanded to order m^6), and the branch only goes to the periodic orbit on the right. Thus, the closest dynamical substitute to the L_2 libration point does not belong to branch A. It belongs to branch B, which ends in another periodic orbit in the Sun–Earth–Moon HR4BP after passing a turning point in m. All three orbits have stability center $\times$ saddle. Near the turning point, branch B undergoes an additional bifurcation that gives rise to a periodic orbit family C that is symmetric across the x-axis (though the individual orbits themselves are not). This branch is most apparent on the right of Figure 3.19 where the periodic orbit coordinates (x, y) at time $t \pmod{2\pi} = 0$ are plotted as m varies. The two periodic

[2] As m varies, the dimensional time unit is scaled by $(1 + m)$. When $m = 0$ (Earth–Moon CR3BP), 2π time units corresponds to a sidereal month (27.32 days). When $m = 0.0808$ (Sun–Earth–Moon HR4BP), 2π time units is a synodic month (29.53 days). See [Scheeres, 1998] for more details.

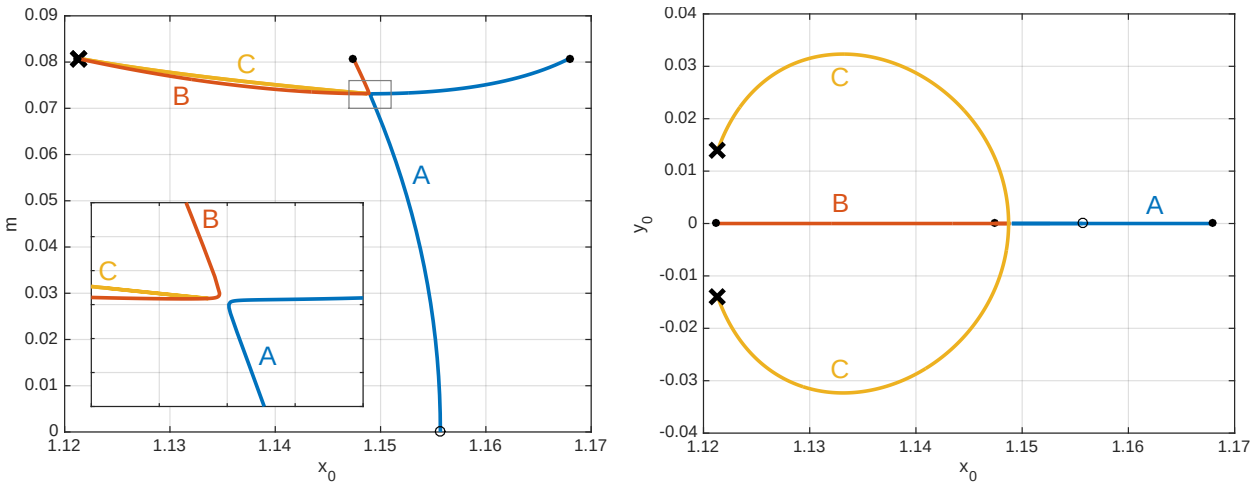

Figure 3.19: Bifurcation diagram of Earth–Moon L_2 dynamical substitute periodic orbits

orbits in the Sun–Earth–Moon HR4BP along branch C have stability saddle $\times$ saddle.

The bifurcation behavior of the Earth–Moon L_2 dynamical substitute may clarify the observations by Andreu in the (non-coherent) bicircular four-body problem. The substitute computed by direct continuation is a fairly large orbit. It may be possible that a periodic orbit similar to the middle HR4BP Earth–Moon L_2 dynamical substitute exists on a disconnected branch. The branches may not be as close to intersecting as in Figure 3.19 due to the lack of coherence.

The five periodic orbits obtained allow us to understand the geometry of the 2:1 resonance that is passed along the family of two-dimensional quasi-periodic orbits. As with the L_1 case, we initialize the family of tori near the middle dynamical substitute. This is shown in the inner region of Figure 3.20, which is a stroboscopic map $t \pmod{2\pi} = 0$ of the invariant tori. The continuation stops when we approach the 2:1 resonance, $\omega_0 \approx 2\omega_1$. Here we have small families of nearly resonant tori that emanate from the two elliptic periodic orbits on the center manifold. The ones on the left are particularly small. Beyond the resonance region, there are additional invariant tori that replace the larger Earth–Moon L_2 planar Lyapunov orbits. The inner, two resonant, and outer families of tori are all separated on the center manifold by the invariant manifolds of the two hyperbolic fixed points denoted by crosses. This structure appears to match that of the quasi-bicircular problem computed semi-analytically in Andreu [1999].

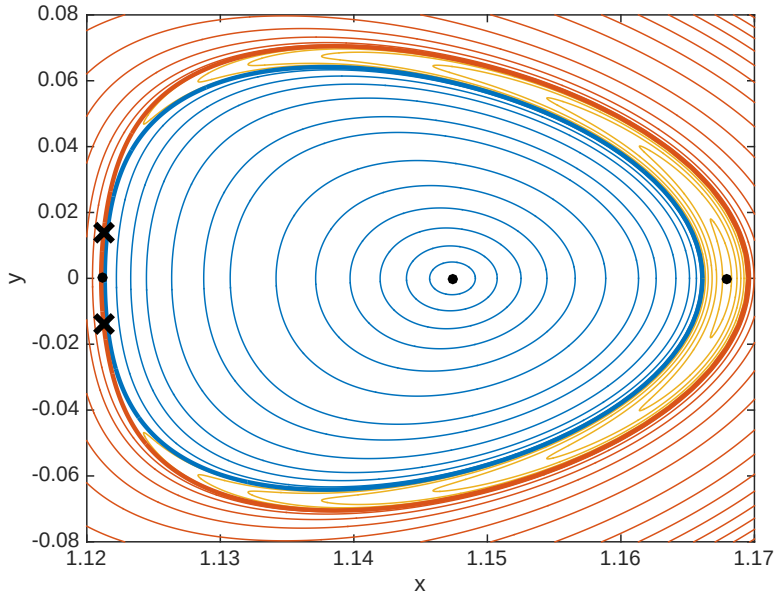

Figure 3.20: Stroboscopic map of Earth–Moon L_2 planar quasi-periodic orbits (including 2:1 resonance region)

CHAPTER 4

CONNECTIONS IN THE RESTRICTED THREE-BODY PROBLEM

Transport in the vicinity of the collinear libration points is organized by the invariant manifold structure. In the spatial CR3BP, the L_1 and L_2 libration points have two degrees of freedom associated with oscillatory motion, and one degree of freedom associated with hyperbolic motion. The four-dimensional center manifold of each libration point is filled with two-dimensional invariant tori, notably the Lissajous and quasi-halo orbits shown in Chapter 3. The associated five-dimensional center-stable and center-unstable manifolds contain trajectories that respectively approach and depart the invariant tori of the center manifold.

Intersections between the center-stable and center-unstable manifolds in the six-dimensional phase space correspond to families of trajectories that naturally connect invariant tori. For spacecraft orbiting a libration point, these trajectories allow the spacecraft to reach another orbit with nominally zero fuel cost. The connections can come in various forms. They can, for example, go between orbits of the L_1 and L_2 libration points (a heteroclinic connection), or depart and return to the center manifold of the same libration point (a homoclinic connection). Furthermore, they can travel between orbits of different types such as a departure from a Lissajous orbit and an arrival at a quasi-halo orbit. Recall, however, that the CR3BP dynamics mandate that the connected tori and the trajectory between them all lie at the same energy level.

Insight into the prevalence of connections can be obtained by considering dimension. The codimension of a manifold is the difference between the dimension of the space in which it resides (the phase space) and the dimension of the manifold. The codimension of a transverse intersection between two manifolds is the sum of their codimensions [Guckenheimer & Holmes, 2002]. The

center-stable and center-unstable manifolds of L_1 and L_2 in the CR3BP are codimension-1, so we expect their intersection to be codimension-2, or equivalently, a 4-dimensional manifold in the 6-dimensional phase space. This intersection manifold is filled with 1-dimensional trajectories, so there is a 3-parameter family of connecting trajectories. At a fixed energy level, this family has one dimension less, i.e., there is a 2-parameter family of connecting trajectories. In contrast, if we consider the planar CR3BP where the spacecraft moves in the plane of the primary bodies, connecting trajectories are generically isolated at a fixed energy level.

Recall that two-dimensional tori in the CR3BP lie in two-parameter families. Since the Hamiltonian is conserved, it is convenient to select one of these to be an energy parameter E. Then a value I can be assigned to each torus. This torus parameter serves a role similar to the pseudo-arclength for torus continuation in (2.1). Since we only compute a discrete set of tori with the approach described in Chapter 2, cubic interpolation is used to approximate intermediate tori. Alternatively, a Poincaré–Lindstedt expansion could be used. This expansion avoids the numerical computation of individual tori, but is only accurate in a limited region of the libration point or halo periodic orbit. States on each torus are parameterized using a pair of angles that we denote (u, v).

To provide each stable or unstable manifold trajectory a unique state for use as a boundary condition, we set a fixed distance from the corresponding torus in the stable or unstable direction. To improve the interpolation accuracy, we use a linear perturbation of size 10^{-6} in the Sun–Earth system and of size 10^{-5} in the Earth–Moon system (when the standard CR3BP normalization is used) and nonlinearly extend each perturbation to sizes 10^{-3} and 10^{-2}, respectively, by integrating the equations of motion. This procedure provides the boundary conditions $\mathbf{w}^s(u, v; I, E)$ on the center-stable manifold and $\mathbf{w}^u(u, v; I, E)$ on the center-unstable manifold that are stored in data sets for the L_1 and L_2 Lissajous and quasi-halo orbits. For the current analysis, we focus specifically on the "halves" of each manifold in the direction of the second primary body.

In this chapter, we present two methods for computing families of connections between quasi-periodic orbits in the spatial CR3BP. In Section 4.1 we present an indirect approach for computing connections where only one of the two boundary tori is known explicitly. We discuss how these

connections can be continued, and how the second boundary torus can be extracted. In Section 4.2 we consider the continuation of connections when both boundary tori are explicitly parameterized. We explore initialization of spatial families from the planar CR3BP, and explore a family of connections in the Sun–Earth system.

4.1 INDIRECT COMPUTATION

It can be shown that the center-stable manifold divides trajectories that leave the region of the second primary and pass to the interior or exterior regions [Conley, 1968; Gómez et al., 2004]. Thus, if a continuous family of trajectories has members that leave through the L_1 or L_2 gateway and some that do not, then one member lies directly on the center-stable manifold itself. The simplest application of this procedure is to use a binary search selecting the trajectory based on whether it escapes or not within some time interval. The main drawback is that the procedure lacks robustness.

For initial conditions on a periodic orbit, Calleja et al. [2012] makes this procedure more robust by taking advantage of Gauss–Legendre collocation and pseudo-arclength continuation. The stability of these tools is fundamental to this approach. Since we are able to compute quasi-periodic orbits and their stability, we can adapt this procedure to computing quasi-periodic-to-quasi-periodic connections, which are much more prevalent. Unlike Calleja et al., we compute the starting orbit and its stability ahead of time in a parameterized database rather computing the orbit and its stability at the same time as the connection.

We refer to the procedure as "indirect" since we only compute part of a trajectory lying on the destination torus. We explain in Section 4.1.2 how this trajectory can be used to extract the torus itself given sufficiently many windings.

4.1.1 Locating and continuing connection

The procedure starts by finding an initial condition $\mathbf{w}_0^u(u_0, v_0; I_0, E_0)$ on the center-unstable manifold of the departure libration point such that the corresponding trajectory transits the desired arrival libration point. We select a stopping surface such that the transit is ensured. For example, when

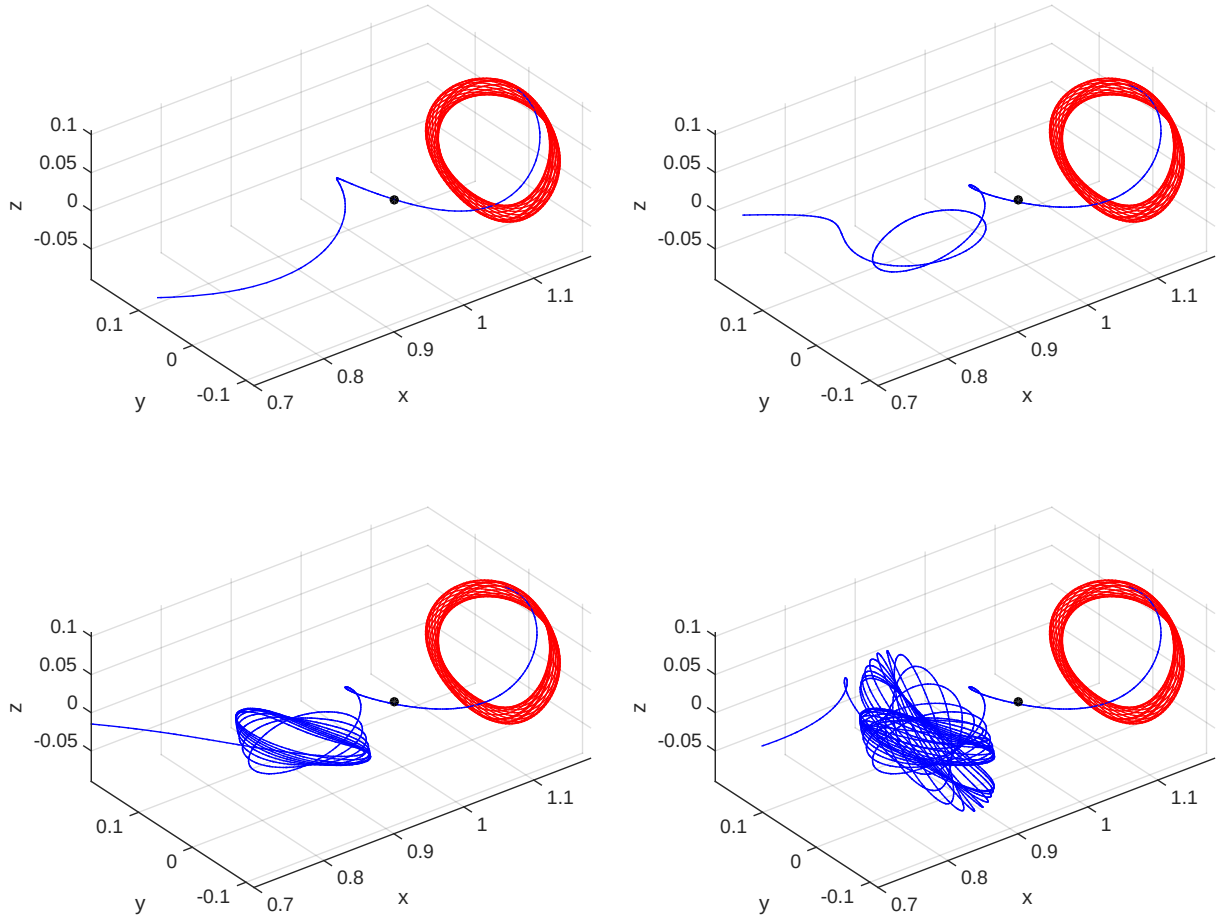

Figure 4.1: Steps 0, 200, 500, 1000 for locating first heteroclinic connection

finding a connection from the Earth–Moon L_2 vicinity to L_1 vicinity, if the trajectory has component $x = 0.7$ at time $T > 0$, then the transit of L_1 is guaranteed. The starting trajectory can be found by simply integrating a few initial conditions from $\mathbf{w}_0^u$ forward in time and checking whether or not the surface is crossed. Note that an identical procedure can be used for starting from the stable manifold $\mathbf{w}_0^s$ if we consider time $T < 0$. An example starting trajectory on the unstable manifold of an Earth–Moon L_2 quasi-halo torus that transits L_1 is shown in the first plot of Figure 4.1.

We now construct a boundary value problem for indirectly locating an initial connecting orbit. As with the torus computation, we parameterize the trajectory on the unit interval, $\tau \in [0, 1]$:

$$\frac{d\mathbf{x}}{d\tau}(\tau) = T\mathbf{f}(\mathbf{x}(\tau)), \tag{4.1a}$$

$$\mathbf{x}(0) = \mathbf{w}_0^u(u_0, v_0; I_0, E_0), \tag{4.1b}$$

$$g(\mathbf{x}(1)) = 0, \tag{4.1c}$$

$$\int_0^1 \left\langle \mathbf{x}(\tau) - \tilde{\mathbf{x}}(\tau),\, \tilde{\mathbf{x}}'(\tau) \right\rangle d\tau + \left\langle \mathbf{p} - \tilde{\mathbf{p}},\, \tilde{\mathbf{p}}' \right\rangle = \Delta s. \tag{4.1d}$$

We fix the initial torus (I_0, E_0) and let the free parameters $\mathbf{p} := (u_0, T)$ contain one of the two angles parameterizing the torus along with the time T to reach the final surface defined by (4.1c), for example, $g(\mathbf{x}(1)) := x(1) - 0.7 = 0$. It is often convenient for the free angle u_0 to be selected to correspond to the major angle around the torus, while minor angle v_0 is associated with the oscillatory motion about the base periodic orbit. The last constraint (4.1d) is used for pseudo-arclength continuation along the family of transit trajectories with tilde representing a neighboring solution in the family, and prime representing the approximate family tangent. As mentioned earlier, the stable manifold $\mathbf{w}_0^s$ could be used in place of $\mathbf{w}_0^u$ if $T < 0$.

The system of equations (4.1) provides a well-posed boundary value problem. We use a Newton method to solve the equations discretized via Gauss–Legendre collocation (Section 2.3.2). The corresponding Jacobian is a square matrix. The primary idea is that as we perform continuation of the transit trajectory, we approach the boundary between transit and non-transit orbits. By constraining each trajectory to be sufficiently close to the previous one, we get closer and closer to the heteroclinic connection that divides these orbits. Fundamental to this approach is the stability of the Gauss–Legendre collocation and constraint (4.1d) depending on the entire trajectory and not just the initial condition. Using single shooting, at most two revolutions of the destination torus can typically be obtained.

This procedure can fail in certain situations. Notably, if for all $u_0 \in \mathbb{S}$, the manifold trajectories transit the destination libration point, then a heteroclinic connection will not be found. Also, if the family of transit trajectories undergoes a tangency at the stopping surface $g(\mathbf{x}(1)) = 0$, then the continuation could fail. In practice, both of these situations appear to be uncommon. If such a situation arises, the choice of the free parameter can be changed.

To illustrate the procedure, we start from an Earth–Moon CR3BP quasi-halo torus. As a function of the step number, we plot the two free parameters: the angle u_0 and the time T that is

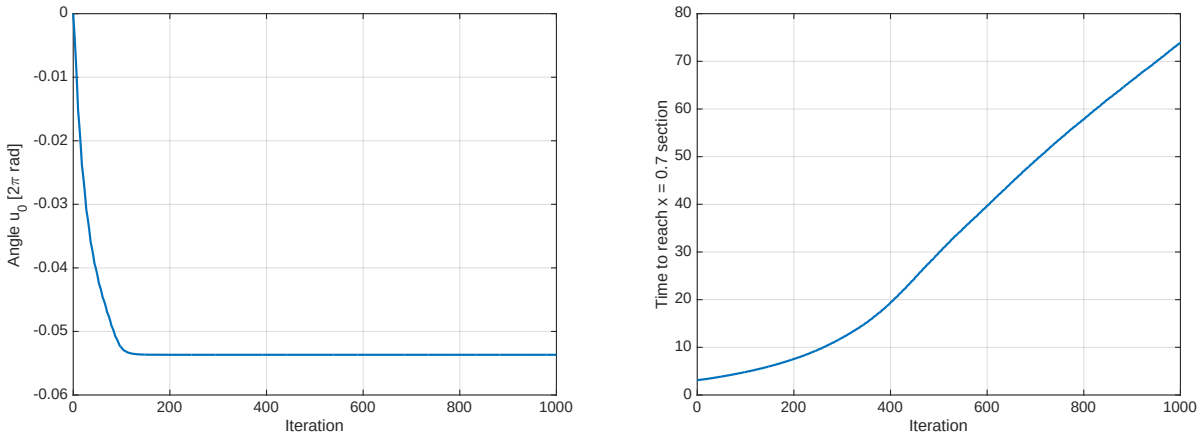

Figure 4.2: Parameters for locating first heteroclinic connection

required to reach the final surface. This is shown in Figure 4.2. We can see that u_0 converges to a fixed value. At each step, however, small changes in u_0 are sufficient for the time T to grow in an approximately linear manner after an initial transient phase. We plot steps 0, 200, 500, 1000 in Figure 4.1. It is apparent that we are converging to an L_1 Lissajous orbit. The initial L_2 quasi-halo orbit is shown in red to illustrate the behavior backwards in time, but the computation itself, starts from a point on the unstable manifold $\mathbf{w}_0^u$.

We have so far computed a connection from a set initial torus (I_0, E_0). In fact, we have only considered trajectories at a fixed v_0 value. Now let us fix T and have both angles as free parameters, $\mathbf{p} := (u_0, v_0)$. We still consider boundary value problem (4.1). Since T is fixed at some large value, the trajectory family will remain near the boundary between transit and non-transit trajectories, i.e., the center-stable manifold of the destination libration point.

We illustrate this one-parameter family of connections in Figure 4.3 where the final portion of the trajectory that intersects the stopping surface has been trimmed off. A particularly interesting result is that we pass through the boundary between the Lissajous and quasi-halo orbits within the single family. This is also apparent if we plot the crossings of the $z = 0$ plane (where $\dot{z} > 0$) as shown in Figure 4.4. We overlay the crossings with the L_1 center manifold section from Figure 3.13 at this energy level. It is apparent that the connections cover part of the Lissajous family (in blue) and the

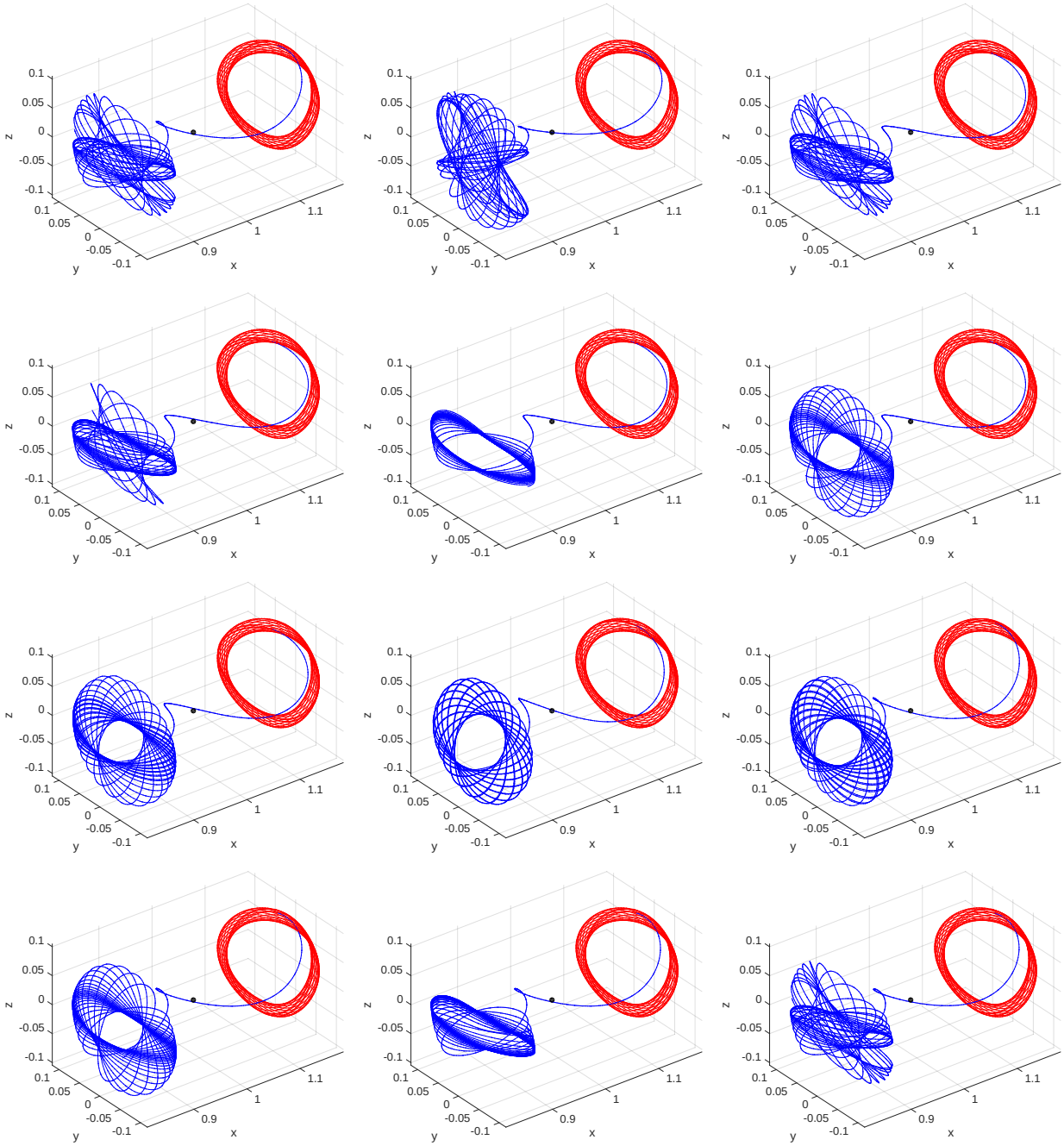

Figure 4.3: Earth–Moon L_2 to L_1 heteroclinic connection family from single L_2 quasihalo torus

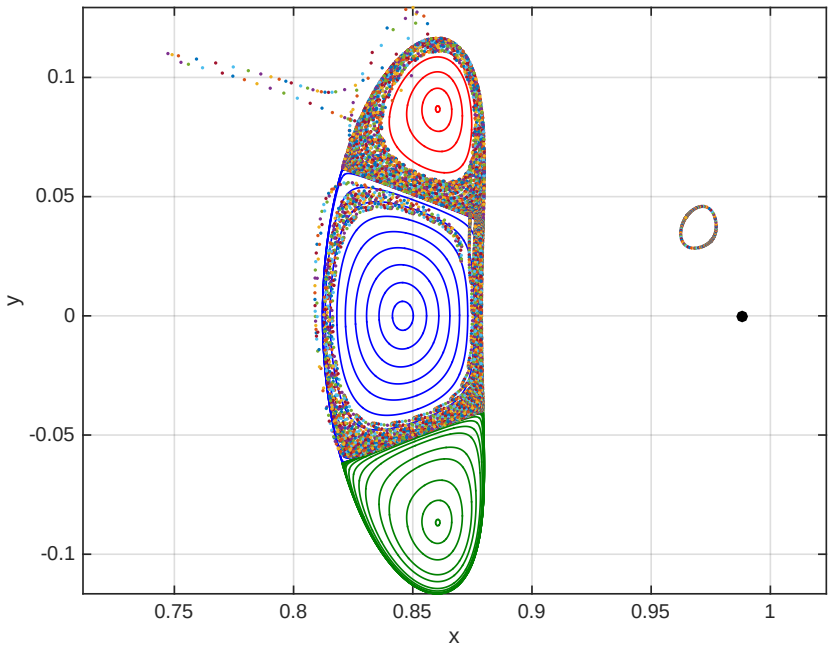

Figure 4.4: Crossings of $z = 0$ plane near L_1 for connection family from L_2 torus

southern quasi-halo family (in red). These connections, however, do not reach the L_1 vertical or halo periodic orbits.

It is important to note that all the connections originate from a single departure torus. If we also vary parameters (I_0, E_0), we can begin to explore the full three-parameter family of connecting orbits. Each torus can also have connections that belong to different families such as connection families that make additional passages by the Earth.

4.1.2 Extracting boundary condition torus

A drawback of the indirect computational approach is that we lack an explicit representation of the destination torus. Rather we obtain a trajectory that follows the flow around the torus for a finite interval of time before leaving its vicinity. With sufficiently many windings around the torus, however, we can obtain an approximation $(\mathbf{u}, T, \rho)$ of the torus itself. We use an interpolation method inspired by the work of Simó [1998]. This approximation can then be refined using the torus computation method from Chapter 2.

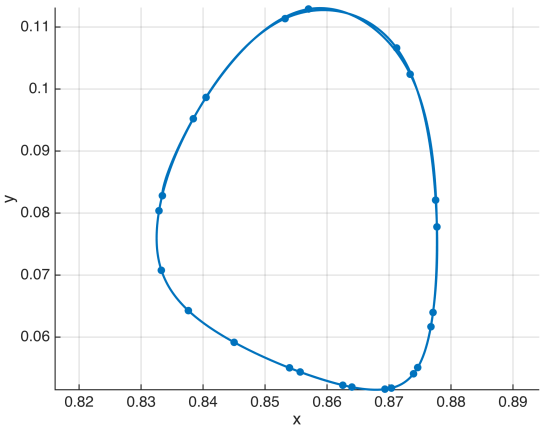

Figure 4.5: Interpolation of $z = 0$ plane crossings

The first step of the scheme is to reduce the trajectory to discrete iterates of a map. A simple choice is to consider intersections with the surface $z = 0$, $\dot{z} > 0$. Let $\mathbf{F}$ be the corresponding Poincaré map. Since we are only interested in the motion on the destination torus itself, we trim any beginning and ending iterates corresponding to the trajectory segments between the tori and departing to the stopping section. In actuality, none of the iterates will be exactly on the torus itself. With sufficiently many windings around the torus, however, the normal components in the stable and unstable directions will be negligibly small. For a connection to an L_1 southern quasi-halo orbit, the iterates are the dots shown in Figure 4.5 where the first 4 and last 4 iterates have been trimmed.

We denote each iterate $\mathbf{x}_i$ where $i \in \{0, 1, \ldots, N\}$. If the orbit is periodic and repeats after k iterations, then $\mathbf{F}(\mathbf{x}_0; k) \equiv \mathbf{F}^k(\mathbf{x}_0) = \mathbf{x}_0$. For a quasi-periodic orbit, the iterates never repeat but rather densely fill an invariant circle. Let $\bar{k}$ be some number of iterations such that a full revolution of the invariant circle is completed. If we view k as a continuous parameter, then for some noninteger $k^* \in (0, \bar{k})$, we can satisfy the condition $\mathbf{F}(\mathbf{x}_0; k^*) = \mathbf{x}_0$. We approximate the function's value at noninteger parameter values by evaluating a cubic spline through the iterates $\{\mathbf{x}_0, \ldots, \mathbf{x}_N\}$ over the integers $\{0, 1, \ldots, N\}$. This spline is the curve in Figure 4.5 passing through the sequence of dots. To compute k^* we find the argument that minimizes $\|\mathbf{F}(\mathbf{x}; k) - \mathbf{x}\|^2$. For the example orbit this function is shown in Figure 4.6, and the minimum is computed to be $k^* = 13.1926$. The corresponding

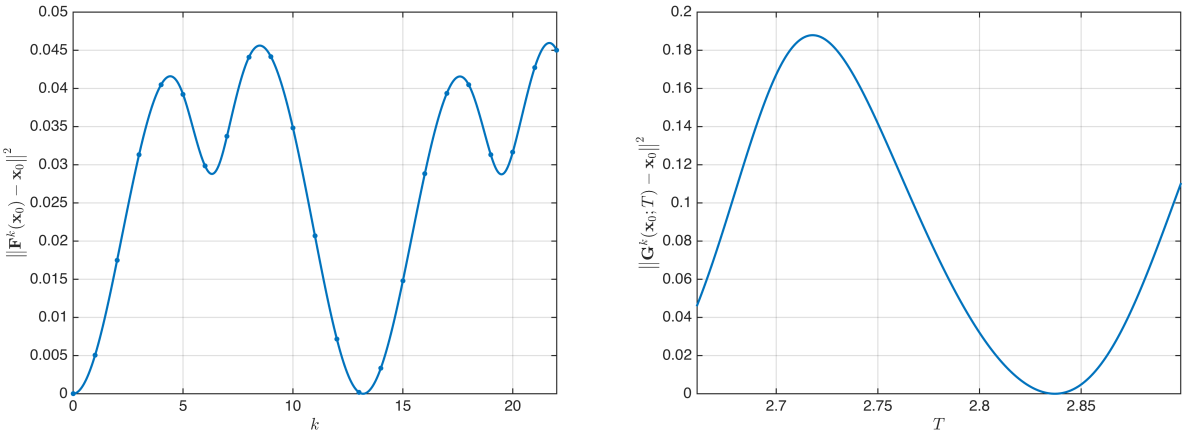

Figure 4.6: Minimization functions for computing k and T

rotation number is $1/k^* = 0.07580$. Since we can freely add any integer to this number, we find $\rho = 1.07580$.

For the destination torus, we have thus far computed an invariant circle of a Poincaré map (along with its rotation number). We would now like to find an equivalent invariant circle of a stroboscopic map. We define function $\mathbf{G}(\mathbf{x}_0; k, T) := \boldsymbol{\varphi}_T^k(\mathbf{x}_0)$, which gives the k-th iterate of the time-T map. This can be obtained by simply evaluating the continuous, piecewise polynomial representing the trajectory. For a given T, we can compute $\mathbf{G}(\mathbf{x}_0; k^*, T)$ in an analogous manner to the Poincaré map by constructing a cubic spline through values at integers k, and evaluating at k^*. Then the time giving an invariant circle is the solution to $\mathbf{G}(\mathbf{x}_0; k^*, T^*) = \mathbf{x}_0$, which we estimate by minimizing $\|\mathbf{G}(\mathbf{x}_0; k^*, T^*) = \mathbf{x}_0\|^2$. We bound the stroboscopic map time by the minimum and maximum times between crossings of the surface of section. For the example orbit, the function to minimize is in Figure 4.6. We find $T = 2.83708$. Combined with the rotation number, we can compute frequencies ω_1 and ω_2.

Finally, for the collocation method we need a set of trajectories evenly-spaced around the invariant circle. From the computed trajectory itself, we have a sequence of trajectory segments $\{\mathbf{x}_0(\cdot), \mathbf{x}_1(\cdot), \ldots\}$ parameterized over a sequence of integers $\{0, 1, \ldots\}$. Now we apply a cubic spline to the trajectories themselves and evaluate it at evenly-spaced points in the interval $[0, k^*]$. We now

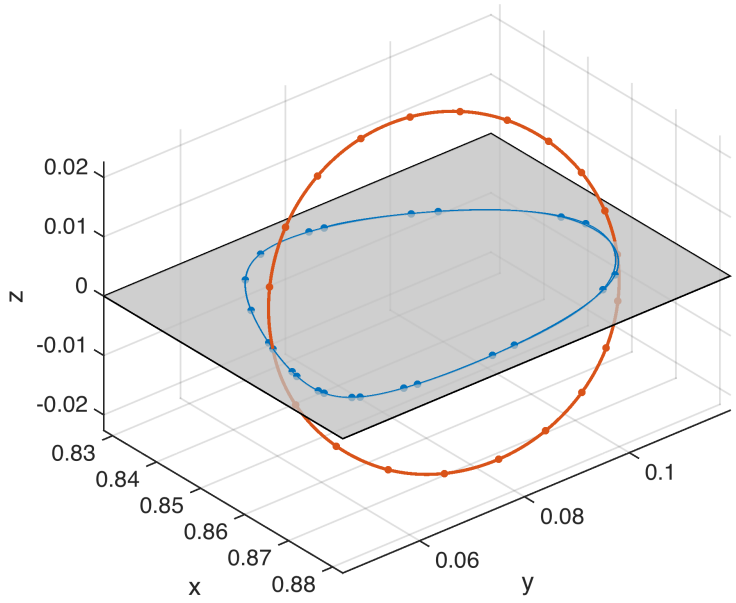

Figure 4.7: Invariant circles of section and stroboscopic map

have a complete initial guess that can be put into the torus computation scheme of Chapter 2. The corresponding point on the invariant circle are included in Figure 4.7. We are able to successfully converge to a torus keeping ρ and T fixed (and removing two constraints: the Hamiltonian value ($2.1\mathrm{d}_1$) and pseudo-arclength continuation ($2.1\mathrm{d}_2$)). This torus corresponds to the final boundary condition for this particular heteroclinic connection.

While this procedure is not guaranteed to always work, it appears to work well in practice. The primary requirement is to have enough crossings such that we have a "complete" circle. Close to a strong resonance, the procedure may also have difficulty.

4.2 DIRECT COMPUTATION

We now consider an approach where both the departure center-unstable manifold $\mathbf{w}_0^u$ and the arrival center-stable manifold $\mathbf{w}_1^s$ are explicitly used as boundary conditions. One advantage of this formulation is that we no longer need to compute the portion of the trajectory that winds around the arrival torus. Furthermore, since we know the motion on torus itself, we can automatically add

as many windings of each torus as desired. This is particularly useful when constructing chains of connections.

We will first formulate a boundary value problem for each connecting orbit at a fixed energy level. For the spatial CR3BP, this restriction corresponds to a two-parameter family of connections. Since the family is generated using continuation, a first connection must be provided. One option is to use the indirect approach from Section 4.1. An alternative that we present is to initialize the spatial connection family from a planar connection. We then apply this methodology to study the connection geometry between Sun–Earth Lissajous orbits.

4.2.1 BVP for connection family

We now introduce a boundary value problem for the direct computation of connecting trajectories at a fixed energy level. We constrain the beginning state to lie on the center-unstable manifold $\mathbf{w}_0^u$, and the ending state to lie on the center-stable manifold $\mathbf{w}_1^s$. The complete system of equations is as follows:

$$\frac{d\mathbf{x}}{d\tau}(\tau) = T\mathbf{f}(\mathbf{x}(\tau)) + \lambda \frac{\partial H}{\partial \mathbf{x}}^{\intercal}(\mathbf{x}(\tau)), \tag{4.2a}$$

$$\mathbf{x}(0) = \mathbf{w}_0^u(u_0, v_0; I_0, E_0), \tag{4.2b}$$

$$\mathbf{x}(1) = \mathbf{w}_1^s(u_1, v_1; I_1, E_1), \tag{4.2c}$$

$$h(\mathbf{p}) = 0, \tag{4.2d}$$

$$\int_0^1 \left\langle \mathbf{x}(\tau) - \tilde{\mathbf{x}}(\tau),\, \tilde{\mathbf{x}}'(\tau) \right\rangle d\tau + \left\langle \mathbf{p} - \tilde{\mathbf{p}},\, \tilde{\mathbf{p}}' \right\rangle = \Delta s. \tag{4.2e}$$

As usual, the connecting trajectory is parameterized on the unit interval, $\tau \in [0, 1]$. The boundary value problem is solved in discretized form using Gauss–Legendre collocation. Eight free parameters $\mathbf{p} := (I_0, u_0, v_0, I_1, u_1, v_1, T, \lambda)$ provide a well-posed system of equations and a square Jacobian matrix. The last two equations of (4.2) reduce the two-parameter family of connections to a single connection. First, the constraint $h(\mathbf{p}) = 0$, which is selected based on the connection geometry, reduces the family to a single parameter. For the Sun–Earth Lissajous connection family, we will

use $h(\mathbf{p}) = v_0 - \tilde{v}_0$ where $\tilde{v}_0$ is a fixed value. Second, pseudo-arclength continuation (4.2e) is used to select an individual connection along this branch.

The damping-like parameter λ warrants some discussion. We implicitly assume that the fixed parameters E_0 and E_1 provide boundary conditions at the same energy level. When the damping-like parameter λ is nonzero, the energy level changes monotonically; thus, a solution requires $\lambda = 0$ in theory. In practice, though, there is a small variation in the energy when the boundary conditions $\mathbf{w}_0^u$ and $\mathbf{w}_1^s$ are interpolated between the discrete set of computed tori. The parameter λ has a small magnitude to correct for this error and allows for the Newton method to fully converge to a solution. Alternatively, parameter λ could be removed, and either the initial energy parameter E_0 or the final energy parameter E_1 could be free.

4.2.2 Initializing family from planar connection

Continuing connections is a local problem. The solution to the boundary value problem (4.2) provides a connection that is some small distance Δs from a neighboring connection, and the continuation process is then repeated. Finding a first connection, however, is a global problem. One method to find a spatial connection for starting the direct computation procedure is described in Section 4.1. An alternative is to start from a planar connection between periodic orbits.

Planar connections are easier to find since they lie in a four-dimensional space (rather than a six-dimensional space). The challenge is that they are degenerate in the sense that out-of-plane angles v_0 and v_1 do not play a role. The boundary conditions are planar Lyapunov periodic orbits that only depend on the in-plane angles u_0 and u_1. However, by considering the spatial linearization about this planar connection, nearby spatial connections can be found. We start by linearizing the boundary conditions, specifically that the initial state should belong to $\mathbf{w}_0^u$ and the final state should belong to $\mathbf{w}_1^s$:

$$\mathbf{\Phi}_{6\times 6}\left(\frac{\partial \mathbf{w}_0^u}{\partial I_0}\Delta I_0 + \frac{\partial \mathbf{w}_0^u}{\partial u_0}\Delta u_0\right) + \mathbf{\Psi}_{6\times 2}\begin{bmatrix}\Delta T \\ \Delta\lambda\end{bmatrix} = \frac{\partial \mathbf{w}_1^s}{\partial I_1}\Delta I_1 + \frac{\partial \mathbf{w}_1^s}{\partial u_1}\Delta u_1 \tag{4.3}$$

Changes in the initial state and changes in the parameters are mapped to the final state using the matrices $\mathbf{\Phi}$ and $\mathbf{\Psi}$. A key characteristic is that while the boundary conditions do not depend on

v_0 and v_1, the partial derivatives with respect to the amplitudes I_0 and I_1 are a function of the out-of-plane angles:

$$\frac{\partial \mathbf{w}_0^u}{\partial I_0}(v_0) = \mathbf{v}_{0,c}\cos v_0 + \mathbf{v}_{0,s}\sin v_0 \tag{4.4}$$

$$\frac{\partial \mathbf{w}_1^s}{\partial I_1}(v_1) = \mathbf{v}_{1,c}\cos v_1 + \mathbf{v}_{1,s}\sin v_1 \tag{4.5}$$

where vectors $\mathbf{v}_{0,c}, \mathbf{v}_{0,s}, \mathbf{v}_{1,c}, \mathbf{v}_{1,s}$ are 6-dimensional vectors. This allows us to construct a 6×8 matrix $\mathbf{A}$ such that (4.3) is expressed as

$$\mathbf{A}_{6\times 8} \begin{bmatrix} \Delta I^0 \cos v^0 \\ \Delta I^0 \sin v^0 \\ \Delta u^0 \\ \Delta I^1 \cos v^1 \\ \Delta I^1 \sin v^1 \\ \Delta u^1 \\ \Delta T \\ \Delta \lambda \end{bmatrix} = \mathbf{0}_{6\times 1}. \tag{4.6}$$

The two-dimensional null space of $\mathbf{A}$ corresponds to the two tangent vectors of the two-parameter family of spatial heteroclinic connections. By perturbing in some combination of these directions, we can find spatial connections in the vicinity of a planar one.

4.2.3 Geometry of Sun–Earth connection family

To illustrate the computational procedure, we now consider a family of connections between Sun–Earth L_2 and L_1 Lissajous orbits. We constrain ourself to connections at Hamiltonian value $H = -1.500441436$. This level of energy is selected since it contains a Lissajous orbit at each libration point with y- and z-amplitudes $A_y \approx A_z \approx 200,000$ km. Arona & Masdemont [2007] study a similar family of connections in Hill's problem. In that work, the Lissajous orbits are obtained from a Poincaré–Lindstedt expansion, and connections are found using a surface of section.

There are two planar connections at this energy level that make two revolutions of the Earth en route to L_1 from L_2 (Figure 4.8). Additional heteroclinic connections between these planar Lyapunov orbits require additional revolutions of the Earth and thus have longer transfer times.

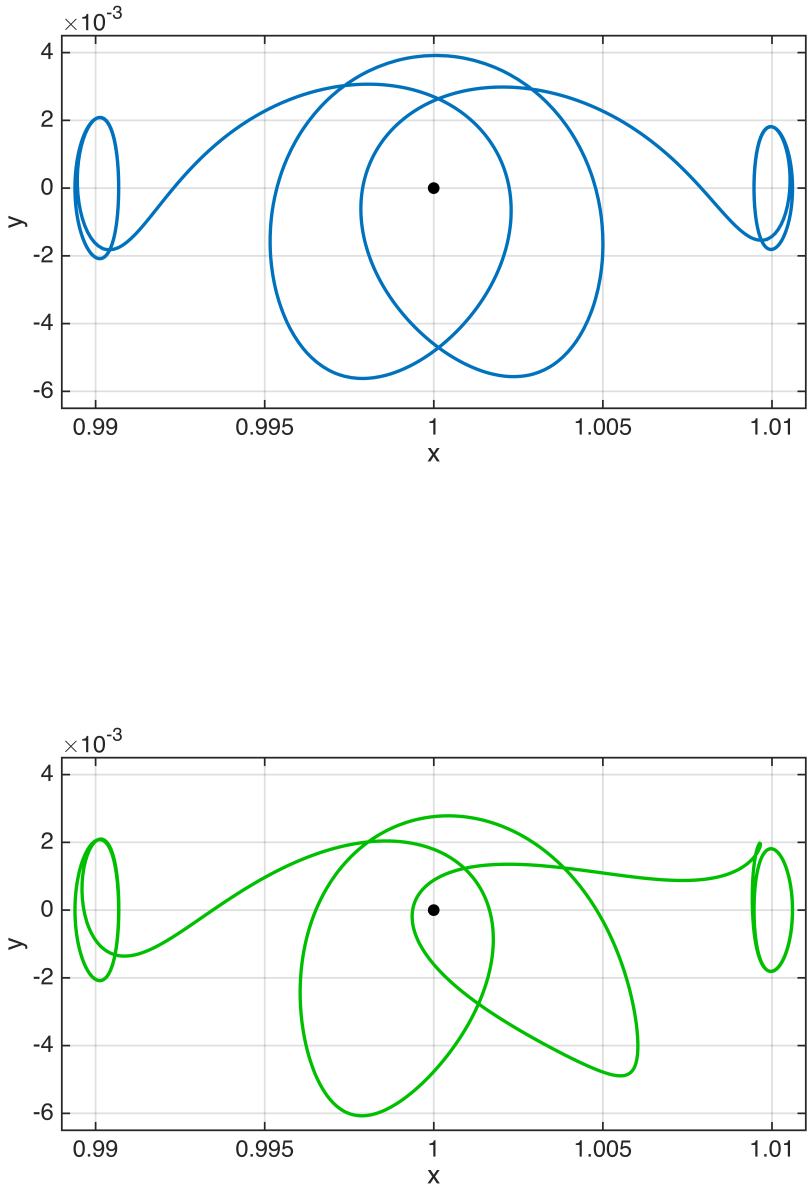

Figure 4.8: Planar Sun–Earth L_2 to L_1 heteroclinic connections

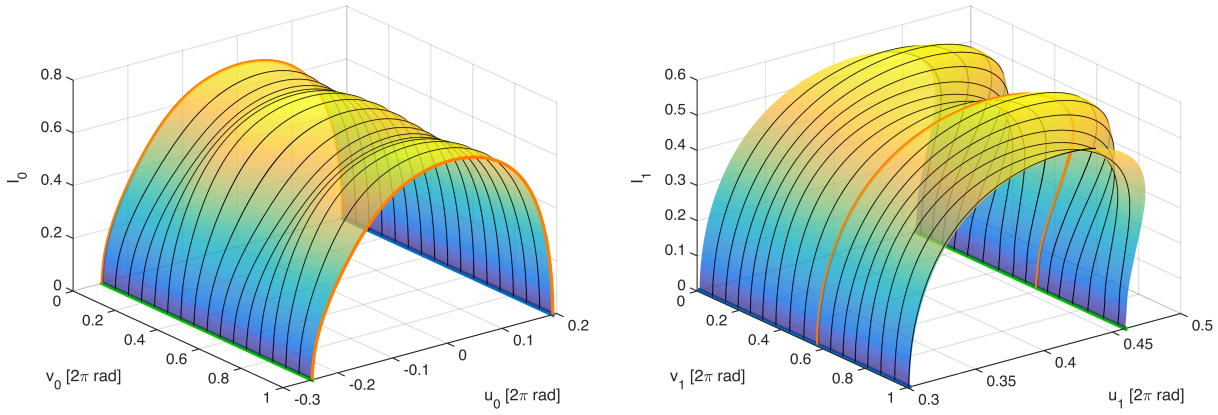

Figure 4.9: Spatial connection family initial conditions at L_2 and final conditions at L_1

These connections are found using a simple binary search to locate the boundary between transit and non-transit trajectories. Note that the boundary conditions are easy to represent since at this energy level there is a single planar torus at each libration point, namely a planar Lyapunov orbit. This solves the "global" part of finding the heteroclinic connection family.

Starting from the first planar connection, we linearize to find neighboring spatial connections using the approach of Section 4.2.2. We now perform one-parameter continuation of the connections solving boundary value problem 4.2. Since there is a two-parameter family of heteroclinic connections at a fixed energy level, along each branch we fix angle $v_0 = \tilde{v}_0$, and compute a sequence of branches for a discrete set of values $\tilde{v}_0 \in \mathbb{S}^1$.

The amplitude-like parameter I_i $(i = 0, 1)$ parameterizes the one-parameter family of tori at each boundary. It is defined such that $I_i = 0$ corresponds to the planar Lyapunov periodic orbit, $I_i = 1$ corresponds to the vertical Lyapunov periodic orbit, and $I_i \in (0, 1)$ corresponds to the two-dimensional Lissajous tori between them. Angle u_i corresponds to the planar motion, and angle v_i corresponds to the out-of-plane motion.

Each branch is shown as a thin black line in Figure 4.9. We plot the three parameters (u_0, v_0, I_0) that uniquely define the initial conditions $\mathbf{w}_0^u(u_0, v_0; I_0, E_0)$ for a fixed E_0 corresponding to the energy level. Similarly, we also plot the three parameters (u_1, v_1, I_1) that uniquely define

the final conditions $\mathbf{w}_1^s(u_1, v_1; I_1, E_1)$ for a fixed E_1. Each point on the initial condition surface represents a single connection that is mapped to a corresponding point on the final condition surface. A sample spatial heteroclinic connection within this two-parameter family is shown in Figure 4.10. The connection goes from a Sun–Earth L_1 Lissajous orbit to an L_2 Lissajous orbit. An interesting characteristic of the connection family is that each continuation branch starts from $I_0 = I_1 = 0$ and ends at $I_0 = I_1 = 0$ but with a different u_0 value. These two connections are precisely the two planar connections shown in Figure 4.8.

The two-dimensional torus family is degenerate when $I_i = 0$, specifically, the corresponding torus is one-dimensional, the planar Lyapunov orbit. In this case, the out-of-plane angle v_i does not affect the boundary state. To emphasize this geometric structure, we plot the initial and final conditions from Figure 4.9 in terms of coordinates $(u_0, I_0 \cos v_0, I_0 \sin v_0)$ and $(u_1, I_1 \cos v_1, I_1 \sin v_1)$ in Figure 4.11. From this it is apparent that that the connection family has the structure $\mathbb{S}^2 \times \mathbb{R}$. If we reduce each trajectory to its boundary conditions shown in Figure 4.11, then we have the structure of a 2-sphere. The two "poles" of each sphere correspond to the two planar heteroclinic connections.

We also plot the "amplitudes" I_0 and I_1 of the boundary condition tori along with the "transfer time" T from the initial conditions to the final conditions in Figure 4.12. It is apparent that the connections roughly "preserve" the amplitude of the boundary condition tori. In other words, if we start from a Sun–Earth L_2 Lissajous orbit with a certain out-of-plane amplitude, we tend to arrive at a Sun–Earth L_1 Lissajous orbit with a similar out-of-plane amplitude.

Other connection families can be explored in a similar manner. For example, we can also compute connections in the return direction from L_1 to L_2. This allows us to begin to consider chains of connections. The ending amplitude I_1 for a first leg from L_2 to L_1 will then be the starting amplitude I_0 for a second leg from L_1 to L_2. Depending on the number of revolutions we make about the intermediate Lissajous at L_1 we can relate the ending angles (u_1, v_1) of the first leg to starting angles (u_0, v_0) of the second leg. Computation of example non-planar chains of heteroclinic connections is ongoing work.

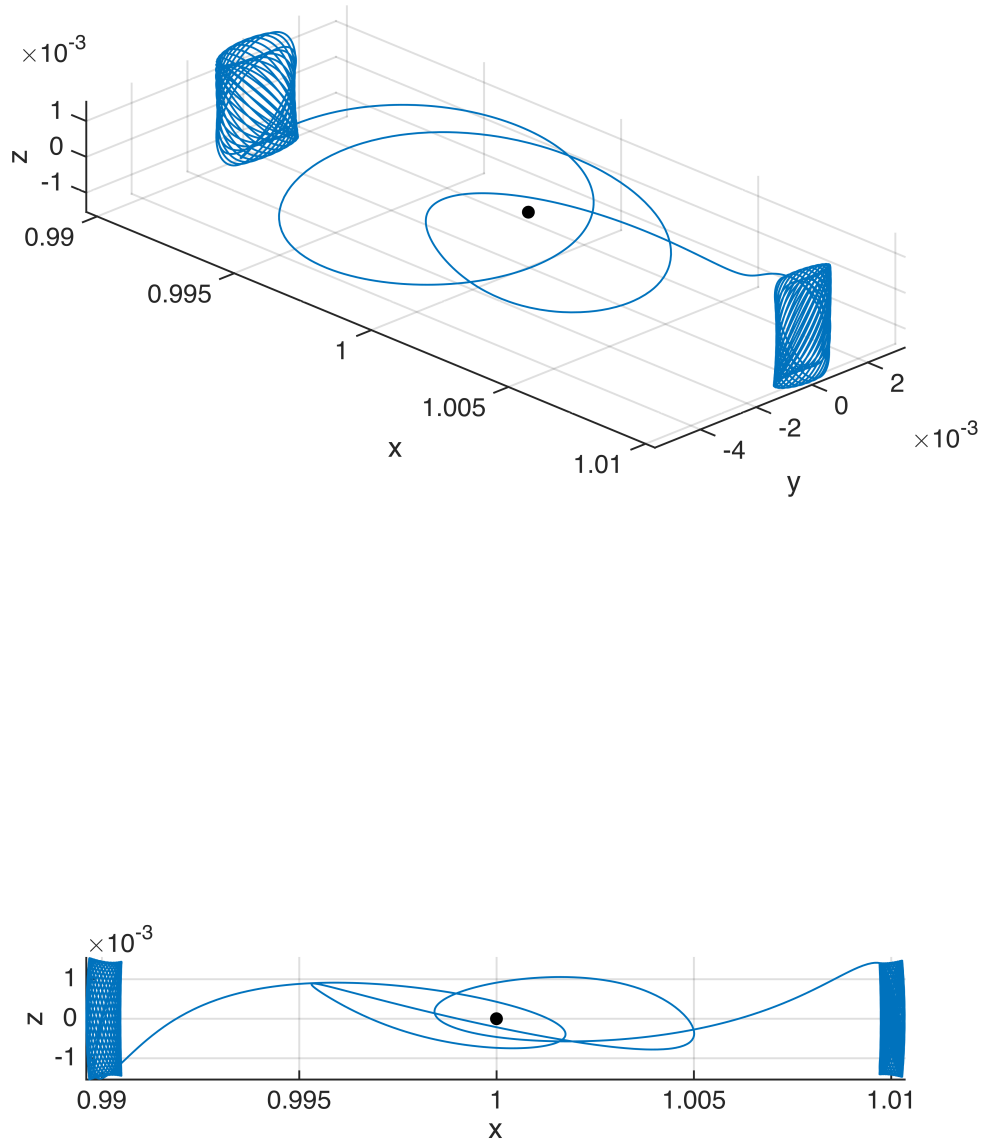

Figure 4.10: Sample connection from Sun–Earth L_2 Lissajous to L_1 Lissajous

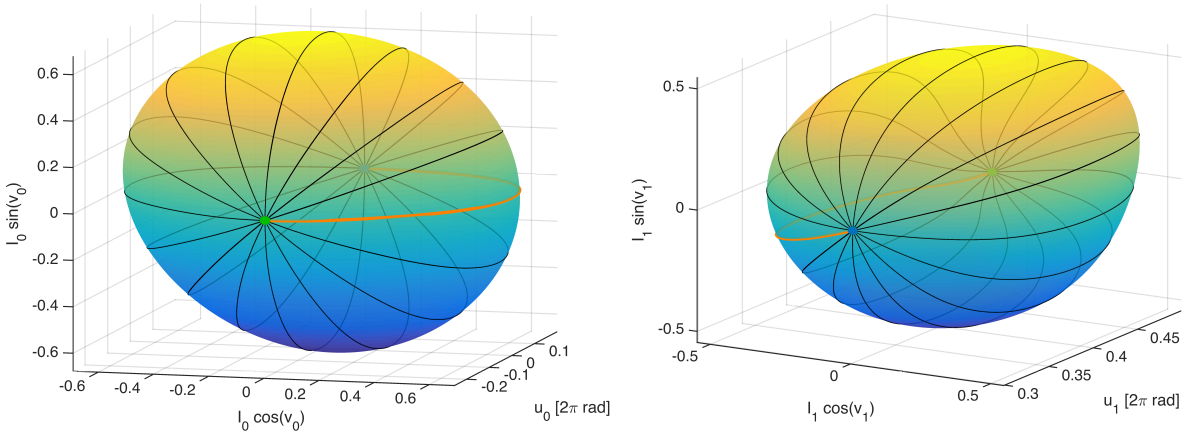

Figure 4.11: Initial and final condition 2-sphere topology

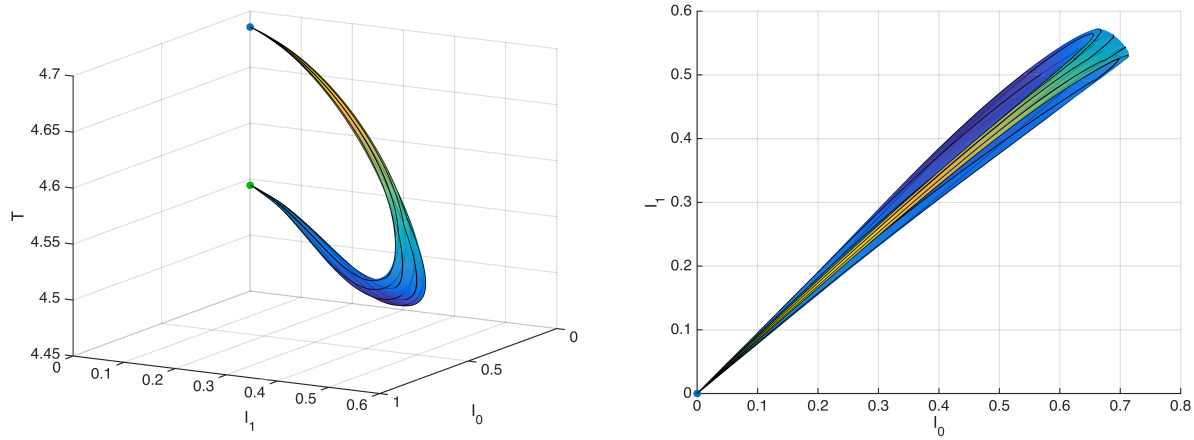

Figure 4.12: Boundary condition amplitudes and transfer time

CHAPTER 5

TRANSITIONING TO SOLAR SYSTEM

Simplified models such as the circular restricted three-body problem allow a mission designer to concentrate on the most relevant aspects of the dynamics. The dynamical structures such as invariant tori are interesting places for spacecraft. Their associated stable and unstable manifolds can be used for transfers. Using the methods presented thus far, it is possible to compute invariant tori in Hamiltonian systems.

The solar system itself is more complicated. A spacecraft is perturbed by the various planets, minor planets, and small bodies. One approach would be to include each of these bodies as a periodic forcing into our system. The dimension of the torus would go up by one for each body that is added, however, and the computation soon becomes intractable. Perhaps even more importantly, this does not allow us to use the exact positions of the perturbing bodies but rather some periodic (or quasi-periodic) approximation of their motion. Furthermore, non-conservative perturbations, even if small, would destroy the tori in general.

An alternative approach is to include all the available forces, and look for a similar trajectory to that obtained in the simplified model. In effect, we are no longer looking for an invariant object (which no longer exists), but instead looking for a "shadow" of it. In this chapter we use an ephemeris model that includes the precise positions of solar system bodies. We first generate a prediction of the original trajectory relative to the true positions of the primary bodies (this discussion follows Olikara et al. [2015]). Then we set up a minimization problem to find a nearby trajectory that matches the dynamics in the ephemeris model. We are still able to use the Gauss–Legendre collocation tool that we have developed. We present some sample orbits to illustrate the procedure.

5.1 EPHEMERIS MODEL

High-fidelity simulations produce ephemeris data sets containing the positions of solar system bodies (such as the Sun, planets, and moons) over an interval of time. Interpolating the ephemeris data, one can obtain accurate locations of the bodies at arbitrary times within the interval. This allows us to accurately model the (point-wise) gravitational forces on a spacecraft. The model is a restricted $(N+1)$-body problem where we assume the spacecraft's mass M_0 is negligible with respect to the masses $M_1, M_2, \ldots, M_N$ of the solar system bodies.

The equations of motion are formulated in an inertial frame and describe the evolution of the spacecraft's position vector $\mathbf{Q}(t)$ relative to the first body. From the ephemeris, we obtain the positions $\mathbf{R}_i(t)$ of the additional bodies $(i = 2, \ldots, N)$ relative to the first. Defining $\mathbf{Q}_i(t) := \mathbf{Q}(t) - \mathbf{R}_i(t)$ as the position of the spacecraft relative to each of these bodies, the spacecraft's dynamics are governed by the second-order differential equation

$$\ddot{\mathbf{Q}} = -GM_1 \frac{\mathbf{Q}}{\|\mathbf{Q}\|^3} - \sum_{i=2}^{N} GM_i \left(\frac{\mathbf{Q}_i(t)}{\|\mathbf{Q}_i(t)\|^3} + \frac{\mathbf{R}_i(t)}{\|\mathbf{R}_i(t)\|^3} \right) \tag{5.1}$$

where G is the gravitational constant. Note that this equation models each of the bodies as a point mass. It could be modified to include non-uniformities in the gravity field of one or more of the bodies. Additional perturbations on the spacecraft such as solar radiation pressure could also be incorporated.

5.1.1 Prediction transformation

Let the first body having mass M_1 be the larger primary of the restricted three-body problem. We seek to obtain an approximate ephemeris model trajectory $\mathbf{Q}(\cdot)$ that corresponds to the CR3BP trajectory $\mathbf{q}(\cdot)$. The equations of motion, however, differ in some notable ways. First, the spacecraft's state is no longer defined in a barycentric rotating frame of reference but rather in a primary-centered inertial frame. Second, the coordinates are scaled differently. Third, the ephemeris equations of motion are time dependent, so the transformation is dependent on the choice of epoch (the reference time).

We begin by viewing the independent variable in the CR3BP as the true anomaly of the smaller primary body in its orbit about the larger primary body. This corresponds to the typical choice of independent variable in the ER3BP, and it is equivalent to the nondimensional time in the CR3BP. Alternatively, the mean or eccentric anomaly could be used. For each physical time t starting at a specified epoch, we determine the corresponding (averaged) true anomaly f of the primary bodies. This allows us to reparameterize the CR3BP trajectory in terms of the physical time. The dimensional position vector $\mathbf{Q}(t)$ in a primary-centered inertial frame is then related to the non-dimensional position vector $\mathbf{q}(f)$ in a barycentric rotating frame using a transformation of the form

$$\mathbf{Q}(t) = \mathbf{C}(t)R(t)(\mathbf{r}(f(t)) + \mu\hat{\mathbf{x}}). \tag{5.2}$$

The term $+\mu\hat{\mathbf{x}}$ shifts the origin to the larger primary. The scaling factor $R(t) := \|\mathbf{R}(t)\|$ dimensionalizes the length using the ephemeris vector $\mathbf{R}(t)$ pointing from the larger to the smaller primary. The rotation matrix $\mathbf{C}(t)$ converts the position vector from the rotating frame to the inertial frame. Note that the rotating frame is oriented such that the x-axis is aligned with $\mathbf{R}(t)$, the z-axis is aligned with angular momentum $\mathbf{R}(t) \times \dot{\mathbf{R}}(t)$, and the y-axis is selected orthogonal to both such that the reference frame is right-handed. The inertial velocity $\dot{\mathbf{Q}}(t)$ is computed from the derivative of (5.2) using the product and chain rules. Applying the process in reverse, one can transform back into non-dimensional rotating frame states. This is useful for representing the ephemeris solutions in a familiar rotating reference frame.

For the Sun–Earth CR3BP, the smaller primary typically combines the mass of both the Earth and the Moon at their barycenter. For this case, some special consideration is needed for transforming to the ephemeris model. The vector $\mathbf{R}(t)$ points from the Sun to the Earth–Moon barycenter rather than to the Earth itself. For the Earth–Moon CR3BP, $\mathbf{R}(t)$ points directly from the Earth to the Moon.

5.1.2 Correction minimization

Transforming solely the initial state of a libration point orbit from the CR3BP to the ephemeris model and then propagating forward in time, a trajectory will quickly leave the vicinity of the libration point. However, by looking at a collection of transformed states on the trajectory, they can all be adjusted slightly such that the ephemeris dynamics (5.1) are satisfied while still maintaining the qualitative structure of the original orbit in the CR3BP.

Let the initial guess of the trajectory from the previous section be $\tilde{\mathbf{X}}(\cdot) : [t_0, t_f] \to \mathbb{R}^6$, which takes a time t and maps it to a position and velocity $(\tilde{\mathbf{Q}}, \dot{\tilde{\mathbf{Q}}})$. We would like to find a nearby trajectory $\mathbf{X}(\cdot)$ satisfying

$$\frac{d\mathbf{X}}{dt} = \mathbf{F}(\mathbf{X}, t) \tag{5.3}$$

for all $t \in [t_0, t_f]$ where $\mathbf{F}$ represents the non-autonomous ephemeris equations of motion (5.1) expressed as a first-order differential equation. We define the "closest" trajectory as the $\mathbf{X}(\cdot)$ minimizing the function

$$J = \frac{1}{2} \int_{t_0}^{t_f} \left\| \mathbf{X}(t) - \tilde{\mathbf{X}}(t) \right\|^2 dt \tag{5.4}$$

subject to the equations of motion (5.3).

The function J is minimized over the space of functions mapping $[t_0, t_f] \to \mathbb{R}^6$, which is infinite dimensional. We can, however, discretize it in the same manner as used for computing tori in Chapter 2 and connections in Chapter 4. We represent the trajectory as a continuous, piecewise polynomial. The minimization function J is evaluated via quadrature, and we use Gauss–Legendre collocation to enforce the vector field at the collocation points (Section 2.3.2).

This turns the search for the closest trajectory $\mathbf{X}(\cdot)$ into a finite-dimensional nonlinear programming problem with equality constraints. Common tools of solving these problems include SNOPT (Sparse Nonlinear Optimizer), which uses a sequential quadratic programming algorithm, and IPOPT (Interior Point Optimizer), which uses an interior point algorithm. IPOPT is used in this work. As an initial guess we use $\tilde{\mathbf{X}}(\cdot)$, which minimizes J but violates the vector field equality constraints. The Jacobian of the equality constraints can be generated using the same code as for

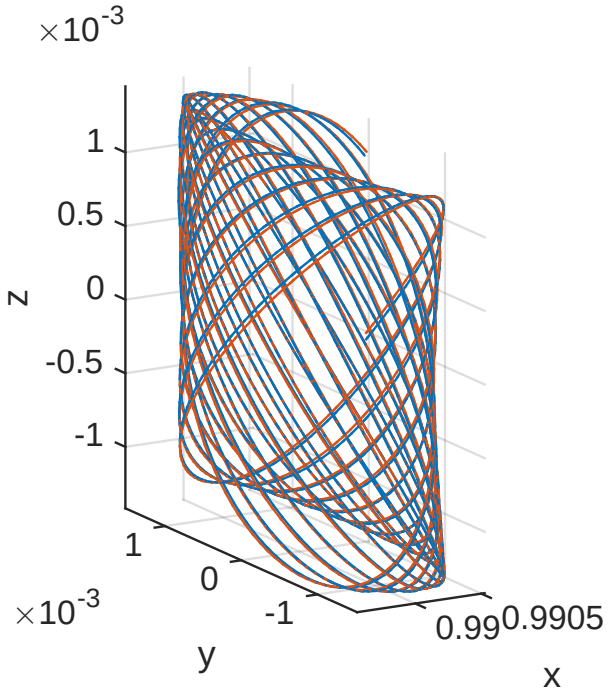

Figure 5.1: Sun–Earth L_1 Lissajous ephemeris orbit

solving boundary-value problems. Since there are only limited associations between the constraints and variables, it is important to take advantage of the sparse structure. We directly provide the solver with the indices of the nonzero elements in the equality constraint Jacobian and the corresponding values. This can greatly reduce memory and computational requirements.

5.2 SAMPLE ORBITS

We demonstrate the procedure using some sample Earth–Moon and Sun–Earth libration point orbits. We use the NASA Jet Propulsion Laboratory's DE422 ephemeris, and for all computations use $N = 10$ bodies: the Sun, the 8 planets, and the Moon. An arbitrarily selected epoch of 12:00 Mountain Standard Time on January 1, 2015 is used for this preliminary study.

In Figure 5.1 we plot 20 revolutions around a Sun–Earth L_1 Lissajous orbit. The trajectory in orange is the reference trajectory from the CR3BP model, and the trajectory in blue is the output from the optimizer in the ephemeris model. In order to compare the trajectories in a familiar frame, the ephemeris trajectory is transformed back to the Sun–Earth rotating frame even though the

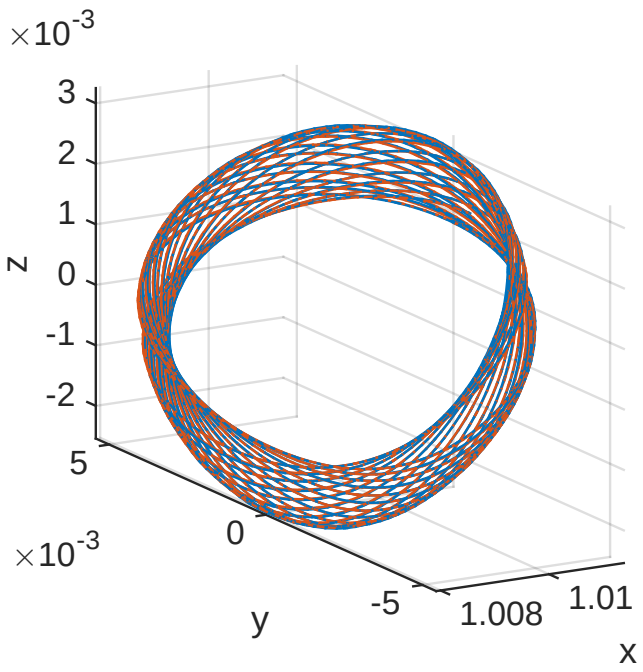

Figure 5.2: Sun–Earth L_2 quasihalo ephemeris orbit

computation is performed in an inertial frame. In Figure 5.2, 20 revolutions around a Sun–Earth L_2 quasi-halo orbit are shown. For both of these examples, it is apparent that the CR3BP geometry persists in the higher-fidelity model.

We also transition two Earth–Moon L_2 to L_1 heteroclinic connections belonging to the family computed in the previous chapter (Figure 4.3). The connection in Figure 5.3 ends at an L_1 Lissajous orbit, and the connection in Figure 5.4 ends at an L_1 quasi-halo orbit. Both ephemeris connections preserve the qualitative structure of the CR3BP connections. It is worth noting, however, that in both cases the ephemeris connection appears to originate from a slightly larger L_2 quasi-halo orbit than in the CR3BP model.

These examples illustrate that an optimization scheme can be an effective tool for transitioning trajectories to an ephemeris model. In the vicinity of the libration points, a nearby trajectory can very often be found. Transitioning a trajectory that passes near one of the primary bodies can be more difficult. In particular, the approach as presented is not able to move the Sun–Earth L_2 to L_1 Lissajous connection computed in the previous chapter (Figure 4.10) most likely due to the close

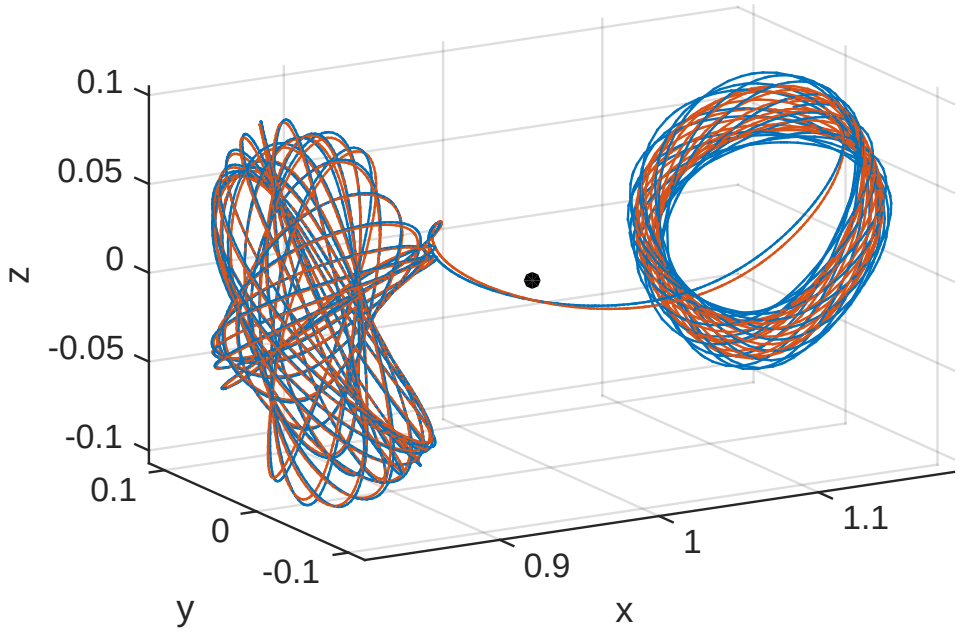

Figure 5.3: Earth–Moon L_2 quasihalo to L_1 Lissajous connection in ephemeris model

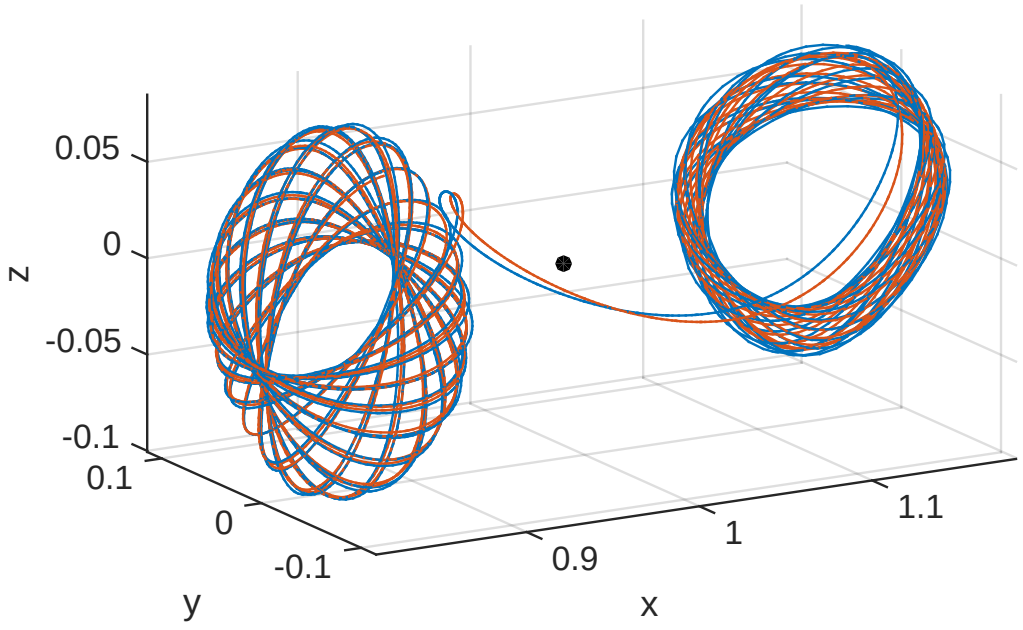

Figure 5.4: Earth–Moon L_2 quasihalo to L_1 quasihalo connection in ephemeris model

passage by the Earth. If the reference trajectory is generated using the Earth's location (rather than the Earth–Moon barycenter) during the close approach, it is possible that the initial guess would be more accurate. This work is ongoing.

CHAPTER 6

CONCLUSION AND FUTURE WORK

Motion in the solar system can be complicated and far from the conic solutions to the two-body problem. Nevertheless, in many regions there is an underlying dynamical structure that a spacecraft follows. This structure can be understood from the invariant manifolds existing in simplified models such as the restricted three-body problem. In this work, we have developed a set of computational tools for studying these manifolds. Various avenues for further exploration are available.

6.1 CONTRIBUTIONS

A common thread in this work is the use of collocation methods. Collocation methods have proven to be powerful tools for solving boundary value problems, particularly for computing periodic orbits. One of the primary contributions of the current work is extending the applicability of these methods to the computation of two-dimensional invariant tori, particularly in Hamiltonian systems which appear often in astrodynamics and various other fields. A focus in the development was to formulate a general-purpose tool that is not limited to a specific system and that does not require an a priori knowledge of the torus shape.

It should be noted that Hamiltonian systems possess special structure that is not present in generic dynamical systems. Entire families of tori exist even without any free external parameters. We are able to embed the system in a family of generic dynamical systems by introducing "unfolding" parameters. These parameters provide us with a well-posed boundary value problem, while maintaining the solution structure of the original Hamiltonian system. In particular, we end up with systems that after discretization have an equal number of equations as unknowns. This is beneficial

when dealing with the large numbers of variables associated with a collocation method.

In many applications we are interested not only in the tori themselves but also in the behavior in their vicinity. We present a simple approach to extract the state transition matrix from the collocation Jacobian matrix, and then use this to compute the eigenvalues of the torus's Floquet matrix. For hyperbolic tori, we can determine the stable and unstable directions at each point on the torus, which can then be globalized to produce the stable and unstable manifolds that asymptotically approach and depart the torus.

The results presented in this document primarily serve to validate the methods. First, two-dimensional tori are presented in the circular restricted three-body problem including sample stable and unstable manifolds. These tori match the well-known Lissajous and quasi-halo orbits that have been generated earlier using semi-analytic and shooting-based techniques. A benefit over shooting-based techniques, however, is that we directly obtain a complete parameterization of the entire torus rather than one or more circles on the torus surface. To test the scheme on non-autonomous systems, we consider both the elliptic restricted three-body problem and the Hill restricted four-body problem.

After computing invariant tori by solving the appropriate boundary value problems, we subsequently use these tori as boundary conditions for computing connecting orbits. Connecting orbits allow a spacecraft to naturally visit different regions of space. We presented their computation in the CR3BP with two techniques. While specifying only a single initial torus, we were able to generate an entire family of connections from the Earth–Moon L_2 to L_1 libration points. This family from a quasi-halo orbit at L_2 connects to both Lissajous and quasi-halo orbits at L_1. Despite only one boundary torus being explicitly specified, the collocation method was sufficiently stable to compute many windings around the destination torus. From the windings it was possible to extract the destination torus.

We also constructed a boundary value problem where both end torus conditions were explicitly specified. This allowed us to generate a complete two-parameter family of spatial heteroclinic connections between the Sun–Earth L_1 and L_2 libration points at a fixed energy. While there are only two planar connections in this family, there are many more spatial connections associated with

it.

The collocation method is also directly applicable to optimization problems. This is illustrated by the simple, yet practical, problem of finding libration point trajectories in a model depending on the ephemeris positions of the solar system bodies. We look for the nearest natural solution to the reference trajectory, while enforcing the ephemeris model dynamics. This appears to often provide a robust means of transitioning trajectories from a simplified model to a model closer to reality.

A common theme in this document is the importance of families of solutions rather than individual ones. One of the primary benefits of considering quasi-periodic tori is their prevalence. In the circular restricted three-body problem, there are entire families of these tori at a fixed energy level whereas there are only isolated periodic orbits. Likewise while heteroclinic connections between periodic orbits are comparatively quite rare, two-parameter families of connections between non-planar tori exist at a fixed energy level. Considering the quasi-periodic trajectories thus greatly expands the available design space for a spacecraft.

6.2 NEXT STEPS

In subsequent work, a more exhaustive exploration of the invariant tori in Sun–Earth and Earth–Moon systems is of interest. Given the general-purpose nature of the algorithms, it should also be possible to consider additional systems. Particularly interesting would be to study motion about small bodies. An irregular gravity field should not be a significant hurdle since no symmetry properties of tori are assumed. In addition, while this document focuses on two-dimensional tori, the basic techniques should generalize in a natural manner to three- and higher-dimensional tori. This is a topic of ongoing work.

The connection families could be used as a basis for shadowing chains of connections. This would allow a spacecraft to visit several (non-planar) tori at different libration points within a system. While connections focus on the most common systems, the Sun–Earth and Earth–Moon CR3BP, other systems can be investigated such as Sun–Mars and planet–moon systems. Furthermore, natural connections between systems can be studied. In fact, a motivation behind the study of the

Hill restricted four-body problem was the analysis of "system-to-system" connections between the Sun–Earth and Earth-Moon libration points in a coherent framework. Early computations in this direction seem promising.

The computations in this document do not include spacecraft maneuvers. In future work, maneuvers can be included, which would further expand the trajectory design space. Low-energy trajectories will still be driven by the natural dynamics. Thus, the natural behavior we have computed could be used as a skeleton for the low-energy transfer options.

BIBLIOGRAPHY

Andreu, M. A. [1999] The Quasi-Bicircular Problem, PhD thesis, Universitat de Barcelona, Spain.

Arona, L., & Masdemont, J.J. [2007] "Computation of heteroclinic orbits between normally hyperbolic invariant 3-spheres foliated by 2-dimensional invariant tori in Hill's problem," Discrete and Continuous Dynamical Systems, Supplement 2007, pp. 64–74.

Ascher, U. M., Mattheij, R. M. M., & Russell, R. D. [1995] Numerical Solution of Boundary Value Problems for Ordinary Differential Equations, 1st ed. reprint, SIAM, Philadelphia.

Baresi, N., Olikara, Z. P., & Scheeres, D. J. [2016] "Survey of numerical methods for computing quasi-periodic invariant tori in astrodynamics," AAS/AIAA Space Flight Mechanics Meeting, Napa, California.

Belló, M., Gómez, G., & Masdemont, J. J. [2010] "Invariant manifolds, Lagrangian trajectories and space mission design," Space Manifold Dynamics: Novel Spaceways for Science and Exploration, Eds. Perozzi, E., & Ferraz-Mello, S., Springer, New York, pp. 1–96.

Boor, C. de, & Swartz, B. [1973] "Collocation at Gaussian points," SIAM Journal on Numerical Analysis, Vol. 10, No. 4, pp. 582–606.

Broer, H. W., Huitema, G. B., & Sevryuk, M. B. [1996] Quasi-Periodic Motions in Families of Dynamical Systems: Order Amidst Chaos, 1st ed., Lecture Notes in Mathematics Vol. 1645, Springer, New York.

Calleja, R. C., Doedel, E. J., Humphries, A. R., Lemus-Rodríguez, A., & Oldeman, E. B. [2012] "Boundary-Value Problem Formulations for Computing Invariant Manifolds and Connecting Orbits in the Circular Restricted Three Body Problem," Celestial Mechanics and Dynamical Astronomy, Vol. 114, No. 1–2, pp. 77–106.

Campagnola, S., Lo, M. W., & Newton, P. [2008] "Subregions of Motion and Elliptic Halo Orbits in the Elliptic Restricted Three-Body Problem," AIAA/AAS Space Flight Mechanics Meeting, Galveston, Texas.

Canalias, E., Delshams, A., Masdemont, J. J., & Roldán, P. [2006] "The scattering map in the planar restricted three body problem" Celestial Mechanics and Dynamical Astronomy, Vol. 95, No. 1–4, pp. 155–171.

Castellà, E., & Jorba, À. [2000] "On the Vertical Families of Two-dimensional Tori near the Triangular Points of the Bicircular Problem," Celestial Mechanics and Dynamical Astronomy, Vol. 76, No. 1, pp. 35–54.

Conley, C. [1968] "Low energy transit orbits in the restricted three body problem," SIAM Journal on Applied Mathematics, Vol. 16, No. 4, pp. 732–746.

Davis, T.A., Rajamanickam, S., & Sid-Lakhdar, W.M. [2016] "A survey of direct methods for sparse linear systems," (To appear) Acta Numerica.

Delshams, A., Masdemont, J. J., & Roldán, P. [2008] "Computing the scattering map in the spatial Hill's problem," Discrete and Continuous Dynamical Systems Series B, Vol. 10, No. 2–3, pp. 455–483.

Doedel, E. J., Keller, H. B., & Kernevez, J. P. [1991] "Numerical analysis and control of bifurcation problems (II): Bifurcation in infinite dimensions," International Journal of Bifurcation and Chaos, Vol. 1, No. 4, pp. 745–772.

Doedel, E. J., Paffenroth, R. C., Keller, H. B., Dichmann, D. J., Galán-Vioque, J., & Vanderbauwhede, A. [2003] "Computation of periodic solutions of conservative systems with application to the 3-body problem," International Journal of Bifurcation and Chaos, Vol. 13, No. 6, pp. 1353–1381.

Doedel, E. J., Romanov, V. A., Paffenroth, R. C., Keller, H. B., Dichmann, D. J., Galán-Vioque, J., & Vanderbauwhede, A. [2007] "Elemental periodic orbits associated with the libration points in the circular restricted 3-body problem," International Journal of Bifurcation and Chaos, Vol. 17, No. 8, pp. 2625–2677.

Farquhar, R. W. [1967] "Lunar communications with libration-point satellites," Journal of Spacecraft and Rockets, Vol. 4, No. 10, pp. 1383–1384.

Farquhar, R. W., & Kamel, A. A. [1973] "Quasi-Periodic Orbits About the Translunar Libration Point," Celestial Mechanics and Dynamical Astronomy, Vol. 7, No. 4, pp. 458–473.

Gardner, J. P., Mather, J. C., Clampin, M., Doyon, R., Greenhouse, M. A., Hammel, H. B., ..., & Lunine, J. I. [2006] "The James Webb Space Telescope," Space Science Reviews, Vol. 123, No. 4, pp. 485–606.

Goldstein, H., Poole, C. P., & Safko, J. L. [2002] Classical Mechanics, 3rd ed., Pearson, New York.

Gómez, G., Jorba, À., Masdemont, J. J., & Simó, C. [1993] "Study of the transfer from the Earth to a halo orbit around the equilibrium point L_1," Celestial Mechanics and Dynamical Astronomy, Vol. 56, No. 4, pp. 541–562.

Gómez, G., Masdemont, J. J., & Simó, C. [1998] "Quasihalo orbits associated with libration points," Journal of the Astronautical Sciences, Vol. 46, No. 2, pp. 135–176.

Gómez, G., Jorba, À., Masdemont, J. J., & Simó, C. [2001a] Dynamics and Mission Design Near Libration Points III: Advanced Methods for Collinear Points, 1st ed., World Scientific, Singapore.

Gómez, G., & Mondelo, J. M. [2001b] "The dynamics around the collinear equilibrium points of the RTBP," Physica D, Vol. 157, No. 4, pp. 283–321.

Gómez, G., Koon, W. S., Lo, M. W., Marsden, J. E., Masdemont, J., & Ross, S. D. [2004] "Connecting orbits and invariant manifolds in the spatial restricted three-body problem," Nonlinearity, Vol. 17, No. 5, pp. 1571–1606.

Guckenheimer, J., & Holmes, P. [2002] Nonlinear Oscillations, Dynamical Systems, and Bifurcations of Vector Fields, 7th ed., Applied Mathematical Sciences Vol. 42, Springer, New York.

Gúzman, J. [2001] Spacecraft Trajectory Design in the Context of a Coherent Restricted Four-Body Problem, PhD thesis, Purdue University, West Lafayette.

Haro, À., & Llave, R. de la [2006] "A parameterization method for the computation of invariant tori and their whiskers in quasi-periodic maps: numerical algorithms," Discrete and Continuous Dynamical Systems Series B, Vol. 6, No. 6, pp. 1261–1300.

Howell, K. C., & Pernicka, H. J. [1988] "Numerical determination of Lissajous trajectories in the restricted three-body problem," Celestial Mechanics and Dynamical Astronomy, Vol. 41, No. 1–4, pp. 107–124.

Howell, K. C., Barden, B. T., & Lo, M. W. [1997] "Application of dynamical systems theory to trajectory design for a libration point mission," Journal of the Astronautical Sciences, Vol. 45, No. 2, pp. 161–178.

Jorba, À., & Villanueva, J. [1997a] "On the normal behaviour of partially elliptic lower-dimensional tori of Hamiltonian systems" Nonlinearity, Vol. 10, No. 4, pp. 783–822.

Jorba, À., & Villanueva, J. [1997b] "On the persistence of lower dimensional invariant tori under quasi-periodic perturbations," Journal of Nonlinear Science, Vol. 7, No. 5, pp. 427–473.

Jorba, À., & Masdemont, J. J. [1999] "Dynamics in the center manifold of the restricted three-body problem," Physica D, Vol. 132, No. 1–2, pp. 189–213.

Jorba, À. [2001] "Numerical computation of the normal behaviour of invariant curves of n-dimensional maps," Nonlinearity, Vol. 14, No. 5, pp. 943–976.

Jorba, À., & Olmedo, E. [2009] "On the computation of reducible invariant tori in a parallel computer," SIAM Journal of Applied Dynamical Systems, Vol. 8, No. 4, pp. 1382–1404.

Kolemen, E., Kasdin, N. J., & Gurfil, P. [2012] "Multiple Poincaré sections method for finding the quasiperiodic orbits of the restricted three-body problem," Celestial Mechanics and Dynamical Astronomy, Vol. 112, No. 1, pp. 47–74.

Koon, W. S., Lo, M. W., Marsden, J. E., & Ross, S. D. [2000] "Heteroclinic connections between periodic orbits and resonance transitions in celestial mechanics," Chaos, Vol. 10, No. 2, pp. 427–469.

Lanczos, C. [1986] The Variational Principles of Mechanics, 4th ed., Dover, New York.

Llave, R. de la [2001] "A Tutorial on KAM Theory," Smooth Ergodic Theory and Its Applications, Proceedings of Symposia in Pure Mathematics Vol. 69, American Mathematical Society, Providence, pp. 175–292.

Lo, M., Williams, B., Bollman, W., Hahn, D., Bell, J., Hirst, E., Corwin, R., Hong, P., Howell, K., Barden, B., & Wilson, R. [1998] "Genesis mission design," AIAA/AAS Astrodynamics Specialist Conference, Boston, Massachusetts.

Meyer, K. R., & Hall, G. R. [1992] Introduction to Hamiltonian Dynamical Systems and the N-Body Problem, 1st ed., Applied Mathematical Sciences Vol. 90, Springer, New York.

Mohn, L., & Kevorkian, J. [1967] "Some limiting cases of the restricted four-body problem," The Astronomical Journal, Vol. 72, No. 8, pp. 959–963.

Mondelo, J. M., Barrabés, E., Gómez, G., & Ollé, M. [2009] "Automatic generation of Lissajous-type libration point trajectories and its manifolds for large energies," International Symposium on Space Flight Dynamics, Toulouse, France.

Muñoz-Almaraz, F. J., Freire, E., Galán, J., Doedel, E., & Vanderbauwhede, A. [2003] "Continuation of periodic orbits in conservative and Hamiltonian systems," Physica D, Vol. 181, No. 1, pp. 1–38.

Olikara, Z. P. [2010] Computation of Quasi-Periodic Tori in the Circular Restricted Three-Body Problem, MS thesis, Purdue University, West Lafayette.

Olikara, Z. P., & Scheeres, D. J. [2012] "Numerical method for computing quasi-periodic orbits and their stability in the restricted three-body problem," IAA Conference on Dynamics and Control of Space Systems, Porto, Portugal.

Olikara, Z. P., Gómez, G., & Masdemont, J. J. [2015] "Dynamic mechanisms for spacecraft disposal from Sun–Earth libration points," Journal of Guidance, Control, and Dynamics, Vol. 38, No. 10, pp. 1976–1989.

Olikara, Z. P., Gómez, G., & Masdemont, J. J. [2016] "A note on dynamics about the coherent Sun–Earth–Moon collinear libration points," Proceedings of the AstroNet-II International Final Conference, Springer, New York.

Parker, J. S., Davis, K. E., & Born, G. H. [2010] "Chaining periodic three-body orbits in the Earth–Moon system," Acta Astronautica, Vol. 67, No. 5–6, pp. 623–638.

Parker, J. S., & Anderson, R. L. [2013] Low-Energy Lunar Trajectory Design, Deep Space Communications and Navigation Series, JPL, Pasadena.

Perko, L. [1991] Differential Equations and Dynamical Systems, 1st ed., Texts in Applied Mathematics Vol. 7, Springer, New York.

Richardson, D. L., & Cary, N. D. [1975] "A uniformly valid solution for motion about the interior libration point of the perturbed elliptic-restricted problem," AAS/AIAA Astrodynamics Specialist Conference, Nassau, Bahamas.

Russell, R. D., & Christiansen, J. [1978] "Adaptive mesh selection strategies for solving boundary value problems," SIAM Journal on Numerical Analysis, Vol. 15, No. 1, pp. 59–80.

Scheeres, D. J. [1998] "The restricted Hill four-body problem with applications to the Earth–Moon–Sun system," Celestial Mechanics and Dynamical Astronomy, Vol. 70, No. 2, pp. 75–98.

Schilder, F., Osinga, H. M., & Vogt, W. [2005] "Continuation of quasi-periodic invariant tori," SIAM Journal on Applied Dynamical Systems, Vol. 4, No. 3, pp. 459–488.

Sepulchre, J. A., & MacKay, R. S. [1997] "Localized oscillations in conservative or dissipative networks of weakly coupled autonomous oscillators," Nonlinearity, Vol. 10, No. 3, pp. 679–713.

Simó, C., Gómez, G., Jorba, À., & Masdemont, J. J. [1995] "The bicircular model near the triangular libration points of the RTBP," From Newton to Chaos, Eds. Roy, A. E., & Steves, B. A., Springer, New York, pp. 343–370.

Simó, C. [1998] "Effective computations in celestial mechanics and astrodynamics," Modern Methods of Analytical Mechanics and Their Applications, Eds. Rumyantsev, V. V., & Karapetyan, A. V., Springer, New York, pp. 55–102.

Szebehely, V. [1967] Theory of Orbits: The Restricted Problem of Three Bodies, 1st ed., Academic Press, New York.